

**DYNAMICS OF PROPAGATING MODES AND
CHARACTERISATION OF ORDERING IN COUPLED
NON-EQUILIBRIUM SYSTEMS**

A THESIS SUBMITTED FOR THE DEGREE OF
DOCTOR OF PHILOSOPHY (SCIENCE)
IN PHYSICS (THEORETICAL)

by
SHAURI CHAKRABARTY

Department of Physics
University of Calcutta

2019

*“Here on the level sand,
Between the sea and land,
What shall I build or write
Against the fall of night?*

*Tell me of runes to grave
That hold the bursting wave,
Or bastions to design
For longer date than mine.”*

— G. H. Hardy
A Mathematician’s Apology

ACKNOWLEDGEMENTS

There is perhaps no task more difficult than that of acknowledging the contributions of the people whose constant support has made this journey possible. While writing, I struggle to find my way through words that convey so very little. At the outset, I would like to thank my supervisor, Dr. Sakuntala Chatterjee, who has been guiding me for the past years in my masters projects and later, in my PhD work. Under her guidance, I have had the opportunity of being exposed to a rich class of problems that has greatly inspired my enthusiasm in the field of statistical physics. Over the past five years, in context of my thesis problems, I have thoroughly enjoyed enlightening discussions with Prof. Mustansir Barma on several occasions. The lectures by Prof. J. K. Bhattacharjee, Prof. S. S. Manna, and Prof. Punyabrata Pradhan on quantum mechanics, computational physics, and statistical physics during my Masters days were exceptionally motivating and I am fortunate enough to have had them as my teachers. It is hard to find words that justly describe the contribution of my teacher Dr. Arup Roy who has mentored me since my college days. The interactions with him have had a lasting impact that has ushered an altogether new perspective towards life. I was blessed to have Mr. Naliniranjan Sarkar, the former headmaster of my school, as my teacher — it has truly been an inspiration to have known him as a human being. My sincere thanks to Mr. Sunish Kumar Deb for all his encouragement and support during the past years at the S. N. Bose institute and all the staffs of this centre for their cooperation. All these years have endowed me with friendships that is to be cherished for the rest of my life. A hearty thanks to Rajkumar Sadhu and Subrata Dev for being the wonderful group-mates that they have been — PhD life would have been much more difficult without them. Chandreyee, Debolina have been great hostel-mates for almost two years, and lovely friends thereafter. A very special thanks to my senior Sayani Chatterjee, whom I have known for almost 11 years now, for being such a kind friend to me. I will fondly remember the musical sessions with Subhasish Chakrabarty. No word of thanks would be enough for the unexpected gesture of support that I continue to receive from Dr. Arghya Dutta. I would love to acknowledge the extremely valuable discussions with Dr. Urna Basu in different contexts. The pleasant times spent with Ritam, Anirban, Rituparna, Dhiraj, and Santanu during the last years of my stay at the S. N. Bose centre will be ever memorable. My love to Monalisa, Samiran, and Poonam for constantly being with me; they have made my hard times endurable. The fond times with Aritra and Anasuya are something I will always look forward to; these past years have gifted me with their companionship, that is to remain a treasure for all times to come. I could not

thank Anisha Chandra, Ansuman Dey, Utsab Chatterje, Pratap Mukherjee, and Subhadipa Das enough for their unconditional love and support — they have re-defined the meaning of friendship for me. Vidhayak Goswami has remained a true friend ever since my school days. My parents have always encouraged me to pursue my passions in spite of all the hardships in their lives; without their support it would not have been possible for me to choose this path. It is impossible to gather words to thank my elder brother for being a guarding shield forever; our bonding has grown all the more strong through the turbulent times that we have faced together. My sister-in-law, Dolly Chattopadhyay, has always been by my side as a resort to seek. She has been more of an elder sister to me for the past 20 years. A quirky thanks to Pratik for all his help and patience while I struggle with Mathematica, and my life too. Many a times, when I pause to take a look back and think awhile what has kept me going, countless faces keep lighting up in unison. A few pages of acknowledgement would not be enough to express gratitude to all those who have, through their loving gestures, helped me take yet another step by being there, even if for a short while. I would consider myself fortunate if it is ever possible, through my actions, to repay even a miniscule amount of the huge debts that I have incurred through all these years.

PUBLICATIONS TO BE INCLUDED IN THE PHD THESIS

- *Large compact clusters and fast dynamics in coupled nonequilibrium systems*,
Shauri Chakraborty, Sukla Pal, Sakuntala Chatterjee, and Mustansir Barma, Phys. Rev. E. **93**, 050102(R) (2016).
- *Ordered phases in coupled nonequilibrium systems: Static properties*,
Shauri Chakraborty, Sakuntala Chatterjee, and Mustansir Barma, Phys. Rev. E **96**, 022127 (2017).
- *Ordered phases in coupled nonequilibrium systems: Dynamic properties*,
Shauri Chakraborty, Sakuntala Chatterjee, and Mustansir Barma, Phys. Rev. E **96**, 022128 (2017).
- *Dynamics of coupled modes for sliding particles on a fluctuating landscape*,
Shauri Chakraborty, Sakuntala Chatterjee, and Mustansir Barma, (Manuscript in preparation) (2019).

CONTENTS

1	INTRODUCTION	1
1.1	Phase separation in coupled systems	3
1.2	Framework for non-linear fluctuating hydrodynamics and mode-coupling theory	6
1.3	Motivation and focus of thesis	10
1.4	Synopsis of main results and plan of thesis	10
1.4.1	Chapter 2: Summary	11
1.4.2	Chapter 3: Summary	11
1.4.3	Chapter 4: Summary	13
1.4.4	Chapter 5: Summary	13
1.4.5	Chapter 6: Summary	14
2	PHASE DIAGRAM FOR A COUPLED NON-EQUILIBRIUM SYSTEM OF PARTICLES ON A FLUCTUATING LANDSCAPE	15
2.1	Introduction	15
2.2	Model description	15
2.3	Phase diagram	17
2.3.1	Strong phase separation(SPS)	19
2.3.2	Infinitesimal current with phase separation(IPS)	20
2.3.3	Finite current with phase separation(FPS)	21
2.3.4	The disordered phase	21
2.4	Conclusion	22
3	STATIC PROPERTIES OF ORDERED PHASES IN THE LH MODEL	23
3.1	Introduction	23
3.2	Static characterisation of the ordered phases	23
3.3	SPS (Strong phase separation) phase [$b' > 0$]	25
3.3.1	Detailed balance in the SPS phase	25
3.3.2	Coarsening in the SPS phase	26
3.3.3	Rescaled temperature and phase transitions in SPS phase	27
3.4	IPS (Infinitesimal current with phase separation) phase [$b' = 0$]	31
3.4.1	Breakdown of detailed balance in the IPS phase	31
3.4.2	A single H particle in the IPS phase: height profile of the landscape	32

3.4.3	Clustering of H particles in the IPS phase in the adiabatic limit	32
3.4.4	Coarsening in the IPS phase	34
3.4.5	Rescaled temperature and phase transitions in the IPS phase	35
3.4.6	Static correlations in the IPS phase	37
3.5	FPS (Finite current with phase separation) phase [$-b < b' < 0$]	38
3.5.1	Coarsening in the FPS phase	39
3.5.2	Static correlations in H -region of the landscape in FPS phase	39
3.5.3	FDPO (Fluctuation-dominated phase ordering) phase [$b = -b'$]	41
3.6	Conclusion	42
4	DYNAMIC PROPERTIES OF ORDERED PHASES IN THE LH MODEL	43
4.1	Introduction	43
4.2	Slow dynamics in the SPS (Strong phase separation) phase	43
4.3	Dynamics in the IPS (Infinitesimal current with phase separation) phase	44
4.3.1	Mechanism for small time behaviour of valley dynamics in IPS phase	45
4.3.2	Mechanism for large time behaviour of valley dynamics in IPS phase	47
4.3.3	Valley dynamics as an Ornstein-Uhlenbeck process in the IPS phase	49
4.3.4	Scaling ansatz for dynamical correlation functions beneath the H -cluster in IPS phase	50
4.3.5	Landscape dynamics beneath the L -cluster in the IPS phase	51
4.4	Dynamics in the FPS (Finite current with phase separation) phase	52
4.4.1	Height fluctuations induced by valley dynamics in FPS phase	54
4.4.2	Landscape dynamics beneath the L -cluster in FPS phase	55
4.5	Conclusion	57
5	LH MODEL IN TWO DIMENSIONS — SQUARE AND TRIANGULAR LATTICE GEOMETRIES	59
5.1	Introduction	59
5.2	Results on a two dimensional square lattice	59
5.2.1	Fast coarsening to IPS and FPS phases on a square lattice	60
5.2.2	Finite size effects in topologies on a square lattice	60
5.3	Steady state dynamics on a square lattice	62
5.4	Results on a two dimensional triangular lattice	64
5.4.1	Finite size effects in topologies on a triangular lattice	64
5.5	Conclusion	66
6	NUMERICAL VERIFICATION OF MODE-COUPLING THEORY AND NON-LINEAR FLUCTUATING HYDRODYNAMICS FOR PROPAGATING MODES IN LH MODEL	67

6.1	Introduction	67
6.2	Short-ranged correlations and mean-field calculation in the disordered phase	68
6.2.1	Calculating currents from nearest neighbor approximations — master equation for two-point correlations	70
6.2.2	Calculating currents from next nearest-neighbour approximations — master equations for three-point correlations	72
6.3	Simulation results for dynamical structure function	77
6.3.1	Significant finite size effects for $b = b' = -0.5$	78
6.3.2	KPZ and 5/3 Lévy mode	80
6.3.3	Modified KPZ and diffusive mode	81
6.3.4	Golden mean modes	84
6.3.5	3/2-Lévy and diffusive mode	86
6.4	Conclusion	87

LIST OF FIGURES

Figure 1.1	Typical configuration of a system in SPS phase.	4
Figure 1.2	Typical configuration of a system in the FDPO phase.	5
Figure 2.1	Phase diagram for the LH-model in the scaled $b - b'$ plane.	17
Figure 2.2	Typical configurations of the LH-model in each phase.	19
Figure 3.1	Alternative representation of the phase diagram for LH-model.	24
Figure 3.2	Schematic representations of allowed transitions in the LH-model.	26
Figure 3.3	Scaled density-density correlation plot during coarsening in the SPS phase.	27
Figure 3.4	Temperature variation of order parameters s_ρ, s_m in the SPS phase.	30
Figure 3.5	Breakdown of the Kolmogorov loop condition in the IPS phase.	31
Figure 3.6	Density profile of the landscape with a single H -particle in the IPS phase.	33
Figure 3.7	Schematic representation of the coarsening mechanism in the IPS phase.	35
Figure 3.8	Scaled density-density correlation plot during coarsening in the IPS phase.	35
Figure 3.9	Temperature variation of order parameters s_ρ, s_m in the IPS phase.	37
Figure 3.10	Static correlation functions in IPS phase.	38
Figure 3.11	Scaled density-density correlation plot during coarsening in the FPS phase.	39
Figure 3.12	(a) Comparison of numerically measured asymptotic values of $S^+(r, N)$ with mean-field results in the FPS phase, (b) Scaling of domain boundary width in the FPS phase.	40
Figure 3.13	Algebraic $1/\sqrt{r}$ variation of the density profile of the landscape from the $H - L$ domain boundary in the FPS phase.	41
Figure 4.1	Schematic depiction of the average height profiles of the landscape and particle configurations in the ordered phases of the LH model.	44
Figure 4.2	Mean-squared displacement of the deepest point of the valley in the IPS phase.	45
Figure 4.3	Schematic representation of height fluctuations in landscape in the IPS phase.	46
Figure 4.4	Mechanism for short-time ($t \ll N^2$) valley displacement.	47
Figure 4.5	Mechanism for large-time ($t \gg N^2$) valley displacement.	48

Figure 4.6	Probability to find an L particle at the deepest point of the surface in the IPS phase. 49
Figure 4.7	Valley dynamics as an Ornstein-Uhlenbeck process in the IPS phase. 50
Figure 4.8	Scaling collapse of dynamical correlation functions in IPS phase. 51
Figure 4.9	Numerical evidence of correspondence between the landscape beneath the L -cluster in the IPS phase and an open-chain SEP. 52
Figure 4.10	Scaling collapse of dynamical correlation functions in FPS phase. 53
Figure 4.11	Tagged mean squared displacement of an upslope bond inside the H -cluster in FPS phase. 54
Figure 4.12	Current fluctuation measured at the deepest point of the landscape in IPS and FPS phases. 55
Figure 4.13	Schematic depiction of height fluctuations in the landscape in the FPS phase. 55
Figure 4.14	Numerical proof that the valley displacement in the FPS phase can not be represented as an Ornstein-Uhlenbeck process. 56
Figure 4.15	Sliding tag correlation function for an upslope bond beneath the L -cluster in the FPS phase. 57
Figure 5.1	Scaling of particle density correlation in the coarsening phase on a two dimensional square lattice in IPS and FPS phases. 60
Figure 5.2	Representative plots for diamond and wedge type configurations in the IPS phase in two dimensions. 61
Figure 5.3	Landscape dynamics in two dimensions. 63
Figure 5.4	Representative plots for hexagonal, wedge, and triangular type configurations in the IPS phase in two dimensions on a triangular lattice. 65
Figure 6.1	Colour plot for nearest neighbor correlations in the disordered phase for $m = 1/2$. 69
Figure 6.2	Demonstration of strong finite size effects in numerical verification of two KPZ modes in the LH model. 79
Figure 6.3	Contour map of all the four diagonal elements of the mode-coupling matrices in ρ, m plane for $b = -0.3, b' = -0.3$. 80
Figure 6.4	Strong finite size effects in the numerical verification of the 5/3-rd Lévy universality class in LH model. 82
Figure 6.5	Numerical verification of the modified KPZ universality class in LH model. 83
Figure 6.6	Contour map of all the four diagonal elements of the mode-coupling matrices in ρ, m plane for $b = -0.3, b' = -0.5$. 84

- Figure 6.7 Contour map of all the four diagonal elements of the mode-coupling matrices in ρ, m plane for $b = 0.1, b' = -0.3$. 85
- Figure 6.8 Strong finite size effects in the numerical observation of the 3/2-Lévy and gold-Lévy universality classes in LH model. 86

LIST OF TABLES

Table 2.1	Different phases observed in the LH model and their qualitative descriptions. 19
Table 6.1	Comparison between particle and tilt currents measured in simulations and calculated from 2-point, 3-point master equations, and mean field theory. 77
Table 6.2	Comparisons between the numerically measured speeds estimated from the moving peaks of the dynamical structure factors, speeds calculated using the currents obtained by solving the master equations, and the mean field values. 77

INTRODUCTION

In nature, we often come across examples of a wide range of natural phenomena ranging from microscopic to macroscopic length-scales that fall under the category of non-equilibrium phenomena. Biological processes such as cell growth [1], movement of micro-tubular motor proteins [2], growth of bacterial colonies [3], besides physical phenomena like moving traffic [4], turbulent fluid flow [5] fall under the broad category of non-equilibrium processes. Such systems constantly gain (lose) energy from (to) an external driving medium and are inherently out of equilibrium. Absence of equilibrium generically implies presence of a system-wide flux that might or might not be constant in space and time. For example, a chemical potential or thermal gradient across any two points in a system can give rise to particle or heat currents respectively. If the gradient varies in space and time, then the current will in general be a function of space and time. Many of these systems are known to attain a steady state in the long-time limit (*i.e.* a state with a time-invariant measure) — subject to a constant drive by an external field, these states are termed as "non-equilibrium steady states" (NESS) that carry a net current that remains stationary in space and time. Description of such systems is beyond the ambits of the Gibbs-Boltzmann framework, and much of their properties might be strikingly different from that of their equilibrium counterparts. A sub-class of non-equilibrium systems where each component of the system exhibits a certain degree of randomness in addition to being driven by an external field, are regarded as "driven diffusive systems" [6]. Till date, there exists no framework for the description of such non-equilibrium steady states that might be comparable in its generality to the Gibbs-Boltzmann framework for equilibrium systems. To understand the wealth of surprisingly different phenomena often exhibited by non-equilibrium systems that are impossible to observe for systems in equilibrium, one must take recourse to simple model systems that might provide insights into non-equilibrium behaviours.

In description of driven diffusive systems it is often useful to describe the system as an assembly of more than one interacting components. It often turns out that apart from the influence of an external driving field, the nature of coupling between the components might crucially affect the behaviour of the whole system. Examples of such coupled driven systems

can be found aplenty in several physical and biological contexts — the advection of a passive scalar by a fluid flow [7], motion of directed polymers in a random medium [8] are few of the many examples of coupled driven systems. The coupling might, in some cases be of a uni-directional nature in the sense that the evolution of one of the components strongly affects the other while the other being passively advected in the flow field of the former — smoke particles dispersed in air can be cited as one of the examples of one-way coupled systems [9]. In other situations, the coupling is bi-directional where both the species strongly affect the time-evolution of one another. Let us consider an example in a biological setting. Proteins and lipids on the membrane of a living cell are found to cluster, advected by fluctuations of the actin cytoskeleton [10–12]. A recent model considers these membrane components to be advected passively, in which case the clusters are not stable, and reorganize constantly [13]. However, there is experimental evidence that the membrane components also act back on the actin [14, 15]. The resulting two-way coupling has the potential to affect the qualitative nature of clustering. There are ample instances of large-scale organisation of varying features taking place among one or all of the coupled species in the system depending on the nature of coupling. Hence, the combination of an external driving field and the coupling between different components in a system can indeed give rise to macroscopic clustering properties. However, the coupling may also drive the system towards a homogeneous, disordered state with no long-ranged correlations in the system [16–18].

In this thesis we explore a both-way coupled non-equilibrium lattice gas model which shows a novel phase diagram of several ordered phases along with a disordered regime on tuning the coupling parameter between the different components of the system. Depending on the form and strength of the two-way coupling, clusters may be stable, compact objects or dynamical entities which keep forming and disintegrating on a rapid time scale, or there might be no clustering at all and the coupling can give rise to a disordered, homogeneous state. A recently developed formalism of non-linear fluctuating hydrodynamics has proven to be useful in studying the dynamics of such coupled, disordered phases [18, 19]. We have carried out an extensive characterisation of the static and dynamic aspects of all the ordered and disordered phases obtained on varying the coupling parameters in our model system using numerical simulations and analytical techniques. Hereafter, this chapter will consist of a brief review of the earlier works that have been done in characterising phase separation in coupled systems along with the discussion of an analytical framework of non-linear fluctuating hydrodynamics that has been developed over the past few years to study disordered phases in coupled systems. The chapter ends with a synopsis of our main results which shall be elaborated in the chapters to follow.

Although equilibrium systems exhibit no phase transitions in one dimension, there are quite a lot of instances where driven, noisy systems show phase transition even in one dimension. For example, an asymmetric exclusion process (ASEP) with open boundaries shows phase transition by tuning the boundary injection and ejection rates [20]. Even in absence of any boundary effects, driven diffusive models show phase separation induced by defects that give rise to density inhomogeneities in the system [21]. In this section we intend to focus on earlier studies of yet another kind of phase separation exhibited by driven systems with two or more coupled species on tuning the coupling parameters in the system.

Let us consider the example of particles suspended in a solvent. If the density of the particles is larger than that of the solvent, then the particles will eventually settle down at the bottom of the fluid and form a sediment. The process of sedimentation strongly depends on the viscosity of the fluid and stochastic thermal fluctuations. Also, as the particle density is increased, the many-body hydrodynamic interactions can significantly affect the sedimentation as well. An experiment conducted with steel balls moving through Turpentine oil [22, 23] showed that any initial layer of particles distributed uniformly will form clusters as they drift through a viscous fluid. In the context of modelling the sedimentation of a colloidal crystal, continuum and lattice gas versions of a model was proposed by Lahiri et. al. [24, 25] that describes a set of particles performing a biased diffusive motion under gravity on a fluctuating landscape. The discrete version of the model can be thought of as two coupled sub-lattices consisting of density field of the particles and the height gradient field of the landscape. The dynamics of the coupled particle-landscape system is such that the particles tend to move towards the local minimum of the landscape and in doing so, affect the shape of the landscape further.

It was shown that for a broad parameter regime, the system reaches a completely phase separated state where the landscape shapes itself into a deep valley that holds all the particles together in a single cluster as shown in Fig. 1.1. It was further shown that for particular choice of densities and rates, such steady states satisfied the Gibbs-Boltzmann measure in terms of a Hamiltonian that involved long-ranged interactions in spite of the dynamics being local. It was also argued that even for other choice of system parameters for which the exact steady state measure could not be found, the system would nevertheless exhibit phase separation in the long time limit. The class of phase separation so obtained was named as "Strong Phase Separation" (SPS) because of certain thermodynamic properties which shall be elaborated in the subsequent chapters. A similar class of steady states were also reported in another lattice gas model also known as the ABC model comprising of three different types of hardcore particles (A,B and C) perform biased hopping on a periodic chain with rates dependent on

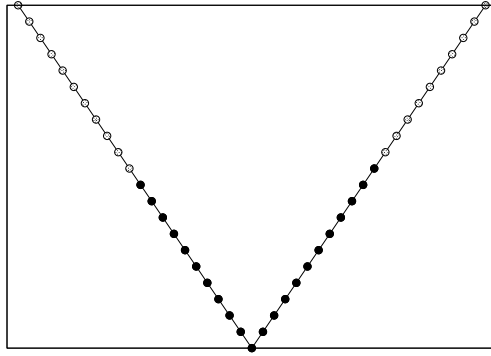


Figure 1.1: Typical configuration of a system in SPS phase

the nearest neighbour [26]. At each time step a bond is chosen randomly, and if the particles across the bond are dissimilar, they are exchanged according to the following rates:

$$\begin{aligned} W(AB \Leftrightarrow BA) &= W(BC \Leftrightarrow CB) = W(CA \Leftrightarrow AC) = q \\ W(BA \Leftrightarrow AB) &= W(CB \Leftrightarrow BC) = W(AC \Leftrightarrow CA) = 1 \end{aligned} \quad (1.1)$$

It was argued that complete phase separation between all the three species of particles will be obtained as long as densities of each of the species is non-zero. A generalised matrix product ansatz was employed to study the steady-state correlations of the system and for a particular limit where densities of all the species were equal, detailed balance was shown to hold. The study was also extended to a general case of m different species of particles with the steady state being characterised by a complete phase separation of each species.

Another qualitatively different kind of phase separation was reported in [27]. The model is similar in setting to that described in LR model, but in this case the evolution of the system is semi-autonomous — while the particles followed the local gradients of the landscape and preferentially settled at the local minima of the landscape, the landscape itself has an independent dynamics which remains unaffected by the particles. This is the case of passive scalar advection where the particles are advected by an autonomously evolving field underneath. When the particles obey hardcore constraint, the particles show a special kind of clustering where strong fluctuations are always present [27, 28]. Although the two-point density correlation function for the particles in the steady state is a scaling function of r/L [29], it shows a cusp singularity as opposed to the linear decay expected for usual phase-ordering systems. This is known as fluctuation dominated phase ordering (FDPO). We show a schematic diagram for a typical configuration of a system in the FDPO state in Fig. 1.2.

Recently, a coupled model of two types of particles embedded in a two-dimensional active medium was proposed [13] in the context of studying actomyosin-dependent phase segregation of protein molecules on cellular surfaces. Experimental studies have shown that

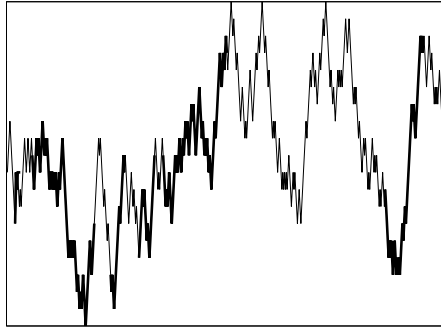


Figure 1.2: Typical configuration of a system in the FDPO phase. The dark patches represent particle clusters and the lighter patches indicate empty stretches of landscape.

actomyosins generate active stochastic stresses on the cell membrane, thus driving clustering of several membrane components [10–12]. The model in [13] considers two types of particles, passive and inert — while the passive particles (un)bind to the active filaments in the medium, the inert particles remain unaffected by the medium. On tuning the density of the filaments and also the active noise strength, a phase segregation of the passive molecules from the inert molecules was found. Further, it was shown that the phase segregated states showed giant fluctuations in order parameter and domain size, characteristic of FDPO [27, 30, 31]. However, in several biological systems it has been also observed that certain membrane proteins are capable of inducing actin-polymerisation at their binding sites and thereby cause local membrane protrusions [32, 33]. While the polymerisation and adhesion of the proteins at the binding sites drive them towards a clustered state, these clusters in turn cause linear instability that changes the membrane shape.

The problem of semi-autonomously evolving coupled systems has recently been extended to the realms of active matter in [34, 35]. In [34] a model of active membrane with particle-like inclusions has been introduced. The presence of particles stimulate the growth of the underlying membrane such that the rates of local membrane fluctuations are directly proportional to the local particle occupancies. On the other hand, the particles themselves show a tendency to cluster in the local minima of the membrane. It was shown that the coupling between the active elements and the interface dynamics drives a microphase segregation among the particles and generates ripple-like structures on the membrane. It was further shown that the scaling behaviour of an actively growing interface does not fall in the Kardar-Parisi-Zhang class of growing interfaces [36]. Another very recent work by the same authors [35] studies the limit of a single active particle on an Edward-Wilkinson type interface [37].

While coupling between the constituent components might drive macroscopic clustering in several systems as elaborated in the previous section, it might also lead to homogeneous, translationally invariant density profiles with no long-ranged correlations. We discuss a recently developed formalism of non-linear fluctuating hydrodynamics (NLFH) along with mode-coupling theory that can be incorporated to study the large-scale dynamical properties of systems with several coupled, conserved components that show no long-ranged order. A recent surge of activity in this field has led to new insights into the spatio-temporal scaling properties of several coupled fields $\{\rho_\alpha\}$, whose dynamical evolution involves couplings between the fields both at the linear and non-linear levels that result in propagating kinematic waves of fluctuations in the fields. The modes can be decoupled at the linear level by finding the correct linear combinations of ρ_α 's that yield the modes which propagate independently as kinematic waves. One can obtain the speeds λ_α of the propagating waves by diagonalising matrix of couplings which are in general different for all the modes. By a Galilean shift of λ_α , one may move to the rest frame of the α^{th} mode. The other modes, of course, are not stationary in this frame and may contribute to the dissipation of α^{th} mode as they are non-linearly coupled to it. The correlation function between the eigenmodes ϕ_α are given by $C_{\alpha\alpha} = \langle \phi_\alpha(0,0)\phi_\alpha(x,t) \rangle$ and are expected to satisfy the following scaling ansatz,

$$C_{\alpha\alpha}(x,t) \sim t^{-1/z_\alpha} f_\alpha\left(\frac{x - \lambda_\alpha t}{t^{1/z_\alpha}}\right) \quad (1.2)$$

where z_α is the dynamical exponent for the α^{th} mode and f_α is the scaling function. A pertinent question to ask is whether the value of z_α is same or different for all the modes. Recently it has been proposed that a non-linear extension of fluctuating hydrodynamics along with mode-coupling theory can yield comprehensive understanding of dynamical exponents that govern the dissipation of these modes along with the corresponding scaling functions. Non-linear fluctuating hydrodynamics (NLFH) has emerged as a universal tool to analyze general one-dimensional systems such Hamiltonian dynamics [38, 39], anharmonic chains [19, 40, 41], or driven diffusive systems [42, 43]. The theory is robust in the sense that it works for systems with generic dynamics — Hamiltonian, quantum, stochastic, with the restriction of being translationally invariant and the interactions being sufficiently short-ranged. The only essential ingredients for carrying out the formalism is the knowledge of the locally conserved currents J_α associated with each conserved field α . In this section we briefly outline the formalism of NLFH along with mode-coupling theory that has been developed over the past few years to study a system of n conserved fields.

The starting point for investigating the large-scale dynamical properties of a system with n conserved components is the continuity equation,

$$\frac{\partial \vec{\rho}(x, t)}{\partial t} + \frac{\partial \vec{J}(x, t)}{\partial x} = 0 \quad (1.3)$$

where $\vec{\rho}(x, t)$ and $\vec{J}(x, t)$ are n -dimensional vectors whose components $\rho_\alpha(x, t)$ and $J_\alpha(x, t)$ denote local density of the α -th conserved quantity and associated conserved current, respectively, with $\alpha = 1, 2, \dots, n$. Assumption of local equilibrium ensures that the current does not have any explicit space-time dependence, but depends on space and time only through its dependence on local densities. Using this Eq. 1.3 can be rewritten as,

$$\frac{\partial \vec{\rho}}{\partial t} + \mathbf{A} \frac{\partial \vec{\rho}}{\partial x} = 0 \quad (1.4)$$

where \mathbf{A} denotes the Jacobian with elements $A_{\alpha\beta} = \frac{\partial J_\alpha}{\partial \rho_\beta}$. Expanding the local density $\rho_\alpha(x, t)$ around its conserved global value ρ_α^0 , one can write $\rho_\alpha(x, t) = \rho_\alpha^0 + u_\alpha(x, t)$. Retention of linear terms in the small perturbation $u_\alpha(x, t)$ yields a set of coupled linear partial differential equations that can be solved by diagonalizing \mathbf{A}^0 whose elements are functions of $\{\rho_\alpha^0\}$. The normal modes $\vec{\phi} = \mathbf{R}^{-1}\vec{u}$ follow the equations $\partial_t \phi_\alpha(x, t) + \lambda_\alpha \partial_x \phi_\alpha(x, t) = 0$ where λ_α 's are eigenvalues of \mathbf{A}^0 . Therefore the normal modes satisfy travelling wave solutions $\phi_\alpha(x - \lambda_\alpha t)$ and λ_α can be interpreted as the speed of propagation of local perturbations in the system.

Beyond the linear theory, one expands the current \vec{J} around the stationary density values, and retains quadratic non-linearities in \vec{u} . This gives rise to coupling between the modes ϕ_α in the quadratic order. The time-evolution equation for $\phi_\alpha(x, t)$ then becomes,

$$\partial_t \phi_\alpha = -\partial_x [\lambda_\alpha \phi_\alpha + \vec{\phi}^T \mathbf{G}^\alpha \vec{\phi} - \partial_x (\mathbf{D}\vec{\phi})_\alpha + (\mathbf{B}\vec{\xi})_\alpha] \quad (1.5)$$

where a phenomenological diffusion term and a noise term has been added [44]. The Gaussian white noise has the strength $\langle \xi_\alpha(x, t) \xi_\alpha(x', t') \rangle = B_{\alpha\alpha} \delta(x - x') \delta(t - t')$ and the matrix \mathbf{B} can be assumed to be diagonal without any loss of generality. The mode-coupling matrices are defined as,

$$\mathbf{G}^\alpha = \frac{1}{2} \sum_\gamma R_{\alpha\gamma}^{-1} \mathbf{R}^T \mathbf{H}^\gamma \mathbf{R} \quad (1.6)$$

where the Hessian matrix $\mathbf{H}_{\alpha\beta}^\gamma = \partial^2 J_\gamma / \partial \rho_\alpha^0 \partial \rho_\beta^0$. With an exact knowledge of the current-density relationship, the elements of the mode-coupling matrices can be evaluated. The element $G_{\beta\beta}^\alpha$ denotes the coupling between the α -th and β -th mode. It is easy to see from Eq. 1.5 that the off-diagonal terms of \mathbf{G}^α do not influence the time-evolution of ϕ_α . The traveling wave solution predicted from linear theory does not remain valid anymore for Eq. 1.5 and

apart from moving through the system with speed λ_α , any local perturbation in ϕ_α would also dissipate with time, due to its coupling with other modes, and also due to diffusion. The formalism of non-linear fluctuating hydrodynamics allows us to understand the long time decay of these local fluctuations.

An useful quantity to study how local perturbations in the system decay in the limit of large space and time, is the dynamical structure function $C_{\alpha\alpha}(x, t) = \langle \phi_\alpha(0, 0) \phi_\alpha(x, t) \rangle$. Starting from Eq. 1.5 the time-evolution of $C_{\alpha\alpha}(x, t)$, or equivalently the mode-coupling equation can be constructed and the scaling ansatz 1.2 can be made [45]. Here, $f_\alpha(y)$ is the scaling function and the scaling variable $y = (x - \lambda_\alpha t) / t^{1/z_\alpha}$ indicates that at time t the perturbation is peaked around the position $x(t) = x(0) - \lambda_\alpha t$ and the width of the peak scales as t^{1/z_α} . It is assumed that the spreading is sub-ballistic, *i.e.* $z_\alpha > 1$. In the case when each of the eigenvalues of the matrix \mathbf{A}^0 are different, the modes also propagate with different speeds, which means that the cross-correlation between two modes $C_{\alpha\beta}(x, t) = \langle \phi_\alpha(0, 0) \phi_\beta(x, t) \rangle$ can be neglected at large times.

Taking Fourier transform in space Eq. 1.2 gives $\tilde{C}_{\alpha\alpha}(k, t) \sim e^{-i\lambda_\alpha k t} \tilde{f}_\alpha(kt^{1/z_\alpha})$, and subsequent Laplace transform in time changes the scaling variable to $\zeta_\alpha = (\omega + i\lambda_\alpha k) |k|^{-z_\alpha}$ and the dynamical structure function can be written as,

$$\hat{C}_{\alpha\alpha}(k, \zeta_\alpha) = \frac{1}{\sqrt{2\pi}} |k|^{-z_\alpha} h_\alpha(\zeta_\alpha). \quad (1.7)$$

This ansatz can be used to solve the mode coupling equation and the scaling function comes out to be [45],

$$\frac{1}{h_\alpha(\zeta_\alpha)} = \lim_{k \rightarrow 0} \left[\zeta_\alpha + D_\alpha |k|^{2-z_\alpha} + Q_{\alpha\alpha} \zeta_\alpha^{\frac{1}{z_\alpha}-1} |k|^{3-2z_\alpha} + \sum_{\beta \neq \alpha} Q_{\alpha\beta} (-i\lambda_k^{\alpha\beta})^{\frac{1}{z_\beta}-1} |k|^{1+\frac{1}{z_\beta}-z_\alpha} \right] \quad (1.8)$$

with coefficient $Q_{\alpha\beta}$ proportional to $(G_{\beta\beta}^\alpha)^2$ and $\lambda_k^{\alpha\beta} = (\lambda_\alpha - \lambda_\beta) \text{sgn}(k)$. In order to have a non-trivial scaling limit, we must ensure that in the limit of small k the scaling function $h_\alpha(\zeta_\alpha)$ stays finite and $h_\alpha(\zeta_\alpha) \neq 1/\zeta_\alpha$. Note that $h_\alpha(\zeta_\alpha) = 1/\zeta_\alpha$ would mean dissipationless transport of density perturbation as predicted from the linear theory. We briefly discuss below how these two criteria determine the value of the dynamical exponent z_α and the form of the scaling function.

Case A: When all diagonal terms of \mathbf{G}^α vanish, $G_{\beta\beta}^\alpha = 0 \forall \beta$, then last two terms on the right hand side of Eq. 1.8 drop out. The resulting scaling function will be non-trivial only if $z_\alpha = 2$, which gives $h_\alpha(\zeta_\alpha) = [\zeta_\alpha + D_\alpha]^{-1}$. This corresponds to,

$$\tilde{C}_{\alpha\alpha}(k, t) = \frac{1}{\sqrt{2\pi}} e^{-i\lambda_\alpha k t - D_\alpha k^2 t} \quad (1.9)$$

This gives a diffusive universality class for the mode α . In absence of self-coupling and cross-coupling between the modes, any local perturbation moves around the system with speed λ_α and dissipates diffusively.

Case B: In case $G_{\alpha\alpha}^\alpha = 0$, but there is at least one β for which $G_{\beta\beta}^\alpha \neq 0$, then Eq. 1.8 becomes,

$$\frac{1}{h_\alpha(\zeta_\alpha)} = \lim_{k \rightarrow 0} \left[\zeta_\alpha + D_\alpha |k|^{2-z_\alpha} + \sum_{\beta \neq \alpha} Q_{\alpha\beta} (-i\lambda_k^{\alpha\beta})^{\frac{1}{z_\beta}-1} |k|^{1+\frac{1}{z_\beta}-z_\alpha} \right] \quad (1.10)$$

Now, we have already assumed that $z_\alpha > 1$, and hence $1 + \frac{1}{z_\beta} - z_\alpha < 2 - z_\alpha$ which means in the limit of small k the second term in the rhs of Eq. 1.10 vanishes faster and the scaling behavior is dominated by the slowest decaying term in the summation present in the third term *i.e.* $z_\alpha = 1 + \frac{1}{z_\beta^{\max}}$. Note that this result is consistent with the assumption that $z_\alpha > 1$. The dynamic structure function in momentum space in this case,

$$\tilde{C}_{\alpha\alpha}(k, t) = \frac{1}{\sqrt{2\pi}} \exp \left[-i\lambda_\alpha kt - \sum_{\beta \in \{z_\beta = z_\beta^{\max}\}} Q_{\alpha\beta} (-i\lambda_k^{\alpha\beta})^{1/z_\beta^{\max}-1} |k|^{1+1/z_\beta^{\max}} t \right] \quad (1.11)$$

Eq. 1.11 shows the long time decay of the local fluctuations when mode α has cross-coupling with other modes but has no self-coupling term.

Case C: Finally, we consider the most general case of non-vanishing self-coupling and cross-coupling, $G_{\alpha\alpha}^\alpha \neq 0$ and $G_{\alpha\beta}^\alpha \neq 0$ for at least one $\beta \neq \alpha$. In this case all four terms on the right hand side of Eq. 1.8 are present. Depending on which term dominates the small k behavior, we can have either $z_\alpha = 2$, or $z_\alpha = 3/2$, or $z_\alpha = 1 + 1/z_\beta^{\max}$. Thus we can rule out the possibility of $z_\alpha > 2$ even in the presence of self-coupling. Moreover, in order to make sure that the right hand side of Eq. 1.8 does not diverge in the limit of small k , we must have non-negative exponents of k in the diffusive term, self-coupling term and cross-coupling term. This is possible only if $z_\alpha = \min[2, 3/2, 1 + 1/z_\beta^{\max}] = 3/2$. The corresponding scaling function can be of two different types. If mode α is not cross-coupled to any diffusive mode, *i.e.* $z_\beta^{\max} < 2$, then only the self-coupling term dominates the small k behavior and the scaling function is given by,

$$h_\alpha(\zeta_\alpha) = [\zeta_\alpha + Q_{\alpha\alpha} \zeta_\alpha^{-\frac{1}{3}}]^{-1}. \quad (1.12)$$

This is known as the usual KPZ universality class [46]. However, if $z_\beta^{\max} = 2$, then the cross-coupling term also affects the scaling function and we have ,

$$h_\alpha(\zeta_\alpha) = [\zeta_\alpha + Q_{\alpha\alpha} \zeta_\alpha^{-\frac{1}{3}} + \sum_{\beta \in \{z_\beta=2\}} Q_{\alpha\beta} (-i\lambda_k^{\alpha\beta})^{-\frac{1}{2}}]^{-1} \quad (1.13)$$

which is known as modified KPZ universality class [40]. This is a distinctly different universality class and can not be described by Prähofer-Spohn scaling function.

1.3 MOTIVATION AND FOCUS OF THESIS

In this thesis, we study a particle-landscape model similar in its setting to that of [24, 25] where there are two sets of particles (heavy and light) moving stochastically on a fluctuating landscape. The heavy (H) particles show a tendency to cluster towards the local potential minima present in the landscape, while the lighter (L) particles tend to rise up. While doing so, the H and L particles modify the shape of the landscape differently. By tuning the coupling parameters that govern the action of the H and L particles on the landscape, we obtain a phase diagram that shows two new kinds of ordered phases in both particle species and also the landscape, along with the earlier found SPS and FDPO phases, and a disordered phase. The phase diagram remains qualitatively valid in both one and two dimensions. We characterise the static and dynamic properties of the ordered phases and observe that the newly found phases are completely different in nature from the earlier examples of coupling-induced phase separation [47–49]. This indicates that the difference in nature of coupling alone can give rise to significantly different ordered states with rich static and dynamical properties. Moreover, it might also crucially change the time-scales of coarsening to such ordered phases.

Additionally, our model shows a disordered phase for a broad parameter regime that we characterise. In this phase, neither the particles nor the landscape show long-ranged order. Nevertheless, there are short-ranged correlations present in the steady state, whose exact forms are unknown. The coupling between the particles and the landscape gives rise to wave-like propagating modes of fluctuations which are coupled at the non-linear level. Using the recently developed formalism of non-linear fluctuating hydrodynamics (NLFH) along with mode-coupling theory that has been discussed in Sec 1.2, we study the dynamical properties of the disordered phase observed in our model. In our work, we aim at carrying the out the NLFH formalism starting from an approximate knowledge of the steady state, and numerically verify the catalogue of universality classes predicted by mode coupling theory for our model. However, we argue that in verifying the predictions through numerical simulations, the conclusions can be masked by finite size effects.

1.4 SYNOPSIS OF MAIN RESULTS AND PLAN OF THESIS

In this section we present the brief summaries of each of the chapters of this thesis. Chapter 2 gives an overview of the phase diagram that reveals novel phases on tuning the particle-

landscape couplings. Chapters 3, 4, and 5 focus on the static and dynamic characterisation of the ordered phases in one and two dimensions. Chapter 6 is based on our work on the disordered phase that has been studied using the NLFH framework described in Sec. 1.2.

1.4.1 Chapter 2: Summary

In Chapter 2, we first introduce our model of a set of sliding particles on a fluctuating landscape and discuss a phase diagram which is obtained on tuning the particle-landscape couplings. We use a simple linear stability analysis to obtain a condition of having phase separation in the system. The model shows three different well-ordered phases: strong phase separation (SPS), infinitesimal current with phase separation (IPS) and finite current with phase separation (FPS). In all three phases, the H and L particles undergo complete phase separation; the phases differ from each other in the nature of the ordering exhibited by the landscape. In addition, there are two other phases, one of which is disordered with short-ranged correlations while the other shows fluctuation-dominated phase ordering (FDPO) [27]. The new ordered phases found here are quintessentially nonequilibrium; the phase separated states exhibit qualitatively different types of ordering for the particles and landscape, quite unlike systems known earlier. In particular, particles display strong phase separation [24] characterized by pure, fluctuationless phases, which cohabit with three macroscopic regions of the surface, two of which possess long-range order, while the third does not. These findings differ markedly from the strongly phase separated states found earlier in the LR and ABC models [24, 26] and imply strong changes for both static and dynamical properties.

1.4.2 Chapter 3: Summary

In Chapter 3, we discuss our results on the static characterisation of the ordered phases shown by the phase diagram. SPS (Strong phase separation) occurs when the H particles impart a downward push to the landscape, while the L particles impart an upward push. This results in a complete phase separation between the H and L particles, and between the positive and negative height gradient regions of the landscape as well. This is the phase studied in the Lahiri-Ramaswamy model of sedimenting colloidal crystals [24] that has been mentioned briefly in Sec. 1.1. The pure domains of positive and negative slope form a deep ∇ -shaped valley holding the H -cluster, while its mirror image \wedge holds the L -cluster. We show that the entire parameter regime marked by SPS shows logarithmically slow coarsening in time due to formation of metastable states in course of relaxation. In [25] it was shown that with some conditions on the rates, the steady state measure is given by a Boltzmann factor involving a long-ranged Hamiltonian for particular choice of densities. In Chapter 3, we

show that this can now be generalized to the case of an arbitrary densities of the H particles, for which the form of the Hamiltonian is derived. Further, by rescaling rates downward by a factor proportional to the system size, a mean field calculation points to a finite temperature phase transition from a disordered phase to one with long range order. This result is supported by numerical simulations of the model.

A completely new kind of phase separation IPS (Infinitesimal current with Phase Separation) is obtained when the H particles tend to push the landscape downward, while the L particles do not impart any local bias to the landscape dynamics. In the steady state, the H and L species undergo complete phase separation as in the SPS phase. However, unlike SPS, the landscape is long-range ordered only in the region that holds the H -cluster, where it forms a deep valley consisting of macroscopic pure domains of positive and negative slope regions. The remaining part of the landscape beneath the L -cluster is not ordered and assumes a rough shape. Notably, the approach to this steady state is rapid, with a coarsening time that grows as a power law of size, as opposed to the much slower time-scales diverging exponentially with system size that were found earlier [24, 26]. Further, in steady state, there is a current of macroscopic tilt (slope) variables through the system with periodic boundary conditions. A suitable mapping shows that this movement is well described as a SEP (symmetric exclusion process) with input and exit of particles at the two ends of the L -region [50, 51]. The value of this current scales inversely with the system size N , implying that for large system size, the entire system falls downward at an infinitesimal rate. This accounts for the earlier nomenclature (Infinitesimal fall with phase separation) used for this phase [47]. Using the Kolmogorov loop condition [52] for equilibrium, we demonstrate the breakdown of detailed balance in this case. A rescaling of the rates with the system size shows that there is a possibility of having a phase transition in the IPS phase as well. Further, it is shown that a single H particle in a system of $(N - 1)$ particles of type L , leads to a non-trivial landscape profile and a current of order $1/N$. Next, the tendency of particles to cluster is demonstrated by considering a system of two H particles and calculating the energy as a function of separation, in the adiabatic limit of vanishingly small rates for particle movement. Finally, detailed numerical evidence is gathered in support of the description of the landscape in the L region as a SEP with boundary injection.

FPS (Finite current with phase separation) sets in when both H and L particles push the landscape downwards, but the latter at a lower rate than the former. As in the IPS phase, the H and L species segregate into pure phases and the landscape forms a macroscopic valley holding the H cluster while the part beneath the L cluster is disordered. However, unlike the IPS phase, the two arms of the macroscopic valley now have a slope of magnitude less than unity, corresponding to a finite fraction of both tilt species being present in both the arms. The entire system carries a finite current of tilts in the steady state, resulting in a net downward motion with finite velocity. The movement of microscopic tilts in the L -region

resembles the movement of particles and holes in the well-known ASEP (asymmetric simple exclusion process), with boundary injection [20]. The fact that the steady state tilt current must be uniform across regions, allows us, at the level of mean field theory, to relate the slopes of the arms in the H region to the tilt current in the L region. This value of the slope is shown to be close to that obtained by numerical simulations. Further, the argued-for correspondence of the surface in the L region and the ASEP is tested by numerical simulations. Results conform surprisingly well with the maximal current phase of the ASEP, including for instance the power laws which characterize the density profiles near the edges.

1.4.3 Chapter 4: Summary

Chapter 4 focusses on the dynamic properties of the phases highlighting the basic point that the different types of ordering of the landscape result in very different dependence of time-scales on the system size N . In the SPS phase, motion of the interface between the coexisting phases involve an ‘ergodic’ time-scale, growing exponentially with N , so that there is no perceptible large-scale movement or rearrangement of the landscape on shorter timescales. By contrast, in the IPS and FPS phases, the coexistence of ordered and disordered landscape phases gives rise to novel steady state dynamics both near the interfaces and close to the bottom of the large valley, on time-scales which grow algebraically with N . To characterize this dynamics, we propose a scaling ansatz and show that our simulation data for various dynamical correlation functions can indeed be described well by this ansatz. We also estimate different scaling exponents that summarize the scaling behavior of each correlation function considered here. In [48] it was noted that the properties of the landscape in the L -region has certain similarities with open systems. We examine this issue further and show that there is a quantitative matching between the dynamics of the landscape in the L -region with that of an open-chain symmetric (asymmetric) exclusion process for the IPS (FPS) phase.

1.4.4 Chapter 5: Summary

The phase diagram discussed in Chapter 2 remains qualitatively same in two dimensions as well. In Chapter 5, we present our study of our model in two dimensions for two different types of lattice geometries. For a square lattice, in the ordered phases, the landscape organizes itself in algebraic time to form a valley with a diamond-shaped cross section, which supports the H -cluster. However, there is an interesting finite-size effect, which gives rise to a different topology of the landscape for smaller systems. Instead of a deep valley with a single minimum, the landscape develops a line of minima and assumes the shape of a trench. Using a scaling argument, we show that in the thermodynamic limit, such configura-

tions are energetically unfavorable in comparison to the diamond-shaped single valley. For a triangular lattice we encounter similar kind of finite size effects where we find three different kinds of topologies — hexagonal, trench, and triangular. However, we argue that the energy scaling argument fails to work at high densities because of strong finite size effects and boundary contributions. In Chapter 5 we also explore the steady state dynamics on a two dimensional square lattice.

1.4.5 Chapter 6: Summary

Chapter 6 focusses on the disordered phase. Specifically, we are interested in how the coupled time-evolution of particle density and landscape height gradient gives rise to different dynamical universality classes in the system, following the prescription of NLFH described in Sec. 1.2. However, unlike most NLFH studies so far, the exact steady state measure is not known for our system. Although, in the disordered phase neither the particles nor the landscape show any long ranged order, there are still short-ranged correlations present in the system whose exact form is not known. Therefore, in this case we rely on approximate expressions based on mean-field theory where we neglect all correlations in the system or a slightly improved approximation where we retain some nearest neighbor or next nearest neighbor correlations and ignore the rest. Using this approximate expression for current we carry out the analysis of NLFH and derive the condition for observing different dynamical universality classes. Finally, we check our analytical predictions with numerical simulations. Our study shows that our system has rich dynamics in the disordered phase. Starting from approximate expressions of the currents, mode coupling theory along with NLFH predicts the possibility of having diffusive, KPZ, $3/2$ -Lévy, $5/3$ -Lévy, and golden mean universality classes in our system. However, we argue that not all of them are possible to observe numerically as our observations are severely plagued by finite size effects. To the best of our knowledge, this is the first ever study where NLFH has been used in absence of exact knowledge of current-density relationship.

PHASE DIAGRAM FOR A COUPLED NON-EQUILIBRIUM SYSTEM OF PARTICLES ON A FLUCTUATING LANDSCAPE

2.1 INTRODUCTION

In this chapter, we derive the phase diagram obtained by tuning the coupling strength between the components of a coupled non-equilibrium system. The system here can be simplistically described as to consist of two sets of particles performing damped motion under gravity on a fluctuating landscape. The model allows one to tune the interaction between the landscape and the particles. In the process, novel non-equilibrium phases of particles with compact clustering and rich, rapid dynamics coexisting with a macroscopically organized landscape is unmasked. The model has partial overlap with the lattice gas model of Lahiri and Ramaswamy (LR) for sedimenting colloidal crystals [24, 25]. Although one of the ordered phases was reported earlier in the context of the LR model, the other phases manifest themselves outside the LR regime. In this chapter we derive the phase diagram and summarily discuss the broad static and dynamic features of each of the phases. The results presented here constitute a brief, qualitative overview of results reported in [47-49], while the detailed discussions on the same are to follow in the subsequent chapters of this thesis.

2.2 MODEL DESCRIPTION

The model consists of two coupled driven diffusive systems, with conserved quantities. This is a lattice model of H (heavier) and L (lighter) particles performing damped motion under gravity on a fluctuating surface, thus justifying the name LH (Light-Heavy) model. The model is very similar in its setting to the LR model [24, 25]. The system is modelled on a periodic lattice of size N . Each of the lattice sites can accommodate atmost one heavy (H) or one light (L) particle, while each of the lattice bonds representing the discrete surface elements can have an orientation or 'tilt' of $\pm\pi/4$. The occupancy of the i^{th} lattice site is denoted by σ_i which assumes value 1(0) for an H (L) particle, while the tilt of the i^{th} bond is given by $\tau_{i+1/2}$ which takes value $(+1)(-1)$ according as the bond being an up (down)-

tilt. The local dynamics of the particles and the surface are coupled: H and L particles at neighboring sites may interchange locations, and do so preferentially if the local tilt of the surface favors a downward move for H . Particles reside on lattice sites and interact via hard-core exclusion: a site holds at most one particle (H or L) and there are no holes. Hence, if ρ_H and ρ_L are the average densities of the H and L species respectively, then $\rho_H = 1 - \rho_L$. Hence, it suffices to work with a single variable ρ that denotes average density of the H particles in the system. If the symbols $/$ and \backslash indicate upward and downward tilts of the surface, respectively, then the particles follow the dynamics:

$$\begin{aligned}
W(H\backslash L \rightarrow L\backslash H) &= D + a \\
W(L\backslash H \rightarrow H\backslash L) &= D - a \\
W(H/L \rightarrow L/H) &= D - a \\
W(L/H \rightarrow H/L) &= D + a
\end{aligned} \tag{2.1}$$

where W denotes the probability per unit time for a particular process to occur. This dynamics conserves the total number of H (and L) particles. Under the action of the H and L particles, a local hill (\wedge) on the surface might get pushed downward, or a valley (\vee) upward. In one dimension surface dynamics can be represented as,

$$\begin{aligned}
W(/H\backslash \rightarrow \backslash H/) &= E + b \\
W(\backslash H/ \rightarrow /H\backslash) &= E - b \\
W(/L\backslash \rightarrow \backslash L/) &= E - b' \\
W(\backslash L/ \rightarrow /L\backslash) &= E + b'
\end{aligned} \tag{2.2}$$

The dynamics conserves the overall slope *i.e.* $\frac{1}{N} \sum_i \frac{1+\tau_{i+1/2}}{2} = m$, where m denotes the fraction of up-slopes in the surface. We use periodic boundary conditions so that,

$$\sigma_i = \sigma_{i+N}, \quad \tau_{i+1/2} = \tau_{i+1/2+N} \tag{2.3}$$

In characterizing the ordered phases, we have mostly considered $m = 1/2$, *i.e.*, no overall slope in the landscape although our results remain valid for all particle and bond densities. In the disordered part of the phase diagram, however, we have also considered $m \neq 1/2$. Figure 2.1 shows the phase diagram of the system in the scaled $b - b'$ plane, with $a = 0.5$. However, the qualitative features of the phase diagram remains same for any $a > 0$. We present a brief overview of all the phases shown in the diagram in the rest of this chapter.

2.3 PHASE DIAGRAM

As we vary the transition rates in Eqs. 2.1 and 2.2, we encounter different phases. The variation is restricted to the regime in which the parameter a in these equations remain positive. In other words, the H particles always show a tendency to slide downhill. The constants b, b' , on the other hand, can be positive, negative, or zero. The differential action of the H and L particles on the landscape have macroscopic consequences, and result in different phases.

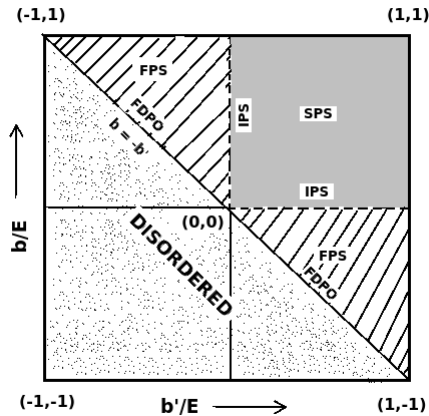


Figure 2.1: Phase diagram in the scaled $b - b'$ plane. For $b > 0$ and $b' > 0$, the system shows SPS. The dotted horizontal and vertical lines are related to each other via interchange of the two particle species. On these lines the system is in IPS phase. The striped region ($-b < b' < 0$) in the 2nd and 4th quadrants represent FPS phase and are connected by $H - L$ exchange symmetry. $b = -b'$ line corresponds to FDPO phase. The dotted region beyond $b = -b'$ line correspond to disordered phase.

Fig. 2.1 shows that the $b' = -b$ line acts as the boundary between ordered and disordered phases. This can be also be seen directly from a linear stability analysis of the corresponding continuum theory, describing the system as a coupled time evolution of two conserved fields, the density field of the particles and the tilt field (or height gradient) of the landscape. One can write down the continuity equations in terms of the particle current and the tilt current. The particle current can be denoted by the difference in the rightward and leftward fluxes of the H -particles per unit time, while the bond current by the difference between the rightward and leftward fluxes of the up-tilts per unit time in the stationary state. Denoting the coarse-grained particle density as $\rho(x, t)$ and landscape height gradient as $m(x, t)$, the corresponding currents within mean-field approximation are given by,

$$J_\rho = 2a\rho(x, t)[1 - \rho(x, t)][1 - 2m(x, t)] \quad (2.4)$$

$$J_m = m(x, t)[1 - m(x, t)][2\rho(x, t)(b + b') - 2b'] \quad (2.5)$$

In the disordered phase, the hydrodynamic expansion of $\rho(x, t)$ and $m(x, t)$ about the homogeneous state can be used and only linear terms in $\delta\rho(x, t) = \rho(x, t) - \rho_0$ and $\delta m(x, t) = m(x, t) - m_0$ in the expression for J_ρ and J_m can be retained to get the continuity equation in the form,

$$\partial_t \begin{pmatrix} \delta\rho \\ \delta m \end{pmatrix} = \begin{pmatrix} 0 & -4a\rho_0(1 - \rho_0) \\ (b + b')/2 & 0 \end{pmatrix} \begin{pmatrix} \delta\rho \\ \delta m \end{pmatrix} \quad (2.6)$$

Here, ρ_0 is the average density of the H particles and m_0 is the average value of the slope. Here, we have used the fact that the surface is an untilted one *i.e.* $m_0 = 1/2$. In our model, the coupling between the particles and the landscape is such that the mobility of one species depends on the local density of the other. Our linear stability analysis in this case shows that the eigenvalues of the Jacobian matrix

$$\lambda_{\pm} = \pm \sqrt{-2a\rho_0(1 - \rho_0)(b + b')} \quad (2.7)$$

that enters the continuity equations are real for $b < -b'$, which implies a homogeneous or disordered state for both particles and landscape. These eigenvalues represent the speeds of the kinematic waves of fluctuations described in 1.2. However, for $b > -b'$, the eigenvalues have an imaginary part indicating growth of instability which heralds the onset of ordering. It may be worth mentioning here that the nature of cross-species coupling between the mobility and density is crucial. If instead of depending on the density, the mobility of one species depended on higher derivatives of density of the other species, the results might have been different. In [53] a coupled driven system was studied where the mobility of one species depended upon the second derivative of the density of the other species. In that case, however, no ordered phase was found, and homogeneous solutions were shown to remain valid for all parameter regimes.

For $b, b' > 0$, the part of the surface containing L particles has a bias to move upward; this results in an SPS phase. For the SPS phase, the system exhibits the purest form of ordering where all the different species in the system, *e.g.*, H, L , up-slopes and down-slopes completely phase separate. For $b > 0$ and $b' = 0$, the landscape beneath the L particles has unbiased local fluctuations, and on the macroscopic scale an IPS phase results. In this case, the particle species still remain completely phase separated. However, although the part of landscape holding the H -cluster shows pure phase, the landscape beneath the L -cluster is devoid of any pure domains and show a linear gradient in density. Moving further anticlockwise into the phase diagram, for $-b < b' < 0$, the L particles push the landscape downward, but with a rate smaller than the H particles do, and we have an FPS phase. In the FPS phase, there are no pure domains present in the landscape although the purity of the particle phases is

still retained. The limit $b' = -b$, corresponds to the case when H and L particles behave identically and we have an FDPO state, characterized by weak phase ordering among the particles and a product-measured landscape [27]. For $-b > b'$, the L particles push the surface downward at a larger rate than H particles and in this case neither the landscape nor the particles show any long-ranged ordering and the system is in a disordered phase. A brief description of the different phases is tabulated in the table below and a figure showing typical configurations of each of the phases is shown in Fig 2.2.

Phase	Condition	Particles	Landscape	Downward velocity
(a)SPS	$b' > 0$	Single, compact, macroscopic H and L clusters	Complete phase separation of up-slope and down-slope bonds	$\sim \exp(-\alpha N)$
(b)IPS	$b' = 0$		Deep valley beneath H cluster and disordered slopes with gradient $\sim 1/N$ below L cluster	$\sim 1/N$
(c)FPS	$-b < b' < 0$		Partial phase separation of slopes beneath H cluster and disordered beneath L cluster	Finite
(d)FDPO	$b' = -b$	Compact macroscopic clusters of fluctuating lengths	Disordered	Finite
(e) Disordered	$-b > b'$	No macroscopic clusters	Disordered	Finite

Table 2.1: Different phases observed in the LH model and their qualitative descriptions.

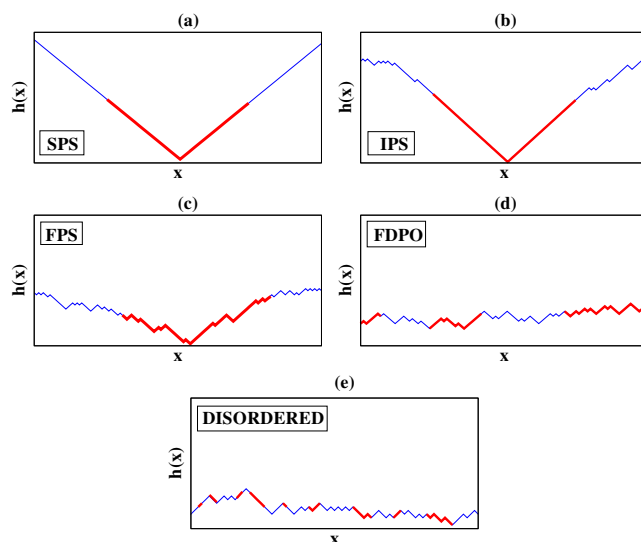


Figure 2.2: We show typical configurations of our system in each of the phases. The thick lines represent the region occupied by the H -particles while remaining parts are occupied by L -particles.

2.3.1 Strong phase separation(SPS)

The grey region of the phase diagram, where $b, b' > 0$, corresponds to the strongly phases separated (SPS) states reported by Lahiri et. al. [24, 25], as appropriate to sedimenting colloidal crystals. In this regime, the light particles tend to move the surface upward whereas

the heavier particles tend to push the surface around them, downwards. In steady state, the up-slope and down-slope surface bonds phase separate to form a single macroscopic valley and hill, which hold all the H and L particles, respectively, in separated clusters (see Fig. 2.2(a)). Both particles and tilts show strong phase separation (SPS). This phenomenon is known as strong phase separation because the ordered states survive even at arbitrarily high temperatures. In this context, the notion of a temperature in the system can be introduced in the form of $\frac{D-a}{D+a} = q = e^{-\beta}$ where, $\beta = 1/T$. For $q \neq 0$, the H particles gain a non-vanishing rate of climbing uphill. However, for $a > 0$, the value of q always remains less than 1, which signifies that the H 's always have a higher tendency to slide down towards any local minimum present in the landscape. In these class of systems, for any $q < 1$, sufficiently away from the domain boundaries, pure domains that scale with the size of the system, can always be found. For these systems when domain merging can take place at high temperatures, the coarsening process is found to be logarithmically slow, due to existence of meta-stable states whose lifetime diverges exponentially with the system size N .

We observe [47] in this phase that for particular choices of the rates, the system satisfies detailed balance and in the steady state, satisfies Boltzmann measure $\sim \exp(-\beta\mathcal{H})$ with respect to a Hamiltonian containing long-ranged interactions. We present a detailed proof for this in the next chapter. The long-ranged interactions in the Hamiltonian give rise to energy that scales as N^2 and hence for any non-zero β , or equivalently, any $q < 1$, the system shows SPS: the up-slope and down-slope surface bonds phase separate to form a single deep valley and all the particles are present inside that valley in a single cluster.

2.3.2 Infinitesimal current with phase separation(IPS)

The $b > 0$, $b' = 0$ case corresponds to the IPS phase which is obtained along the dashed lines of the phase diagram in Fig. 2.1. In this case, the local fluctuations in the surface occupied by L particles are of the symmetric Edwards-Wilkinson type [37], while the H particles continue to push the surface down. In the steady state, the H and L species undergo complete phase separation as in the SPS phase. However, the entire landscape does not show phase separation as in the SPS phase — while the part holding the H -cluster forms a deep valley consisting of pure macroscopic domains of up and down-slope bonds, the rest of it beneath the L -cluster is not ordered and the bonds to show a $1/N$ density gradient (see Fig. 2.2(b)). In this phase, unlike the SPS phase, the detailed balance breaks down for all densities and the system carries a net current scaling inversely as the system size. The steady state current in the system manifests itself in a downward motion of the entire landscape with an average velocity $1/N$ for a lattice of size N and hence the name infinitesimal fall with phase separation. Contrary to the SPS phase, where metastable states result in logarithmically slow

coarsening process, the relaxation to an IPS phase takes place algebraically fast ($t \sim N^2$) as we shall see in more details in Chapter 3. We carry out the static characterisation of the IPS phase in Chapter 3 by measuring the density profiles of the particles and bonds which show that in steady state, the landscape beneath the L -cluster can be viewed as an open chain symmetric exclusion process [50, 51]. The detailed correspondence of the static and dynamic aspects of the IPS phase with an open chain SEP will be carried out in Chapters 3 and 4. The coexistence of an ordered valley along with the symmetrically fluctuating part of the landscape, gives rise to rich steady state dynamics with time-scales growing algebraically with N for the landscape, and exponentially with N for the particles.

2.3.3 Finite current with phase separation(FPS)

The FPS phase sets in for $b > 0$ and $-b < b' < 0$ when both H and the L 's push the landscape downwards, but the latter at a lower rate than the former. As in the SPS and IPS phases, the H and L species segregate into pure phases. The landscape forms a macroscopic valley holding the H cluster while the part beneath the L cluster is disordered — unlike in the SPS and IPS phases, the two arms of the macroscopic valley now have a slope of magnitude less than unity, corresponding to a finite fraction of both tilts being present in both the arms (see Fig. 2.2(c)). The presence of a finite tilt current through the system results in a finite downward velocity of the surface and in steady state, the entire surface moves downward at finite speed, preserving the macroscopic valley and disordered tilt region, along with the pure domains of H and L particles. By measuring the density profiles of the upslope bonds, we identify the landscape beneath the L -cluster to be in the maximal current phase in an open-chain asymmetric exclusion process [20]. Similar to the IPS phase, the coarsening to the FPS phase happens in an algebraic time $\sim N^2$.

2.3.4 The disordered phase

In the disordered region shown in Fig. 2.1, neither the particle species nor the tilts shows long-range order. However, there are finite, short-ranged correlations present everywhere in this phase except at a particular point in the phase diagram where the system obeys product measure [54]. In all of the ordered phases described so far, the particles remain static and hence, the steady state particle current J_ρ is zero. The landscape, on the other hand, undulates beneath the particle clusters and gives rise to bond current J_m that scales inversely as the system size in the IPS phase and remain finite in the FPS phase. On contrary, in the disordered phase, both J_ρ and J_m are finite. With knowledge of the current-density relationship $[(J_\rho, J_m) \text{ vs. } (\rho, m)]$ in the system, one may write down the linearised continuity

equations (see Sec. 1.2). The eigenvalues of the Jacobian matrix \mathbf{A} (Eq. 1.4) represent constant speeds at which the fluctuations in the density fields travel around the system. Using suitable linear combination of the fields, one can construct normal modes which are decoupled at the linear level. The non-linear coupling between these propagating modes governs their dissipation in space and time and also their scaling forms. Following the formalism using non-linear fluctuating hydrodynamics and mode coupling theory that has been described in Chapter 1, we try to characterise these propagating and dissipating modes in the disordered part of the phase diagram. However, for our system, the closed form expressions for the short-ranged correlations are not known. As a consequence, due to lack of knowledge of exact expressions of current-density relationship, we rely on approximate expressions for current to carry out the formalism described in Sec. 1.2 and calculate the mode coupling matrices 1.6. We check the final predictions of NLFH through numerical simulations and present our results on the disordered phase in Chapter 6.

2.4 CONCLUSION

In this chapter, we have explained our model of two coupled species that exhibits different ordered phases and explicitly demonstrated how the coupling affects the qualitative nature of the ordering. The model is that of a lighter and a heavier particle species moving on a potential energy landscape. The particles try to lower the potential energy, and in occupying valleys in the landscape, the heavier species always gets preference over the lighter one. Most importantly, the particles also affect the landscape locally, so as to lower the energy further. Depending on how each species interacts with the landscape, we find three different ordered phases (SPS, IPS, and FPS) that show long-ranged order in both particles and the landscape, a phase where the landscape is disordered but the particles show weak ordering (FDPO), and a disordered phase where the particles and the landscape show finite, short-ranged correlations. in the system. We present detailed characterisation of the phases in the subsequent chapters of this thesis.

STATIC PROPERTIES OF ORDERED PHASES IN THE LH MODEL

3.1 INTRODUCTION

In this chapter, we demonstrate and discuss the static features of different emergent phases in a coupled driven system in which two species of particles are advected by a fluctuating potential energy landscape. Due to the two-way coupling between the landscape and the particles, the system shows new interesting phases, characterized by different sorts of long-ranged order in the particles and in the landscape. In all these ordered phases, the two particle species L and H phase separate completely from each other, but the underlying landscape may either show complete ordering, or may show coexistence of ordered and disordered segments, depending on the differential nature of effect produced by the particle species on the landscape. We discuss several aspects of static properties of these phases in one dimension. Results presented in this chapter have been reported in [48].

3.2 STATIC CHARACTERISATION OF THE ORDERED PHASES

In this chapter, we present our results on the static characterisation of the ordered phases obtained in the particle-landscape model that have qualitatively been discussed in Chapter 2. As described in Sec. 2.2, the $L - H$ model consists of two coupled systems with conserved components. The system describes two species of particles moving stochastically on a fluctuating energy landscape, one species being lighter (L) while the other heavier (H). The particles tend to minimize their energy by moving along the local potential gradient and also by modifying the landscape around their position to further lower the energy. Generically, the H particles preferentially displace the L particles while sliding downward along the landscape. Further, each species affects the local landscape dynamics differently.

In Chapter 2, we have already shown the phase diagram in the $b - b'$ plane depicting the different phases in our model (see Fig. 2.1). In Fig. 3.1, we present an alternative representation of the same phase diagram and explain.

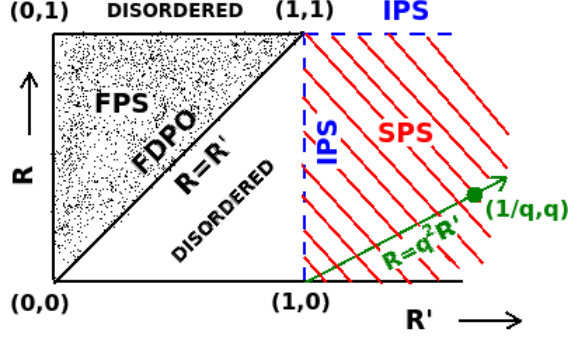


Figure 3.1: Phase diagram in the $R - R'$ plane, where $R = \frac{E - b}{E + b}$ and $R' = \frac{E + b'}{E - b'}$ with model parameters E, b and b' defined in Eq. 2.2 as part of model description in Chapter 2. Here, $R > 1$ ($R' < 1$) indicates a downward bias imparted by H (L) particles on the landscape, and $R' > 1$ indicates that L particles push the landscape upward. For $1 < R' < \infty$, one has the SPS phase. In this regime, detailed balance is satisfied in the system on the straight line $R = q^2 R'$ where, $q = (D - a)/(D + a)$. The LR model is shown by a solid circle on this line. The dashed lines shown in the diagram correspond to the IPS phase. The dotted region corresponds to the FPS phase ($R' < R < 1$), while the white region corresponds to the disordered phase ($R < R' < 1$). Disordered phase is also seen when $R' < 1$ and $R = 1$. For $R = R' < 1$ FDPO phase is observed.

On varying the transition rates in Eqs. 2.1 and 2.2, we encounter different phases. For now, we restrict this variation to the regime in which the parameters a and b in these equations remain positive. In other words, the H particles always show a tendency to slide downhill and push the landscape downward. The ratio,

$$R = \frac{E - b}{E + b} \quad (3.1)$$

then always remains bounded between 0 and 1. The constant b' , on the other hand, can be positive, negative, or zero and the ratio,

$$R' = \frac{E + b'}{E - b'} \quad (3.2)$$

can assume any value between 0 and ∞ . The differences in the action of the L particles have macroscopic consequences, and result in different phases.

For $b' > 0$, or $1 < R' < \infty$ the part of the surface containing L particles has a bias to move upward; the macroscopic consequence is that an SPS phase is obtained. For $b' = 0$, or $R' = 1$, the landscape beneath the L particles has unbiased local fluctuations, and on the macroscopic scale an IPS phase is encountered. For $-b < b' < 0$, or $R' < R$, the L particles push the landscape downward, but with a rate smaller than the H particles do, and we have an FPS phase. The limit $b' = -b$, or $R = R'$ corresponds to the case when H and L particles behave identically and we have an FDPO state, characterized by weak phase

ordering among the particles and a disordered landscape. For $-b > b'$, the L particles push the surface downward at a larger rate than H particles and in this case neither the landscape nor the particles show any ordering and the system is in a homogeneous or disordered phase. Fig. 3.1 shows the phase diagram of the system in the $R - R'$ plane. In the remaining part of this chapter, we discuss several static aspects of the different ordered phases in detail.

3.3 SPS (STRONG PHASE SEPARATION) PHASE [$b' > 0$]

In the striped part of the phase diagram ($R' > 1$), the model is identical to that considered by Lahiri and Ramaswamy [24, 25] in the context of sedimenting colloidal crystals. In this regime, the system exhibits SPS. While the H 's push the landscape down, the L 's tend to push it upwards. Both particle species and the upslope and downslope bonds of the landscape undergo complete phase separation into a macroscopic valley and a hill that holds the H and the L cluster respectively, as shown in Fig. 2.2(a) [Chapter 2].

3.3.1 Detailed balance in the SPS phase

In [25] it was shown that if the surface is untilted *i.e.* $m = 1/2$ and the density ρ of the H particles is also $1/2$, the condition of detailed balance holds with respect to a Hamiltonian with long-ranged interactions, provided that the rates obey certain criteria. We show below that this result can be generalized to an arbitrary density ρ , with a ρ -dependent condition on the rates. In this case, detailed balance holds and the steady state measure of the system is given by $\sim \exp(-\beta\mathcal{H})$ with respect to the following Hamiltonian:

$$\mathcal{H} = \sum_{i=1}^L (n_i - \lambda) h_i \quad (3.3)$$

where, h_i is the height of the i -th site defined as $h_i = \sum_{j=1}^{i-1} \tau_{j+1/2}$ and n_i is the occupancy of the i -th site which takes the value 1 or 0, according as the site is occupied by an H or an L particle. The parameter λ may assume any value between 0 and 1 and characterizes the symmetry under interchange of L and H . It suffices to consider the range $0 \leq \lambda \leq 1/2$ as \mathcal{H} remains invariant under $\lambda \rightarrow 1 - \lambda$ and $n_i \rightarrow 1 - n_i$. Figure 3.2 shows the rates of the allowed microscopic moves along with the change of energy they entail. It is easy to see from this figure that the condition of detailed balance is satisfied for the following choice of rates,

$$\frac{D - a}{D + a} = q, \quad \frac{E - b}{E + b} = q^{2-2\lambda}, \quad \frac{E - b'}{E + b'} = q^{2\lambda} \quad (3.4)$$

where $q = e^{-\beta}$. Note that the system is defined on a ring and hence it is translationally invariant. The height h_i , as defined above, is measured with respect to the first site. If the sites are relabelled such that the site k with height $h_k = \delta$ is the new origin, then the height of all the sites are changed as $h'_i = h_i - \delta$. Hence, in order to ensure that the total energy of the configuration does not change as a result of this relabelling, one must have $\lambda = \rho$, where ρ is the total density of H particles. Thus, in the $\lambda - \rho$ plane, it is only along the locus $\lambda = \rho$ that detailed balance holds with \mathcal{H} given by Eq. 3.3. The limit $\lambda = \rho = 1/2$ corresponds to the case considered in [25] for the Lahiri-Ramaswamy model.

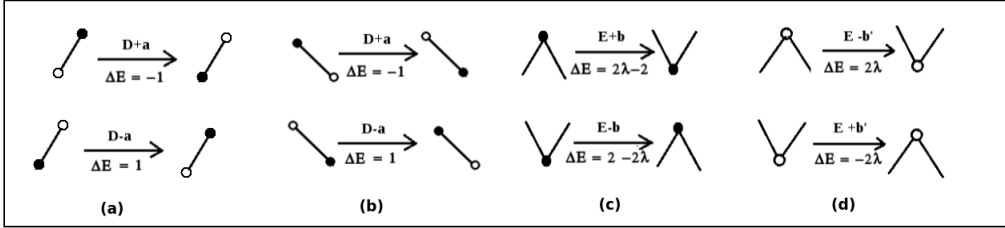


Figure 3.2: Schematic representation of different transitions that are allowed to occur in the system. ΔE 's denote the energy costs involved in the transitions, as per the Hamiltonian in Eq. 3.3. Solid (empty) circles represent H (L) particles.

3.3.2 Coarsening in the SPS phase

As found earlier in [24–26], for all the models exhibiting strong phase separation the coarsening process is found to be logarithmically slow, due to existence of metastable states whose lifetimes diverge exponentially with the system size N . In our model, we find that the entire parameter regime marked by stripes in Fig. 3.1 shows SPS where the coarsening is logarithmically slow in time. For $b' > 0$, the landscape occupied by an L -cluster tends to move upwards and forms a hill, while an H -cluster pushes the landscape down and forms a valley. For two adjacent valleys with H -clusters to merge, the time to dissolve the intermediate hill containing the L -cluster grows exponentially with the size of the L -cluster, and hence the final SPS state is reached over a time-scale $e^{\gamma N}$. For estimating the relaxation time, we measure two point density correlation function for the H particles defined as,

$$C(r, t) = \langle \rho_i(t) \rho_{i+r}(t) \rangle - \rho_0^2 \quad (3.5)$$

where, $\rho_i(t)$ is 1(0) if the i^{th} site is occupied by an H (L) particle at time t during the coarsening phase. The angular brackets denote average over initial conditions. ρ_0 denotes the global density of H particles in the system. Figure 3.3 shows the scaling collapse of the equal time

density correlation function for H particles when separations are scaled by the coarsening length scale $\mathcal{L}(t)$, which is found to grow as $\ln(t)$ for two different values of λ .

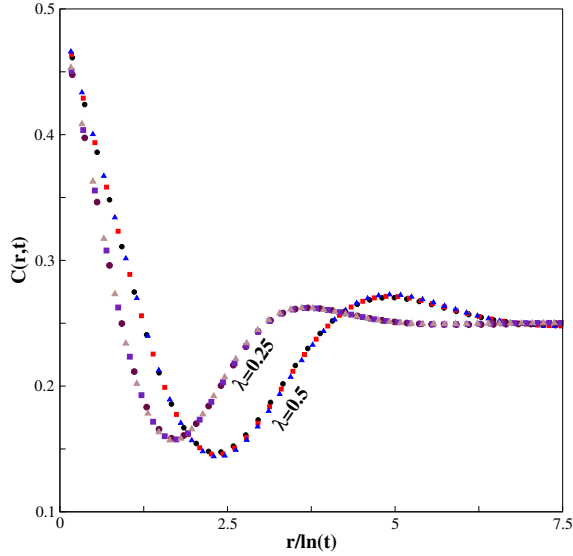


Figure 3.3: Scaling of particle density correlation in the coarsening phase. The equal time density correlation for the particles $C(r, t)$ shows a collapse when r is scaled by $\mathcal{L}(t) \sim \ln(t)$ for two different values of λ .

3.3.3 Rescaled temperature and phase transitions in SPS phase

Although, the Hamiltonian in Eq. 3.3 is defined in terms of local height and local occupancy, the definition of the height field generates long-ranged interactions between n_i and $\tau_{j+1/2}$ in the Hamiltonian. This gives rise to a super-extensive energy that scales as N^2 which at any finite temperature always overrides the extensive entropy term. In other words, as follows from Eq. 3.4, for any non-zero β , or equivalently, any $q < 1$, the H -rich phase has a vanishing fraction of L particles, and vice versa. Such phases are referred to as ‘compact’ as they exclude intermittent islands of the other species. The name ‘strong phase separation’ actually refers to this particular aspect of this phase [24, 25]. However, if the parameter β is rescaled by system size N , *i. e.* $\beta \rightarrow \beta/N$, then the energy and entropy terms become comparable and the system shows an order-disorder transition at a critical β_c [26, 55]. Below, we present a calculation based on mean field theory to provide an estimate of this critical point that matches remarkably well with the numerical simulations in our model.

Let ρ_i denote the probability to find an H particle at site i and $m_{i+1/2}$ denote the probability to find an upslope bond between sites i and $(i + 1)$. Using the dynamical rules described

in section 2.2[see Chapter 2], one can write down the time-evolution equations for these probabilities, within mean-field theory, neglecting all correlations:

$$\begin{aligned} \frac{d\rho_i}{dt} = & \rho_{i-1}(1 - m_{i-1/2})(1 - \rho_i) - \rho_i(1 - m_{i+1/2})(1 - \rho_{i+1}) + q\rho_{i-1}m_{i-1/2}(1 - \rho_i) \\ & - q\rho_im_{i+1/2}(1 - \rho_{i+1}) \end{aligned} \quad (3.6)$$

$$\begin{aligned} \frac{dm_{i+1/2}}{dt} = & m_{i-1/2}\rho_i(1 - m_{i+1/2}) + q^{2-2\lambda}(1 - m_{i+1/2})\rho_{i+1}m_{i+3/2} \\ & + (1 - m_{i+1/2})(1 - \rho_{i+1})m_{i+3/2} + q^{2\lambda}m_{i-1/2}(1 - \rho_i)(1 - m_{i+1/2}) \\ & - m_{i+1/2}\rho_{i+1}(1 - m_{i+3/2}) - q^{2-2\lambda}(1 - m_{i-1/2})\rho_im_{i+1/2} \\ & - (1 - m_{i-1/2})(1 - \rho_i)m_{i+1/2} - q^{2\lambda}m_{i+1/2}(1 - \rho_{i+1})(1 - m_{i+3/2}) \end{aligned} \quad (3.7)$$

Assuming slow spatial variation of ρ and m fields, we can take the continuum limit where $\rho(x), m(x)$ are density profiles at rescaled positions $x = i/N$ and obtain the following expansion:

$$\rho_{i\pm 1} = \rho(x) \pm \frac{1}{N} \frac{\partial \rho(x)}{\partial x} + \frac{1}{2N^2} \frac{\partial^2 \rho(x)}{\partial x^2} + \dots \quad (3.8)$$

Similarly,

$$\begin{aligned} m_{i+3/2} &= m(x) + \frac{1}{N} \frac{\partial m(x)}{\partial x} + \frac{1}{2N^2} \frac{\partial^2 m(x)}{\partial x^2} + \dots \\ m_{i-1/2} &= m(x) - \frac{1}{N} \frac{\partial m(x)}{\partial x} + \frac{1}{2N^2} \frac{\partial^2 m(x)}{\partial x^2} + \dots \end{aligned} \quad (3.9)$$

Next, we write $q = e^{-\beta/N} = 1 - \frac{\beta}{N} + \frac{\beta^2}{2N^2} + \dots$, in which the parameter β has been explicitly scaled by the system size. The time-evolution equations 3.6 and 3.7 then become,

$$\frac{\partial \rho}{\partial t'} = \frac{\partial^2 \rho}{\partial x^2} + 2\beta\rho(1 - \rho) \frac{\partial m}{\partial x} + \beta(2m - 1)(1 - 2\rho) \frac{\partial \rho}{\partial x} \quad (3.10)$$

$$\frac{\partial m}{\partial t'} = \frac{\partial^2 m}{\partial x^2} - 2\beta \frac{\partial}{\partial x} [\rho m(1 - m)] + 2\beta\lambda \frac{\partial}{\partial x} [m(1 - m)] \quad (3.11)$$

where $t' = t/N^2$ is the rescaled time.

In the stationary state, the time-derivatives on the left hand sides of the Eqs. 3.10 and 3.11 vanish. Recalling that the overall density of upslope bonds in the system is 1/2 and

periodic boundary condition requires the density of H particles to be equal to λ , we linearize $m(x) = 1/2 + \delta m(x)$ and $\rho(x) = \lambda + \delta\rho(x)$, in the stationary state to obtain,

$$\frac{\partial^2}{\delta x^2} \delta m - \frac{\beta}{2} \frac{\partial}{\partial x} \delta \rho = 0 \quad (3.12)$$

$$\frac{\partial^2}{\delta x^2} \delta \rho + 2\beta\lambda(1 - \lambda) \frac{\partial}{\partial x} \delta m = 0 \quad (3.13)$$

Making the Fourier expansions,

$$\delta m(x) = \sum_n a_n \exp(2\pi i n x / N) \quad (3.14)$$

$$\delta \rho(x) = \sum_n b_n \exp(2\pi i n x / N)$$

we find from Eqs. 3.12 and 3.13 that,

$$i2\pi n a_n = \frac{\beta}{2} b_n \quad (3.15)$$

and,

$$i2\pi n b_n = -2\beta\lambda(1 - \lambda) a_n. \quad (3.16)$$

To obtain non-zero solutions for a_n and b_n we must have,

$$\beta = \frac{2\pi n}{\sqrt{\lambda(1 - \lambda)}} \quad (3.17)$$

which has the minimum value $\beta_c = \frac{2\pi}{\sqrt{\lambda(1 - \lambda)}}$ for $n = 1$. For any β smaller than this value no non-zero a_n and b_n can be found and $\rho(x)$ and $m(x)$ only allow uniform solutions, corresponding to a disordered state (a_0 and b_0 non-zero). Thus β_c gives the critical point for the order-disorder transition in the system.

To verify this in simulations, we define the order parameters s_ρ and s_m

$$s_\rho = \frac{1}{N} \sum_{i=1}^N n_i n_{i+1} - \lambda^2 \quad (3.18)$$

$$s_m = \frac{1}{4N} \sum_{i=1}^N (1 + \tau_{i+1/2})(1 + \tau_{i+3/2}) - \frac{1}{4} \quad (3.19)$$

which characterize the order in the particles and the landscape, respectively. Our simulations show that for small values of β , the average values $\langle s_\rho \rangle$ and $\langle s_m \rangle$ are zero, indicating a

disordered phase. As β increases, the system goes into an ordered phase with finite values of $\langle s_\rho \rangle$ and $\langle s_m \rangle$. To calculate the critical β , at which the transition takes place, we plot the second order Binder cumulant,

$$f_\alpha = 1 - \langle s_\alpha^2 \rangle / \langle s_\alpha \rangle^2 \quad (3.20)$$

as a function of β (see Fig. 3.4), where $\alpha = \rho, m$ for different system sizes. Since here, one does not need to distinguish between the positive and negative values of the order parameter s_α , the quantity defined in Eq. 3.20 serves the purpose of the standard binder cumulant defined by,

$$b_\alpha = 1 - \langle s_\alpha^4 \rangle / 3 \langle s_\alpha^2 \rangle^2 \quad (3.21)$$

At the critical point β_c , the value of f_α must be universal, which means the curves for different N values must coincide at β_c . In Fig. 3.4 we present data for $\lambda = 1/5$ for which we expect $\beta_c = 5\pi \simeq 15.708$. From our simulation data we find $\beta_c \simeq 15.65$ and 15.76 for $\alpha = \rho$ and $\alpha = m$, respectively. These values are close to the theoretical prediction.

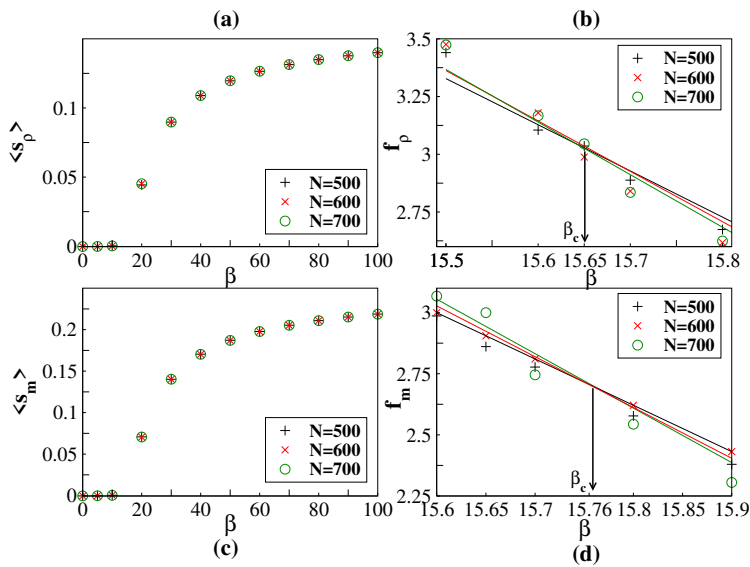


Figure 3.4: Temperature variation of s_ρ and s_m for three different values of N [plots (a) and (c)]. (b) and (d) show the cumulants f_ρ and f_m for three N values. We have used $\lambda = 0.2$ here. We obtain the best linear fits to the data points for each value of N . From the point of intersection of the straight lines, β_c is estimated to be 15.65 ± 0.001 for f_ρ and 15.76 ± 0.005 for f_m which is close to theoretical prediction 5π . The data shown here have been averaged over at least 10^8 histories.

3.4 IPS (INFINITESIMAL CURRENT WITH PHASE SEPARATION) PHASE [$b' = 0$]

The IPS phase is obtained along the dashed lines of the phase diagram in Fig. 3.1, where b' vanishes, alternatively, $R' = 1$ and from Eq. 3.4 it follows that $\lambda = 0$. In this case, the local fluctuations in the surface occupied by L particles are of the symmetric Edwards-Wilkinson type [37], while the H particles continue to push the surface down. In our derivation of detailed balance condition in section 3.3.1 above, we have shown that $\lambda = \rho$ has to be satisfied for a periodic system. In the IPS phase this condition gets violated for all finite ρ . As a result, the detailed balance breaks down. We use the Kolmogorov loop condition [52] to explicitly show the lack of detailed balance, as illustrated below.

3.4.1 Breakdown of detailed balance in the IPS phase

The Kolmogorov loop condition [52] states that the necessary and sufficient condition for a system to satisfy detailed balance is that for every closed loop in configuration space, $Q = \frac{W(1 \rightarrow 2)W(2 \rightarrow 3) \dots W(K \rightarrow 1)}{W(2 \rightarrow 1)W(3 \rightarrow 2) \dots W(1 \rightarrow K)} = 1$ where $W(i \rightarrow j)$ denotes the transition rate from configuration C_i to C_j . To show that detailed balance is violated, it suffices to find a single loop in configuration space for which the above condition is not satisfied. In Fig. 3.5 we explicitly show this for a set of local configurations. Since each configuration is specified by the particle occupancy at the lattice sites, and slope of the lattice bonds, the first and the last configurations in the sequence presented in Fig. 3.5 are identical and hence this sequence forms a closed loop in the configuration space. According to our dynamical rules, $W(4 \rightarrow 5) = D + a$ and $W(5 \rightarrow 4) = D - a$. All other rates $W(i \rightarrow i + 1)$ are same as the reverse rate $W(i + 1 \rightarrow i)$, since in the IPS phase $b' = 0$. The ratio Q then becomes $Q = \frac{D+a}{D-a} \neq 1$, which proves violation of detailed balance.

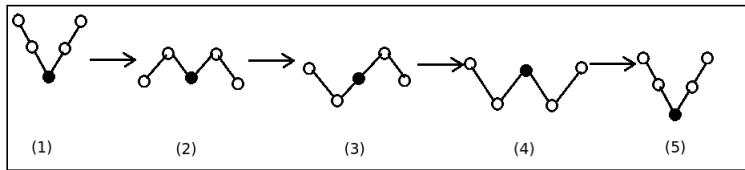


Figure 3.5: Breakdown of Kolmogorov loop condition in the IPS phase. Starting from the first configuration, the system passes through a sequence of configurations and comes back to the starting configuration again, but the ratio $Q = \frac{W(1 \rightarrow 2)W(2 \rightarrow 3)W(3 \rightarrow 4)W(4 \rightarrow 5)}{W(2 \rightarrow 1)W(3 \rightarrow 2)W(4 \rightarrow 3)W(5 \rightarrow 4)} \neq 1$. This shows that the system does not obey detailed balance.

3.4.2 A single H particle in the IPS phase: height profile of the landscape

In order to understand the nature of the IPS phase, let us first consider the case of a single H particle with $(N - 1)$ lattice sites occupied by L particles. According to the dynamical rules, the local height fluctuations at these $(N - 1)$ sites are symmetric, of Edwards-Wilkinson type [37], and only at the site containing the H particle the height fluctuation is asymmetric, of Kardar-Parisi-Zhang type [36]. Obviously, this asymmetry drives the system out of equilibrium and there is a non-zero current in steady state, which gives rise to a downward velocity of the surface. Since the local fluctuations are symmetric almost everywhere in the system, to support this downward drift, a gradient is generated in the density of upslope and downslope bonds of the surface. We calculate this gradient within mean-field theory below.

Let us consider a site at a distance k from the position of the single H particle in the system, and let $S^+(k, N)$ be the probability to find an upslope bond between this site and its right neighbor. Similarly, let $S^+(k - 1, N)$ be the probability to find an upslope bond between the site and its left neighbor. Within mean-field theory, the site under consideration will be at the top of a local hill with probability $S^+(k - 1, N)[1 - S^+(k, N)]$. From this local configuration, the height of the site can decrease with rate E , when the local hill flips to a valley (see Eq. 2.2). Likewise, the probability that the site is at the bottom of a local valley is given by $[1 - S^+(k - 1, N)]S^+(k, N)$ and from here its height can increase with the same rate E . The downward velocity of the surface at this position is then $E[S^+(k - 1, N)\{1 - S^+(k, N)\} - \{1 - S^+(k - 1, N)\}S^+(k, N)]$.

In the steady state, this velocity must be the same everywhere in the system and hence independent of k . In other words, $[S^+(k - 1, N) - S^+(k, N)] = C$, which is a constant. Moreover, for an untilted surface, $\sum_k S^+(k, N) = N/2$. These two relations together imply that $S^+(k, N)$ decreases linearly with k with a gradient $\sim 1/N$, for large N . We verify this from the simulation data in Fig. 3.6.

3.4.3 Clustering of H particles in the IPS phase in the adiabatic limit

In this section, we perform a simple calculation to explain the rationale behind the clustering tendency of the H in the IPS phase.

First let us consider a large system in the continuum limit with a finite M number of H particles in it. Let x_1, x_2, \dots, x_M be the positions of these particles. Apart from these positions,

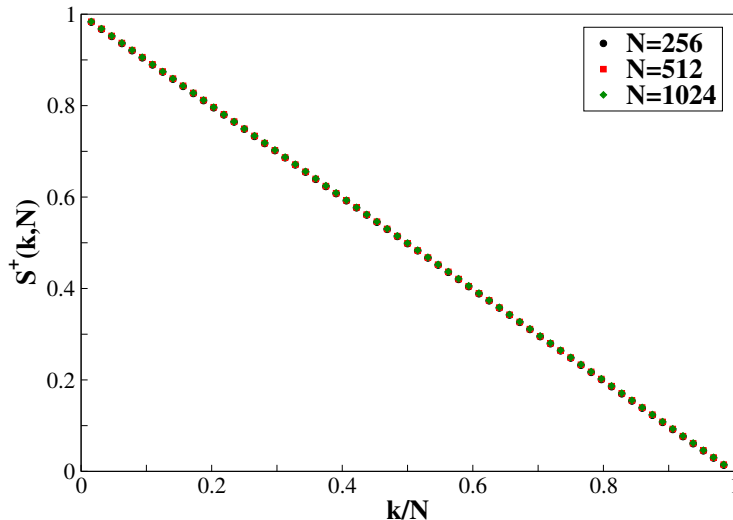


Figure 3.6: We measure the density of upslopes $S^+(k, N)$ as a function of the scaled distance k/N , where k is the distance measured from the position of the single H particle in a system of size N . The profile decreases linearly with a gradient $\sim 1/N$ as predicted by our mean field analysis. The data shown here have been averaged over at least 10^4 initial histories.

the local height fluctuations of the surface are symmetric and of Edwards-Wilkinson type, while at the positions x_i 's the height fluctuations are biased. This is captured by the equation,

$$\partial_t h(x, t) = D \partial_x^2 h(x, t) + \eta(x, t) + j_0 \sum_{n=1}^M \delta(x - x_n) \quad (3.22)$$

where j_0 represents the bias imparted by the H particles, $\eta(x, t)$ is the white noise and D the surface diffusivity. To find the mean profile $\bar{h}(x, t)$, we average over the noise and obtain,

$$\partial_t \bar{h}(x, t) = D \partial_x^2 \bar{h}(x, t) + j_0 \sum_{n=1}^M \delta(x - x_n). \quad (3.23)$$

Let us first consider $M = 1$, when there is a single H particle present in the system at the position x_1 . To solve the above equation, we make an adiabatic assumption based on the separation of time-scales. Suppose the H particle is very heavy such that it hardly ever moves during the time the height fluctuations of the surface are taking place. In this limit, we can treat x_1 as the position of a quenched defect and without any loss of generality put $x_1 = 0$. The above equation can then be solved using Green's function method [56]. Starting from a flat height profile at $t = 0$, we can write the height profile at time t as,

$$\bar{h}(x, t) = j_0 \int_0^t \frac{1}{(4\pi D)^{1/2}} \frac{e^{-x^2/4Ds}}{s^{1/2}} ds = \frac{j_0}{4D\pi^{1/2}} x \Gamma \left(-\frac{1}{2}, \frac{x^2}{4Dt} \right) \quad (3.24)$$

where Γ denotes the incomplete Gamma function. For large t , we have $x^2/4Dt \ll 1$ and,

$$\bar{h}(x, t) \simeq \frac{j_0}{\sqrt{\pi}} \left[2\sqrt{\frac{t}{D}} - \frac{\sqrt{\pi}}{2D} \frac{|x|}{D} \right]. \quad (3.25)$$

Similarly, for $M = 2$, when there are two quenched defects in the system, at x_1 and x_2 , each will generate a height profile around its position. As the system is linear, the resulting height profile is given by,

$$\bar{h}(x, t) \simeq \frac{j_0}{\sqrt{\pi}} \left[2\sqrt{\frac{t}{D}} - \frac{\sqrt{\pi}}{2D} (|x - x_1| + |x - x_2|) \right]. \quad (3.26)$$

If each particle has mass m , the mean gravitational energy E_g associated with the system is,

$$E_g = -\frac{mgj_0}{\sqrt{\pi}} \left[4\sqrt{\frac{t}{D}} - \frac{\sqrt{\pi}}{D} |x_1 - x_2| \right] \quad (3.27)$$

which is minimum when $|x_1 - x_2|$ is minimum. This explains why the two H particles tend to cluster together. This argument can be extended immediately to arbitrary M , providing insight into the strong clustering tendency of H particles in the IPS phase.

Indeed for a finite density of H particles in the lattice model, where the particles have a finite size, we find a complete phase separation of H and L particles. The upslope and downslope surface bonds lying under the H particle cluster, phase separate to form a deep valley. The domains of all-upslope and all-downslope bonds extend up till the edges of the H particle cluster. Beyond that, in the L -phase, the landscape has a parabolic shape with a mean curvature $1/N$. The fluctuation properties of the surface beneath the L -cluster can be explained by mapping this part of the system to an open-chain symmetric exclusion process [50], with the upslope (downslope) bonds being identified with particles (holes); the pure domains of these bonds in the H -phase act as reservoirs for the respective species. We elaborate more on this issue in chapter 4 where we discuss the steady state dynamics.

3.4.4 Coarsening in the IPS phase

Interestingly, in the IPS phases there is an enormous reduction in the relaxation time, as compared to that in the SPS phase. For the IPS phase ($b' = 0$), the landscape is organized differently, and this leads to fast relaxation, with times growing as N^z . Starting from an initial disordered landscape and randomly distributed particles, the landscape forms small domains of V-shaped landscape holding small H -clusters. The landscape beneath the intervening L clusters shows symmetric fluctuations which merge in diffusive time to give rise

to compact domains of upslopes and downslopes holding a single H -cluster. We show a schematic diagram depicting the domain merging process in Fig. 3.7.

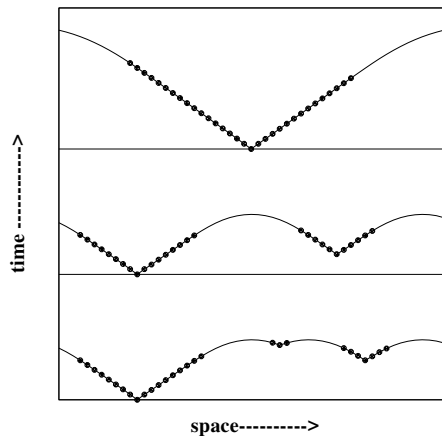


Figure 3.7: Coarsening mechanism in one dimension for $b' \leq 0$

Figure 3.8 shows the scaling collapse of the equal time density correlation function for H particles when separations are scaled by the coarsening length scale $\mathcal{L}(t)$, which is found to grow as $t^{1/z}$. In IPS phase we find $z = 2$.

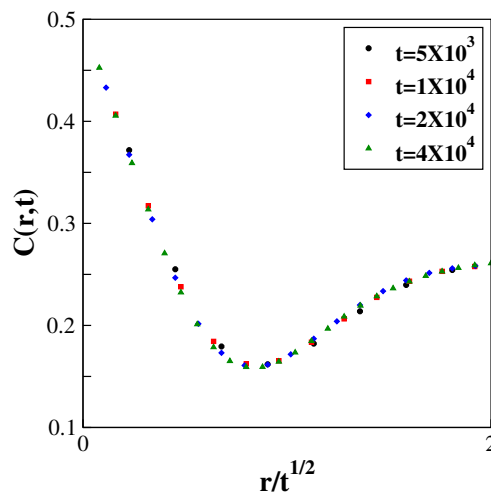


Figure 3.8: The equal time density correlation for the particles $C(r, t)$ shows a collapse when r is scaled by $\mathcal{L}(t) \sim t^{1/z}$ for $b = 0.5, b' = 0$. Here we find $z \simeq 2$.

3.4.5 Rescaled temperature and phase transitions in the IPS phase

Compact domains in the IPS phase are observed as long as the H particles act as the heavier species, *i.e.*, as long as the ratio $q = (D - a)/(D + a) < 1$. As q approaches unity, the domains do not remain as compact and their boundaries become wider. However, this width remains

finite and in the thermodynamic limit, sufficiently far away from these boundaries a pure phase is always retrieved. For a finite system size N , there exists a critical value q_c , when the width of the domain boundaries becomes of the order of the system size and the system becomes disordered.

A similar mean-field calculation as shown in section 3.3.3 can be performed for the IPS phase as well. Following equations 3.6 and 3.7, one may write the time-evolution equations for variables $\rho_i, m_{i+1/2}$ in the IPS phase. The equations read,

$$\begin{aligned} \frac{d\rho_i}{dt} = & \rho_{i-1}(1 - m_{i-1/2})(1 - \rho_i) - \rho_i(1 - m_{i+1/2})(1 - \rho_{i+1}) + q\rho_{i-1}m_{i-1/2}(1 - \rho_i) \\ & - q\rho_i m_{i+1/2}(1 - \rho_{i+1}) \end{aligned} \quad (3.28)$$

$$\begin{aligned} \frac{dm_{i+1/2}}{dt} = & m_{i-1/2}\rho_i(1 - m_{i+1/2}) + q^2(1 - m_{i+1/2})\rho_{i+1}m_{i+3/2} \\ & + (1 - m_{i+1/2})(1 - \rho_{i+1})m_{i+3/2} + m_{i-1/2}(1 - \rho_i)(1 - m_{i+1/2}) \\ & - m_{i+1/2}\rho_{i+1}(1 - m_{i+3/2}) - q^2(1 - m_{i-1/2})\rho_i m_{i+1/2} \\ & - (1 - m_{i-1/2})(1 - \rho_i)m_{i+1/2} - m_{i+1/2}(1 - \rho_{i+1})(1 - m_{i+3/2}) \end{aligned} \quad (3.29)$$

Taking the continuum limit and explicitly rescaling β by the system size, the equations 3.28 and 3.29 are given by,

$$\frac{\partial \rho}{\partial t'} = \frac{\partial^2 \rho}{\partial x^2} + 2\beta\rho(1 - \rho)\frac{\partial m}{\partial x} + \beta(2m - 1)(1 - 2\rho)\frac{\partial \rho}{\partial x} \quad (3.30)$$

$$\frac{\partial m}{\partial t'} = \frac{\partial^2 m}{\partial x^2} - 2\beta\frac{\partial}{\partial x}[\rho m(1 - m)] \quad (3.31)$$

where $t' = t/N^2$ is the rescaled time. Linearising these equations by expanding the densities about their global averages and making Fourier expansions 3.14, for the IPS phase one obtains,

$$i2\pi n a_n = \frac{\beta}{2} b_n \quad (3.32)$$

and

$$i2\pi n b_n = -\frac{\beta}{2} a_n. \quad (3.33)$$

This yields $\beta_c = 4\pi$, which we have verified by simulation (see Fig. 3.9).

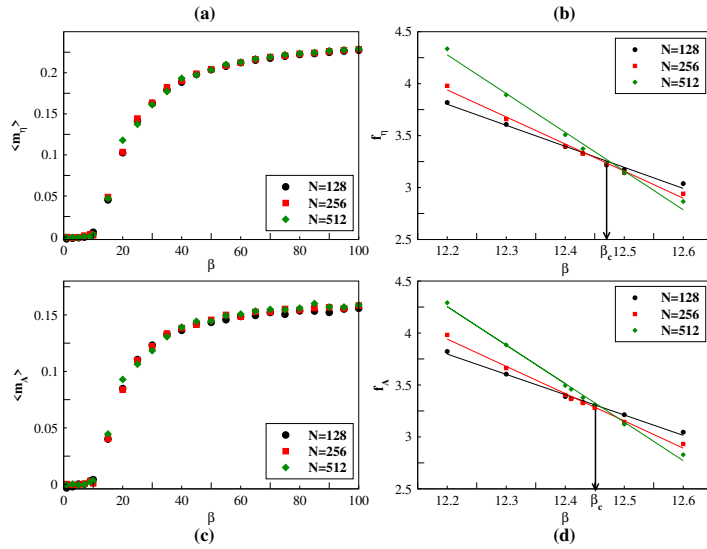


Figure 3.9: Temperature variation of s_ρ and s_m for three different values of N [plots (a) and (c)]. (b) and (d) show the cumulants f_ρ and f_m for three N values. We have used $\lambda = 0$ here. The best linear fits to the data points have been obtained for each value of N . From the point of intersection of the straight lines, β_c is estimated to be 12.47 ± 0.001 for f_ρ and 12.45 ± 0.001 for f_m which is close to theoretical prediction 4π . The data shown here have been averaged over at least 10^8 histories.

3.4.6 Static correlations in the IPS phase

In Fig. 3.10, we present our results on the static correlation functions for the particles and for the surface bonds when the system is in the IPS phase. Here we have considered equal number of H and L particles and all distances have been measured from the centre of mass of the H -cluster. $\rho(r, N)$ and $S^+(r, N)$ denote, respectively, the density of H particles and the probability to find an upslope bond at a distance r from the centre of mass. Our data show that the surface beneath the pure domain of H -cluster has the shape of a deep valley consisting of pure phases of upslope and downslope bonds. By contrast, the surface occupied by the L -cluster in this case behaves like an open-chain symmetric exclusion process connected to the two reservoirs of upslope and downslope tilts at the two ends. Thus the tilt density varies linearly in this region with a gradient $\sim 1/N$ [20], leading to a tilt current and an infinitesimal downward velocity $\sim 1/N$ of the entire landscape (Fig. 3.10).

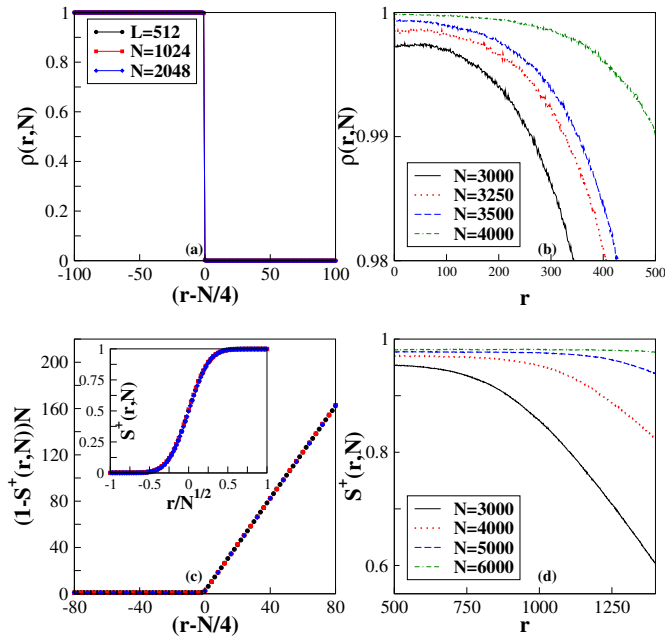


Figure 3.10: Static correlation functions in IPS phase. (a): Density of H particles $\rho(r, N)$ at $q = 0$. The density changes sharply from 1 to 0 indicating pure phases of H and L particles. (b): For $q = (D - a)/(D + a) = 0.99$ (see Eq. 3.4 in 3.3.1), H particle density approaches 1 as N is increased. This confirms the existence of a pure phase in the thermodynamic limit for all $q < 1$. (c) Main plot: For $r \gg \sqrt{N}$ a scaling collapse is obtained for different system sizes when $[1 - S^+(r, N)]N$ is plotted against $(r - N/4)$. Inset shows that as r changes sign, $S^+(r, N)$ shows a transition from 0 to 1 across the domain boundary, which is at the deepest point of the valley. Due to diffusive motion of the domain boundary, $S^+(r, N)$ is a scaling function of r/\sqrt{N} in this region. In main plot and inset we show data for $N = 512$ (black circles), 1024 (red squares) and 2048 (blue diamonds). (d): For $q = 0.99$ and $0 \ll r \ll N/4$ $S^+(r, N) \rightarrow 1$ as N is increased. These data have been averaged over at least 3×10^5 steady state configurations.

3.5 FPS (FINITE CURRENT WITH PHASE SEPARATION) PHASE $[-b < b' < 0]$

The FPS phase can be observed in the dotted region of the phase diagram (Fig. 3.1), where $1 > R > R'$, *i.e.*, when both the particle species push the landscape down, but the H particles do so at a larger rate than the L 's. In this phase, the H and L particles again show complete phase separation and although the landscape forms a single macroscopic valley, neither of the two arms of the valley comprises a compact domain of $/$ or \backslash bonds, unlike in the SPS or IPS phases. In this section we present numerical and analytical results on the static characterisation of this phase.

3.5.1 Coarsening in the FPS phase

We find a fast coarsening to the FPS phase similar to the IPS phase with domain sizes growing as $t^{1/z}$ with $z = 2$. In the FPS phase, during domain merging, the landscapes beneath the intervening L cluster get pushed downward since $b' < 0$. However, the FPS phase ($-b < b' < 0$) shows $z \simeq 2$ in one dimension for very large N and t while for smaller values of these variables, we find $z \simeq 2.5$. We define r_0 as $C(r_0, t) = 0$ and the dynamical exponent z can be estimated from the variation of r_0 with t , using the scaling relation $r_0 \sim t^{1/z}$. Our data shows finite size effects in the value of the dynamical exponent at small times $t < 10^5$ (see Fig. 3.11).

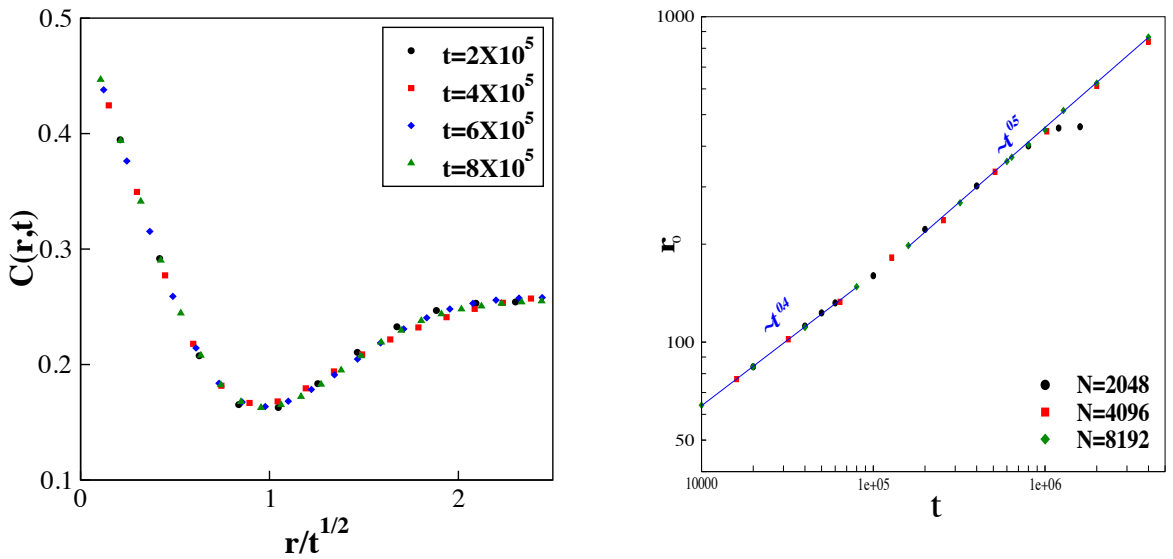


Figure 3.11: The equal time density correlation for the particles $C(r, t)$ shows a collapse when r is scaled by $\mathcal{L}(t) \sim t^{1/z}$ for $b = 0.3, b' = -0.2$ in the left panel. Here we find $z \simeq 2$. The right panel shows plot of r_0 vs time during the coarsening phase for $b = 0.3, b' = -0.2$. For large N and t , we obtain $r_0 \sim t^{0.5}$. For $t \lesssim 10^5$, we observe a crossover region where $r_0 \sim t^{0.4}$. We have used $\rho_0 = 1/2$ here.

3.5.2 Static correlations in H -region of the landscape in FPS phase

A typical configuration in the FPS phase is shown in Fig. 2.2(c). Here, a large valley forms in the landscape that holds the H -cluster, but unlike IPS phase, this valley consists of domains of upslope and downslope bonds which are not compact. Let m be the density of downslope (upslope) bonds in the upslope-(downslope)-rich domain. For a perfectly ordered domain, m takes the value 0 while in the disordered case $m = 1/2$, while $0 < m < 1/2$ indicates a phase separation with the minority species interspersed with the majority species. It is possible to analytically calculate the value of m in this phase.

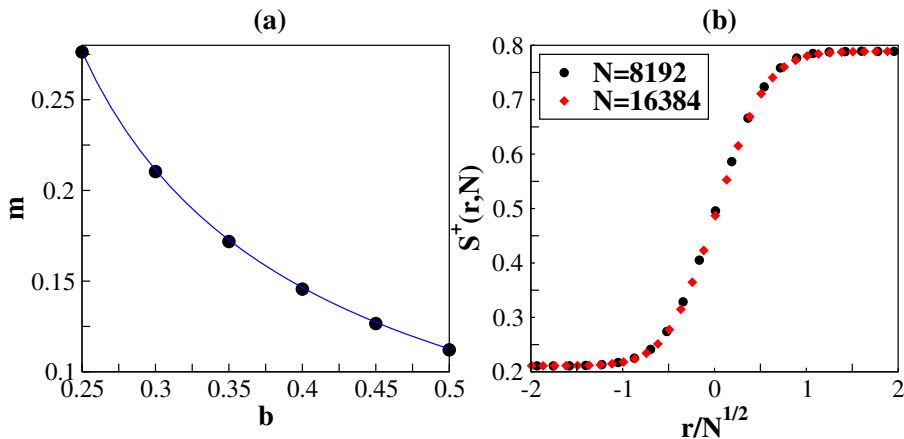


Figure 3.12: (a): Away from the valley bottom $S^+(r, N)$ saturates at a value m , which depends on b and b' . For $b' = -0.3$, we vary b and plot m , which matches well with the mean-field result. Discrete points are from simulation data and the continuous line shows mean-field solution of Eq. 3.34. We have used $N = 1024$ here. (b): $S^+(r, N)$ changes from the value $(1 - m)$ to m across the domain boundary of width \sqrt{N} .

Within mean-field theory, it follows from the dynamical rules (Eq. 2.2) that the average velocity of the surface in H -region is $2bm(1 - m)$. In the steady state, this must be equal to the velocity in the L -region. Now, in the L -region the surface is disordered, and this part of the surface can be mapped onto an open-chain asymmetric exclusion process in the maximal current phase (see Fig. 3.13) [47]. The velocity of the surface in this region is then $b'/2$. Matching the two velocities in the H and L regions, we find the following quadratic equation

$$m^2 - m - \frac{b'}{4b} = 0 \quad (3.34)$$

which can be solved for m for a given b and b' . To verify this, we measure the density of upslope bonds in the H -region, across the valley minimum, this density shows a transition from the value m to $(1 - m)$. We compare the m value measured in simulation, with that obtained from solving Eq. 3.34 and find good agreement (see Fig. 3.12a). The width of the boundary between the upslope-rich and downslope-rich domains scales as \sqrt{N} , as shown in Fig. 3.12b. We discuss in [49] that this width is related to the motion of the valley bottom within a region of size $\sim \sqrt{N}$ around the center of mass of H -cluster. We would like to mention here that the system shows rather strong finite size effects and we had to go to relatively large N ($\sim 10^4$) in order to find the saturation value of S^+ away from the domain boundary.

As mentioned above, the behavior of the landscape in the L -region is like that of an open system. The ordered domains of the upslope and downslope bonds in the H -region act as the reservoirs which are connected to the two ends of the L region. Mapping the upslope (downs-

lope) bonds to particles (holes), we find that the surface in the L -region can be mapped onto an open-chain asymmetric exclusion process, which was introduced in [50] and different phases were obtained on changing the reservoir couplings. In our system, the properties of the landscape in the L -region are same as those observed for a maximal current phase in the open system. The landscape is disordered in the L region, with $S^+(r, N) = 1/2$. From the $H - L$ domain boundary, $S^+(r, N)$ decays algebraically to this disordered value with an exponent $1/2$, as shown in Fig. 3.13.

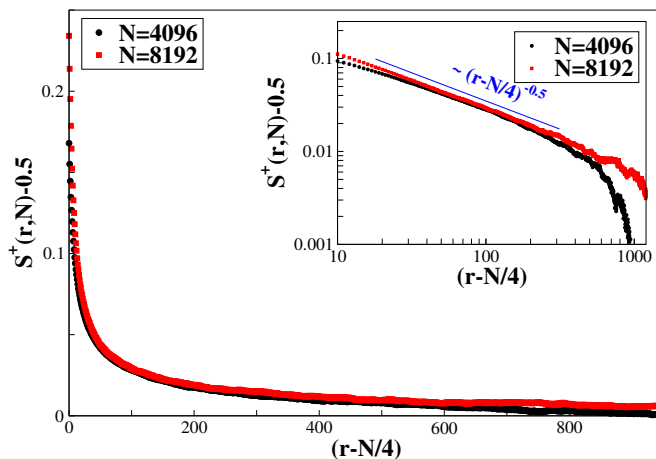


Figure 3.13: We plot $S^+(r, N)$ after subtracting the disordered phase value $1/2$ against $(r - N/4)$ for two different system sizes with $b = 0.3, b' = -0.2$. The decay to a disordered phase occurs algebraically with an exponent $1/2$ (inset). The data shown here have been averaged over at least 10^6 initial configurations.

3.5.3 FDPO (Fluctuation-dominated phase ordering) phase [$b = -b'$]

The FDPO phase can be observed along the $R = R'$ line in the phase diagram in Fig. 3.1. In this case, the H and L particles push the surface down at exactly the same rate. The transition rates between the local hills and valleys of the surface are therefore identical at every lattice site. In other words, the surface behaves just like an ordinary Kardar-Parisi-Zhang surface with a downward bias. With periodic boundary conditions, the steady state measure of Kardar-Parisi-Zhang surface satisfies product measure [57], *i.e.*, the upslope and downslope bonds of the landscape are independently and randomly distributed and the landscape is disordered. This remains true even when both b and b' are zero, and the landscape shows Edwards-Wilkinson type equilibrium fluctuations, since the same product measure holds for a periodic Edwards-Wilkinson surface in one dimension.

Note that in this phase, the coupling between the landscape and the particles is one-way, *i.e.*, while the particles continue being affected by the local height gradient of the landscape, with moves shown in Figs. 2.1 and 2.2, the local dynamics of the landscape does not depend

on whether there is an H particle or L particle on it. This limit is tantamount to passive scalar advection and was studied in detail in [27, 28]. In this phase, while the landscape remains completely disordered, the H and L particles show clustering accompanied by macroscopic fluctuations, as shown in Fig. 2.2d. Owing to strong fluctuations present in the system, these clusters undergo constant reorganization, even in the thermodynamic limit. We do not focus on this phase in our thesis.

3.6 CONCLUSION

In this chapter, we have studied the static properties of the different phases present in a coupled non-equilibrium system and explicitly demonstrated how the coupling affects the qualitative nature of the ordering. In our model described in Chapter 2, a lighter and a heavier particle species move on a potential energy landscape. The particles try to lower the potential energy, and in occupying valleys in the landscape, the heavier species always gets preference over the lighter one. Crucially, the particles also affect the landscape locally, so as to lower the energy further. Depending on how each species interacts with the landscape, we find different phases in the system. In the case when the heavier species tends to push the landscape downward, and the lighter species tends to push it upward, the system shows SPS phase, where the ordering is strongest. When the heavier species pushes the landscape downward, but the lighter one does not push the surface in either direction, rather allows equilibrium local fluctuations of the landscape, we obtain an IPS phase. Finally, FPS phase is obtained, when the lighter species also pushes the landscape downward, but at a smaller rate than the heavier ones. In the limit when both the species affect the landscape in a similar way, either by pushing in a direction with the same rate, or by allowing local equilibrium fluctuations, we obtain FDPO. And in all other cases, we get a disordered phase, with no long-ranged correlations. The schematic configurations in Fig. 2.2 (Chapter 2) show that the main difference between the SPS, IPS and FPS phases lies in the shape of the landscape. In all these phases, the H and L particles completely phase separate from each other and form one single H and L cluster. But due to the different nature of effects produced by these particles on the landscape, one obtains different phases, where the landscape may be completely ordered or may show coexistence of ordered and disordered segments.

DYNAMIC PROPERTIES OF ORDERED PHASES IN THE LH MODEL

4.1 INTRODUCTION

In this chapter we study the dynamical properties of the ordered phases obtained in a coupled model system of two species of particles advected by a stochastically evolving landscape. The local dynamics of the landscape also gets affected by the particles. By tuning the parameters that govern the differential action of the particles on the landscape, one obtains a phase diagram that reveals presence of several ordered phases and a disordered phase (see Fig. 2.1). Previously, in Chapter 3, we have had an elaborate discussion on the static properties of each of the ordered phases. This chapter intends to focus on the dynamics of the ordered phases. We show that in all the three ordered phases (SPS, IPS, and FPS), there are macroscopic particle clusters that move over an ergodic time-scale growing exponentially with system size. However, while in the SPS phase the landscape shows slow dynamics over an ergodic time-scale, the IPS and FPS phases are associated with fast, algebraic dynamics in the landscape. We present a scaling ansatz that describes several dynamical correlation functions of the landscape measured in steady state. Results discussed in this chapter have been published in [49].

4.2 SLOW DYNAMICS IN THE SPS (STRONG PHASE SEPARATION) PHASE

$b, b' > 0$ corresponds to the SPS phase where there is a complete phase separation between the H and L particles and the upslope and downslope bonds in the landscape as well (see figures 2.1 and 2.2). This is the phase studied in the Lahiri-Ramaswamy model of sedimenting colloidal crystals [24, 25]. The pure domains of up and down-slope bonds form into a deep ∇ -shaped valley holding the H -cluster. An average height profile of the landscape in the SPS phase is shown in Fig. 4.1. Coarsening towards such a phase is a logarithmically slow process as has been explained in Sec. 3.3.2. For any $b, b' > 0$, the relaxation involves an Arrhenius process across a large barrier, and the system gets stuck in metastable states [25]. As a result, the relaxation time grows exponentially with the system size in an SPS phase.

Such diverging timescales allow for little dynamics in steady state and both particles and the landscape show slow dynamics over an ergodic time-scale.

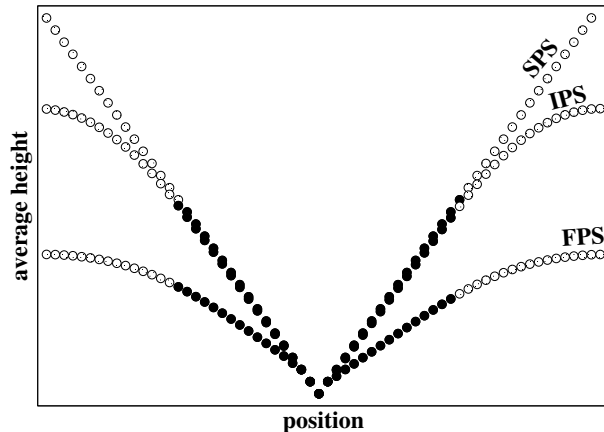


Figure 4.1: Schematic description of various ordered phases. We show the average height profile of the landscape, H (L) particles are shown by solid (empty) circles. In the SPS phase, due to complete phase separation between upslope and downslope bonds, average height grows linearly from the deepest point, with a slope 1. In the IPS phase, the height profile remains similar to SPS till the edge of the H cluster and then it gradually flattens out. In the FPS phase, owing to partial phase separation between upslope and downslope bonds in the H -region, the height grows linearly with a slope smaller than unity, before flattening out in the L -region.

4.3 DYNAMICS IN THE IPS (INFINITESIMAL CURRENT WITH PHASE SEPARATION) PHASE

Contrary to the SPS phase, which shows virtually no dynamics in the steady state, the IPS and FPS phases show rich dynamics. The organisation in the landscape vary widely in nature from one phase to another as demonstrated in Chapters 2 and 3. The landscape in the IPS phase is characterised by a \vee -shaped bottom holding the H -cluster which flattens and assumes a parabolic shape beneath the L -particle cluster (see Fig. 4.1). The different sorts of organisation in the landscape give rise to qualitatively different time-scales in the steady state dynamics in the ordered phases. For instance, although the centre of mass of the H cluster remains stationary for a long time, the landscape immediately below it undulates in time, leading to three distinct temporal regimes in steady state. These are captured by monitoring the mean-squared displacement σ_0^2 of the deepest point of the valley. We present our data for mean-squared displacement of the deepest valley in the IPS phase in Figure 4.2.

At small times $t \ll N^2$, we find σ_0^2 grows diffusively with a diffusion constant $D_1 \sim 1/N$. But after times $\sim N^2$, a plateau for σ_0^2 is reached at a value $\sim N$. From a simple consideration of the total (gravitational) energy of the H particles, it is easy to show that when the deepest point coincides with the centre of mass of the H cluster, the energy is

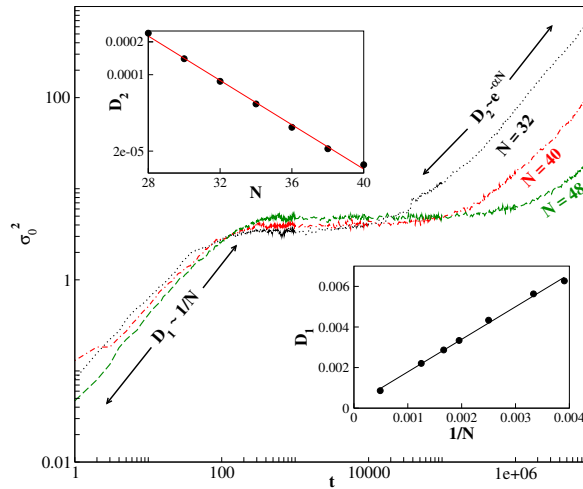


Figure 4.2: Occurrence of three regimes in the steady state dynamics of the deepest point of the valley. Main plot: Mean squared displacement of the deepest point of the valley as a function of time. The displacement shows an initial diffusive growth, followed by a plateau, and finally another diffusive regime at large time. Bottom Inset: Small time diffusivity $D_1 \sim 1/N$. Top Inset: For large time, the diffusivity $D_2 \sim e^{-\alpha N}$, with $\alpha \simeq 0.26$. These data correspond to $b' = 0$, $b = E$, $a = D$ and have been averaged over 5000 steady state configurations.

minimum. Any displacement from this position gives rise to a restoring force that scales linearly with the displacement. We will shortly demonstrate that the motion of the deepest point in the IPS phase is described by an Ornstein-Uhlenbeck process [58]; consequently, the deepest point diffuses within a region of size \sqrt{N} around the H cluster centre of mass. Finally, at very large t , the H cluster itself moves diffusively around the system and the valley moves along with it. The mean-squared displacement of the deepest point in this regime has a diffusion coefficient $D_2 \sim e^{-\alpha N}$. We explain the mechanisms for the short and large time valley displacements using simple analytical arguments and schematic diagrams in the following sections.

4.3.1 Mechanism for small time behaviour of valley dynamics in IPS phase

With the help of a schematic diagram in the IPS phase (see Fig. 4.3), we show the positions of the deepest valley (V), centre of mass of the H -cluster (C), and the right (i_R) and left (i_L) edges of the H -cluster and the dynamical variables associated with their fluctuations. The deepest point of the valley (V) lies at the boundary between two pure domains of upslope and downslope surface bonds and these pure domains extend upto the edges i_L and i_R of the H particle cluster.

The $1/N$ scaling of the short time diffusivity can be explained using a simple argument. At short times, the mechanism for valley dynamics involves the propagation of a downslope

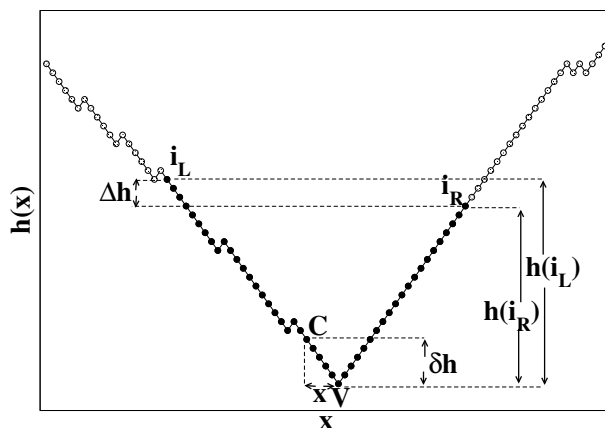


Figure 4.3: The deepest point V of the valley moves a distance x from the centre of mass C of the H cluster. This causes a height asymmetry Δh .

(upslope) bond through a pure domain of upslope (downslope) bonds. For example, if a downslope (upslope) bond reaches the upper edge of the H particle cluster, then it zips ballistically through the domain of pure upslopes (downslopes) beneath the cluster and causes V to shift by one unit towards the right (left). The time-scale associated with this process is proportional to N . Further, to estimate the time-scale for formation of a local hill at the edge of the H cluster, we show with the aid of a simple mean-field calculation in Sec. 4.3.1.1, that the average distance of the nearest downslope bond from the $H - L$ domain boundary scales as \sqrt{N} . This downslope bond reaches the H -cluster boundary diffusively at times $\sim N$. Thus the time-scale of the two relevant processes — formation of a local hill at the edge of the H -cluster, and transport of that hill towards the bottom of the valley — are both of order N . Since the processes occur with equal weight on the left and right arms of the valley, the motion of V is diffusive, with diffusivity $\sim 1/N$. Finally, in the long time limit, the centre of mass of the H -cluster undergoes a shift by one unit thus giving rise to an infinitesimally small diffusivity scaling as $\exp(-\alpha N)$. We pictorially demonstrate the mechanisms for the short and large time behaviour of the valley diffusion in Fig. 4.4.

4.3.1.1 Average distance of the nearest downslope bond from the $H - L$ domain boundary in IPS phase

In the part of the surface occupied by the L particles, the density profile of the surface bonds shows a linear gradient (see Fig. 3.10) [47]. We show that within the mean-field approximation, the average separation between the first downslope bond and the $H - L$ domain boundary (which occurs at a distance of $N/4$ from the centre of mass of the H cluster) scales as $\sim \sqrt{N}$. Let $P(r)$ be the probability that the first downslope bond is located at a distance r

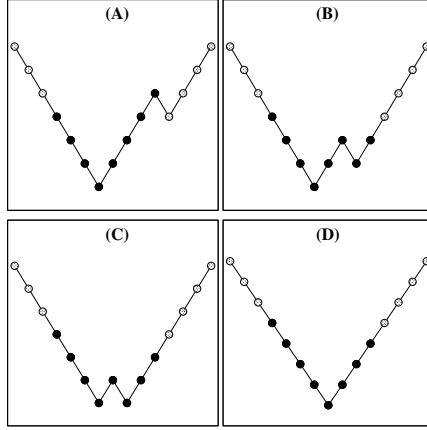


Figure 4.4: Motion of the deepest point over $\sim N^2$ time-scale. (A) An occupied local hill forms at the right edge of the particle cluster. (B) The occupied local hill, being unstable, zips through the pure domain of upslope bonds. (C) The local hill reaches the bottom of the valley. (D) The deepest point shifts one site to the right.

from the $H - L$ domain boundary, *i.e.* there is an upslope bond for all $j < r$, and a downslope bond at $j = r$. Within the mean-field approximation, this probability is given by,

$$P(r) = \prod_{j=1}^{r-1} \left(1 - \frac{2j}{N}\right) \frac{2r}{N} \quad (4.1)$$

The average value of r is then given by,

$$\langle r \rangle = \frac{2}{N} + \sum_{r=2}^{N/2} \sum_{j=1}^{r-1} \left(1 - \frac{2j}{N}\right) \frac{2r^2}{N} \quad (4.2)$$

To proceed further, we define

$$z = \prod_{j=1}^{r-1} \left(1 - \frac{2j}{N}\right) \quad (4.3)$$

$$\log z = \frac{N}{2} \int_{2/N}^{2(r-1)/N} \log(1-y) dy \approx \frac{2r}{N} - \frac{r^2}{N} \quad (4.4)$$

Performing the integration and using this expression in Eq. 4.2 one has, for large N ,

$$\langle r \rangle = \frac{2}{N} + (\sqrt{N} + 1/N)e^{1/N} \sim \sqrt{N} \quad (4.5)$$

4.3.2 Mechanism for large time behaviour of valley dynamics in IPS phase

In the limit of very long time, the H particle cluster will start moving around the system diffusively and the valley will naturally move along with it. This mechanism has been il-

illustrated in Fig. 4.5, which shows movement of an L particle through the H particle cluster. When the L particle reaches the bottom of the valley, the deepest point undergoes a displacement, along with the center of mass of the H particle cluster. Note that the time-scale for this process is rather large because the probability that the L particle, starting from the $H - L$ domain boundary, reaches the bottom of the valley, is very low and decays exponentially with the domain size (see our data in Fig. 4.6). As a result, the diffusivity of the valley in this regime $\sim e^{-\alpha N}$. Existence of an exponentially large time-scale breaks the translational invariance of the system but the relaxation time-scale is still algebraic, as demonstrated in Chapter 3.

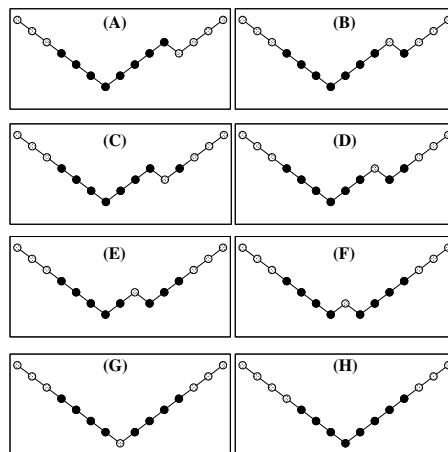


Figure 4.5: Motion of the deepest point over $\sim e^N$ time-scale. (A) Formation of a local hill at the right edge of the H particle cluster. (B) The rightmost H particle slides down the hill and gets detached from the cluster. (C) The resulting hill with L particle flips and another local hill with H particle is formed at the adjacent site. (D) Another H particle slides down the hill and detaches from the H cluster. (E) The L particle propagates down the valley. (F) At the bottom of the valley a local hill with L particle is formed. (G) This local hill flips and the deepest point of the valley shifts one site to the right. (H) The H particles to the left of the deepest point slide down, one after another, moving the center of mass of the particle cluster to one site to the right.

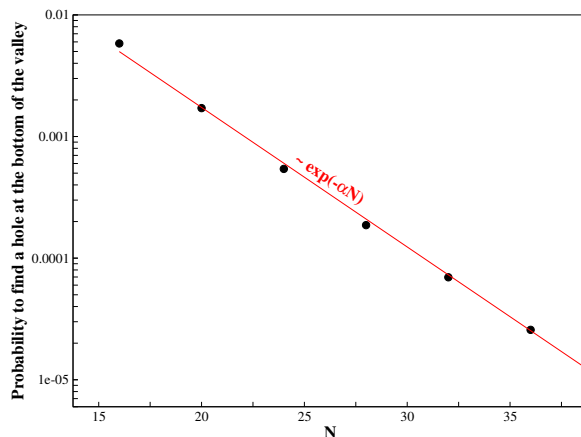


Figure 4.6: The probability to find an L particle at the deepest point of the surface falls off as $e^{-\alpha N}$ with system size where $\alpha = 0.261$. The data have been averaged over 10^6 histories.

4.3.3 Valley dynamics as an Ornstein-Uhlenbeck process in the IPS phase

Since any displacement of V away from C costs energy, which in turn gives rise to a restoring force which is harmonic, the diffusive motion of V can therefore be described by an Ornstein-Uhlenbeck process [58]. The corresponding Fokker-Planck equation in the continuum description has the form,

$$\partial_t P(x, t) = \frac{1}{\tau} \partial_x [xP(x, t)] + D \partial_x^2 P(x, t) \quad (4.6)$$

where $P(x, t)$ is the probability to find V at a distance x away from C . The first term on the right hand side represents the drift which can be positive or negative depending on the sign of x . The parameter τ sets the time-scale which is related to the steepness of the simple harmonic potential. We directly measure the drift term by measuring the bias experienced by V at a position x . In our lattice model, this bias is defined as the difference between the rightward and leftward hopping rate from that position. For a given value of x , we measure the average waiting times $T^\pm(x)$ for V to move to position $(x \pm 1)$. The bias is given by $v(x) = [1/T^+(x) - 1/T^-(x)]$. In Fig. 4.7a we plot the bias as a function of x and find that its magnitude increases linearly. This finding establishes the simple harmonic nature of the force field.

An alternative description of the above dynamics can also be given in terms of the random variable δh , the height difference between V and C . In a single time-step, the value of δh may change by one unit, or even two units (when the centre of mass is on a local hill which flips). We measure the average waiting times $T_n^\pm(\delta h)$ till δh changes by $\pm n$ units, with $n = 1, 2$ and calculate $V(\delta h) = \sum_{n=1,2} [n/T_n^+(\delta h) - n/T_n^-(\delta h)]$. We find that $V(\delta h)$ increases linearly with δh (see Fig. 4.7b). Note however, that by definition, δh can never cross the origin and

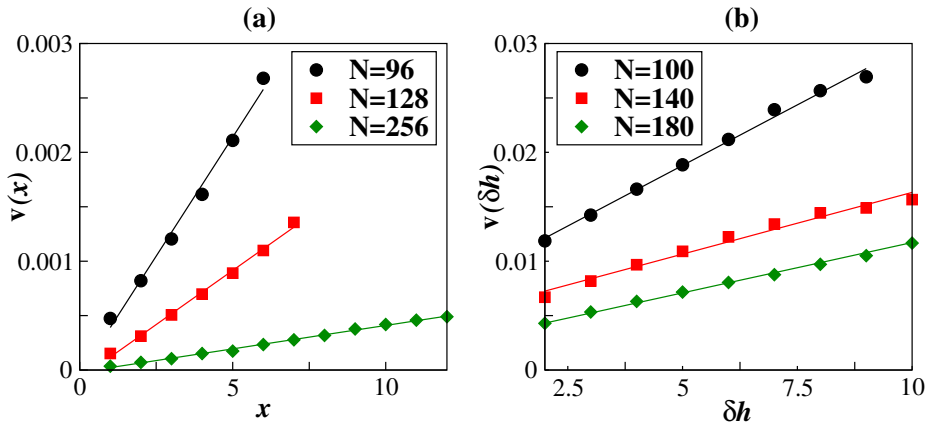


Figure 4.7: Motion of V as an Ornstein-Uhlenbeck process. (a): Velocity of V , when at a distance x away from C , increases linearly with x . (b): C experiences a restoring bias, when at a height δh above V and the bias increases linearly with δh . The data shown for 3 different system sizes have been averaged over at least 10^4 initial histories.

become negative. Therefore, its motion can be described as an Ornstein-Uhlenbeck process with reflecting boundary condition at the origin.

4.3.4 Scaling ansatz for dynamical correlation functions beneath the H -cluster in IPS phase

As shown in Fig. 4.3, there are several dynamical quantities associated with the fluctuations in the landscape. We show that a single scaling form suffices to describe the mean-squared fluctuation of all these quantities. To this end, we measure the mean-squared fluctuations

$$W(t, N) = \langle [Y(t) - Y(0)]^2 \rangle \quad (4.7)$$

as a function of time t , where $Y(t)$ is a generic stochastic variable. $Y(t)$ may denote the position of the deepest point of the valley; or width of the $H - L$ domain wall; or height of the centre of H -cluster, etc. For each such quantity, our data show that $W(t, N)$ grows algebraically with time for small t , with a possible N -dependent co-efficient while for large t , it saturates to an N -dependent value. More precisely, $W(t, N) \sim t^\alpha / N^\nu$ for small t , and $\sim N^\gamma$ when t is large. The values of the exponents α , ν and γ of course depend on the particular physical quantity $Y(t)$ represents, but a single scaling form suffices to describe all the results:

$$W(t, N) \sim N^\phi F(t/N^z) \quad (4.8)$$

The short and long time behavior of W imply that the scaling function $F(x) \sim x^\alpha$ for small x and saturates to a constant at large x with exponents that are related through $\phi = \gamma$ and

$z = (\gamma + \nu)/\alpha$. In Chapter 2, we have demonstrated that the dynamical exponent z which describes the coarsening during approach to the steady state is 2 for both IPS and FPS phases. In the IPS phase, the same value of z describes steady state dynamics as well. However, as we shall demonstrate shortly that in the FPS phase, while the typical time-scale for relaxation towards the steady state $\sim N^2$, the typical time-scale for steady state dynamics $\sim N^{3/2}$.

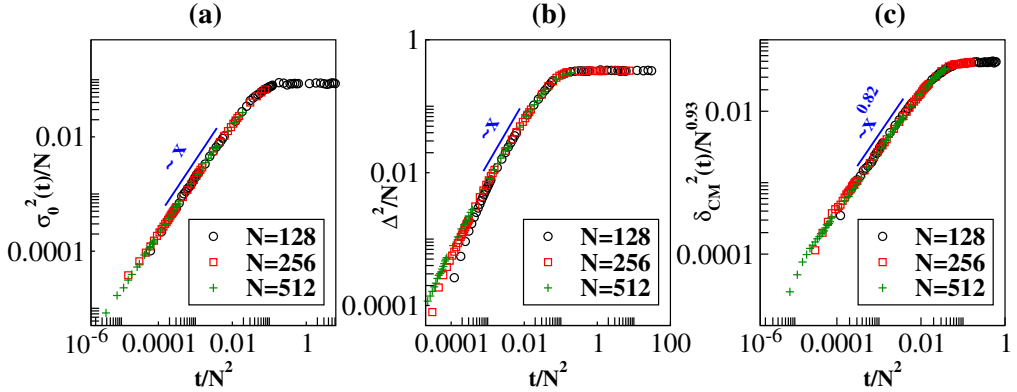


Figure 4.8: Scaling collapse of dynamical correlation functions in IPS phase. The scaling argument is t/N^z with dynamical exponent $z = 2$. For small argument, the scaling function grows as a power law with an exponent α . (a): For $\sigma_0^2(t)$ we find $\phi = 1$, $\alpha = 1$. (b): Scaling collapse of $\Delta^2(t)$ shows $\phi = 1$, $\alpha = 1$. (c): For $\delta_{CM}^2(t)$ best collapse is obtained for $\phi = 0.94$ and $\alpha = 0.82$. The maximum error bar in these exponent values are ± 0.02 . All data are averaged over at least 10^4 initial histories.

4.3.5 Landscape dynamics beneath the L -cluster in the IPS phase

In the previous subsections, we discussed the dynamics of the ordered part of the landscape, in the region occupied by H particles. The landscape beneath the L -cluster is disordered in both the IPS and FPS phases. In this part the dynamics of the landscape actually corresponds to that of an open-chain exclusion process, on mapping the upslope bonds to particles and the downslope bonds to holes. For an IPS phase, in the language of particles and holes, in the L -region the dynamical rules (see Eq. 2.2) are those of a symmetric exclusion process (SEP) [50]. The ordered domains of upslope and downslope bonds in the H -region then act as reservoirs of particles and holes that are present at the two ends of the macroscopic SEP segment, and drive a current through it. Earlier studies on an open-chain SEP [50] show that the density profile of particles shows a linear gradient $\sim 1/N$ which supports a diffusive current $\sim 1/N$ in the system. We have verified both these predictions in Chapter 3.

To carry the correspondence with the open system further, we also compare the dynamical correlation functions in our system with that of an open-chain SEP. The auto-correlation function of an upslope bond at a distance r away from the $H - L$ domain boundary is shown in Fig. 4.9a. The continuous line in this plot shows the result expected for open-chain SEP,

where $A(r, t) = \frac{\rho(r)(1-\rho(r))}{\sqrt{2\pi}} t^{-1/2}$, with $\rho(r)$ being the local density at a position r [59]. We find a good agreement between this prediction and our simulation results. In Fig. 4.9b, we plot the mean-squared displacement of a tagged upslope bond at a distance r from the $H - L$ domain boundary. This corresponds to the mean-squared displacement of a tagged particle in an open-chain SEP and is expected to behave as $\sigma^2(r, t) = \sqrt{\frac{2}{\pi}} \frac{1-\rho(r)}{\rho(r)} t^{1/2}$ [60], up to a time $t \sim N^2$. Beyond this time, the tagged particle displacement becomes larger than the length scale over which $\rho(r)$ varies, and $\sigma^2(r, t)$ then shows a faster growth. Our data in Fig. 4.9b shows this effect clearly.

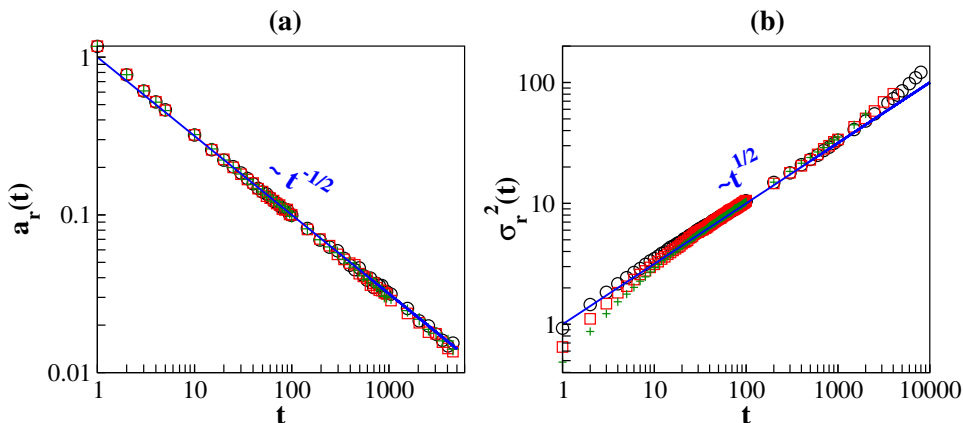


Figure 4.9: The correspondence between the L region in the IPS phase and an open-chain SEP. a: Scaled auto-correlation function of an upslope bond at a distance $r + L/4$ from C , where the average density of upslopes is denoted by $S^+(r)$. We plot $a_r(t) = \frac{\sqrt{2\pi}}{S^+(r)(1-S^+(r))} A(r, t)$ for 3 different r and show that it decays as $t^{-1/2}$. The system size used is 2048. The data shown here have been averaged over at least 10^6 initial histories. b: Tagged mean-squared displacement of an upslope bond at a distance $r + L/4$ from C . We plot $\sigma_r^2(t) = \sqrt{\frac{\pi}{2}} \frac{S^+(r)}{1-S^+(r)} \sigma^2(r, t)$ for 3 different values of r and show that it grows as $t^{1/2}$. We have used $N = 512$ here. These data have been averaged over at least 10^4 initial histories.

4.4 DYNAMICS IN THE FPS (FINITE CURRENT WITH PHASE SEPARATION) PHASE

For the FPS phase, the valley dynamics shows a different behavior from the IPS phase. In this case, the landscape holding the H -cluster forms a macroscopic valley which has a rugged bottom, while the part holding the L -cluster is flat (see Fig. 4.1). Although the deepest point V of the valley still makes excursions around the centre of mass C of the H -cluster, this motion is not diffusive as in the IPS phase. Our data show that $\sigma_0^2(t)$ grows sub-diffusively $\sim t^{1/2}$. The sub-diffusive regime is observed after a large non-scaling regime but before the saturation sets in, and is observable provided N is large enough. Our data show $\alpha = 0.5 \pm 0.01$, $\nu = -0.17 \pm 0.02$, $\gamma = 0.92 \pm 0.03$, which yields $z = 1.5$, $\phi = 0.92$ and a scaling

function which grows with an exponent $1/2$ close to the origin. The corresponding scaling collapse is shown in Fig. 4.10a.

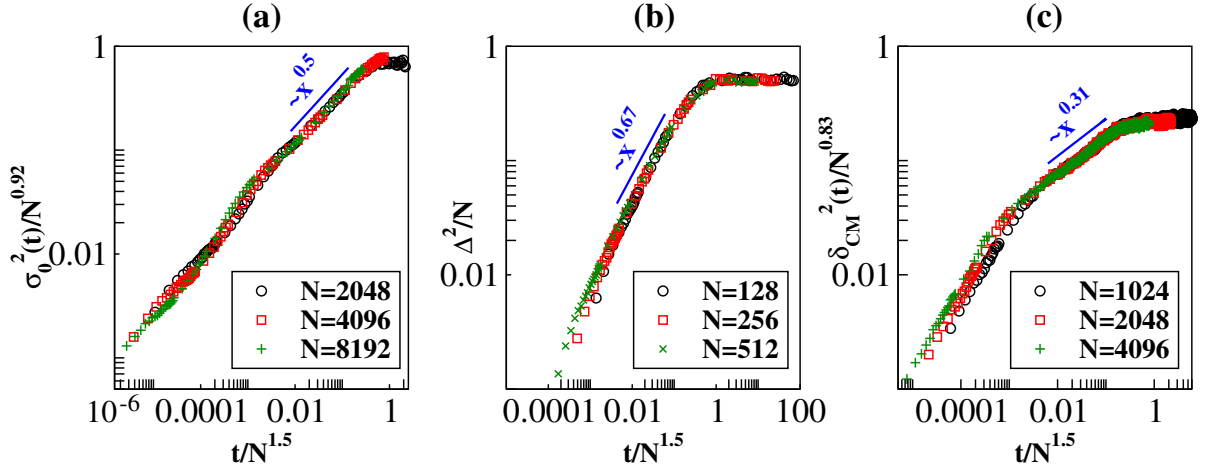


Figure 4.10: Scaling collapse of dynamical correlation functions in FPS phase. In this case the scaling argument is $t/N^{3/2}$. For small argument the scaling function grows with a power α and for large argument saturates to a constant value. (a): Data for $\sigma_0^2(t)$ give $\phi = 0.92$ and $\alpha = 0.5$. (b): For $\Delta^2(t)$ we find $\phi = 1$ and $\alpha = 0.67$. (c): For $\delta_{CM}^2(t)$ best collapse is obtained for $\phi = 0.83$ and $\alpha = 0.31$. The maximum error bar is ± 0.02 . All these data have been averaged over at least 10^4 steady state configurations.

Note that in the FPS phase, the valley is not as sharp as the one seen in IPS phase (see Fig. 2.2). Instead of a single deepest point, the bottom of the valley is often rugged and may contain more than one site with the minimum height. In our simulation, we have chosen one such site and every time a random update causes the height of a site to fall below the current minimum, we count it as a displacement of the deepest point. To verify that the value of the exponent is not tied to the particular method of determining it, we also estimate the exponent by monitoring the time dependence of the mean-squared displacement of a tagged upslope bond that is situated at a distance r away from the centre of mass in the H region. As shown in Fig. 4.11, this quantity also grows with the exponent $1/2$, as did $\sigma_0^2(t)$.

An important qualitative difference in the scaling form in IPS and FPS phase is the sign of the exponent ν . While ν is positive for IPS phase, in the FPS phase we find $\nu < 0$. This implies that as N becomes larger, the growth of $\sigma_0^2(t)$ with time becomes slower for IPS phase, and faster for FPS phase. This difference can be related to the difference in the current fluctuation properties. Note that for a general current-carrying system, in which the state breaks translational invariance, the current fluctuations in steady state can be very different in parts of the system, though the mean current is uniform. Indeed, we find the current fluctuation at the bottom of the valley is very different from that measured in the middle of the L -phase. The exponent ν is related to the fluctuation properties at the bottom of the valley. We find that for an system in FPS phase, which carries a finite current, the current

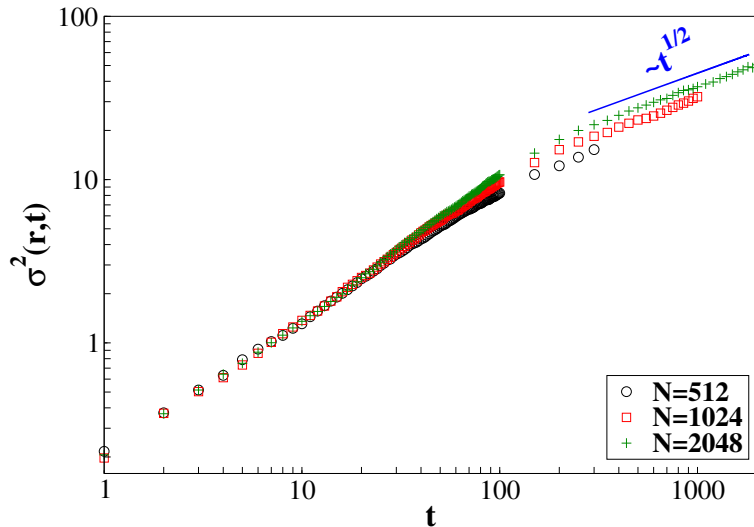


Figure 4.11: Tagged mean squared displacement $\sigma^2(r,t)$ of an upslope bond inside the H -cluster initially at a distance r from the deepest point shows a sub-diffusive behaviour and grows as $t^{1/2}$. Here, we tag an upslope bond at a distance $N/16$ from the deepest point and show the plots for 3 different N values. We observe an initial non-scaling behavior for $t \lesssim 100$ where the growth is steeper. These data have been averaged over at least 10^5 initial configurations.

fluctuation at the valley bottom grows with N (see Fig. 4.12). By contrast in the IPS phase, where current $\sim 1/N$, its fluctuations get smaller as N increases (Fig. 4.12). This ties in with the different signs of ν in the two phases.

4.4.1 Height fluctuations induced by valley dynamics in FPS phase

In the FPS phase, $\Delta^2(t)$ grows sub-diffusively with time with an exponent $2/3$ (Fig. 4.10 b), which is different from the exponent $1/2$ measured for the mean-squared displacement $\sigma_0^2(t)$ of V . Note that due to the rugged structure at the bottom of the valley in this case, every movement of V may not yield a corresponding change in the value of Δh . See Fig. 4.13 for a specific illustration of this point. This means that unlike IPS phase, here we do not have a one to one correspondence between the dynamics of V and Δh . The two distinctly different exponents observed in Figs. 4.8 and 4.10 reflect this difference. For $\delta_{CM}^2(t)$, we find $\alpha = 0.31 \pm 0.02$, $\nu = -0.36 \pm 0.02$, $\gamma = 0.83 \pm 0.03$ and $z = 3/2$ (Fig. 4.10c).

In the FPS phase, the valley motion cannot be described in terms of an Ornstein-Uhlenbeck process. This is not surprising, in view of the sub-diffusive nature of the valley dynamics (an underlying Ornstein-Uhlenbeck process would have yielded a diffusive motion of the deepest point). Indeed, Fig. 4.14 shows that the bias experienced by V when it is at a height δh below C , grows sub-linearly with δh .

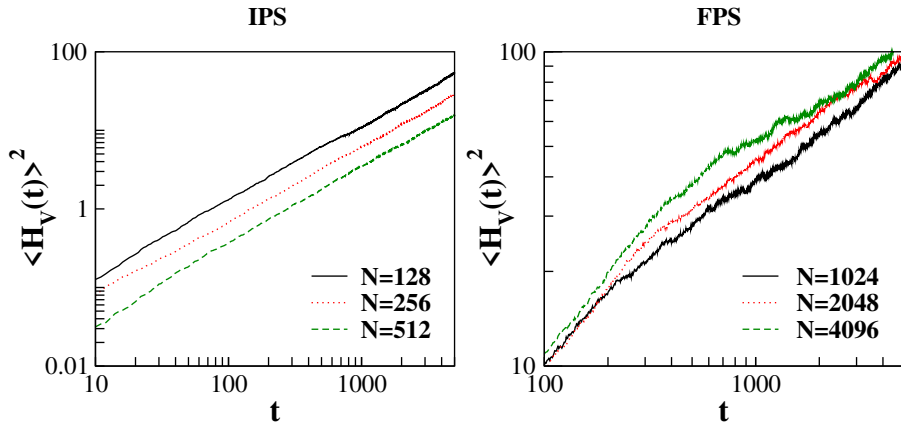


Figure 4.12: We measure the current fluctuation $\langle H_V^2(t) \rangle = \langle [(h_V(t) - h_V(0)) - vt]^2 \rangle$ in the IPS and FPS phases at the bottom of the valley, where $h_V(t)$ denotes the height of the deepest point of the landscape at an instant t in the steady state and v is the average velocity of the system. In the left panel we show that for the IPS phase, the current fluctuation decreases as a function of N , while in the right panel, the current fluctuations in the FPS system grow with the system size. These data have been averaged over at least 10^4 initial histories.

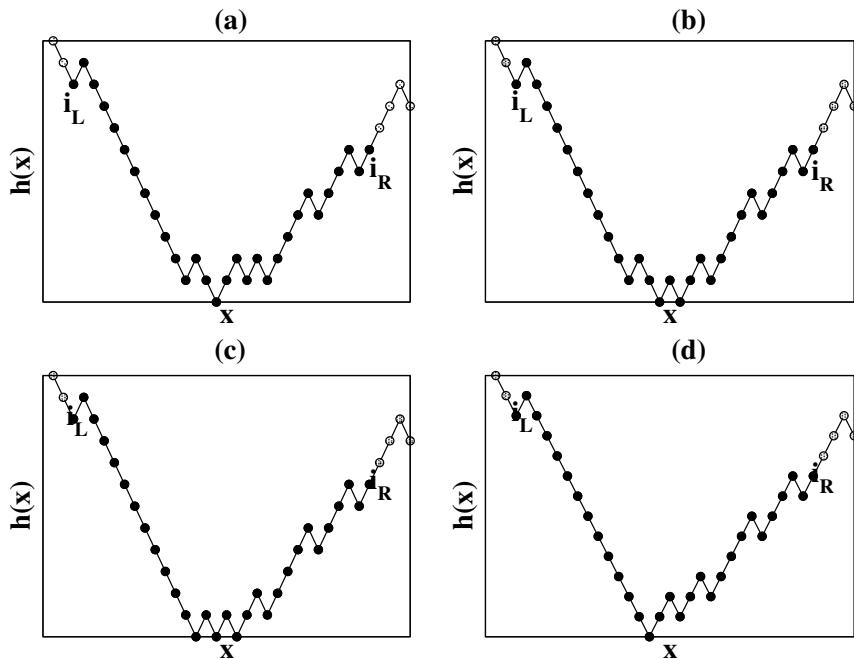


Figure 4.13: We explicitly illustrate that it is possible for the deepest point in an FPS phase to move without causing any change in the height difference between the edges of the H -cluster. Figs (a), (b), (c), (d) show time-evolution of a local configuration. We find that the finite fraction of impurities present within the majority up(down)-slope domains causes the deepest point to shift without causing any change in the heights of the right (i_R) and left (i_L) edges of the H cluster.

4.4.2 Landscape dynamics beneath the L -cluster in FPS phase

In the FPS phase, a similar mapping of upslope (downslope) bonds to particles (holes) brings out a correspondence with an open-chain asymmetric exclusion process (ASEP) in the max-

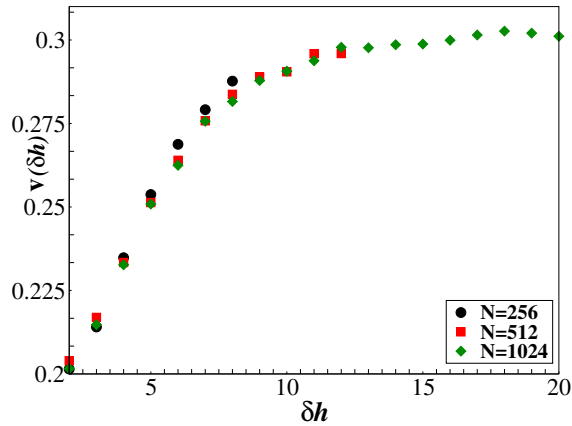


Figure 4.14: Velocity of V when at a height δh below C has a non-linear dependence on δh in the FPS phase. This motion cannot be described as an Ornstein-Uhlenbeck process, unlike IPS phase. The data shown for 3 different system sizes have been averaged over at least 10^4 histories.

imal current phase [20]. In Chap. 3, we have explicitly shown that the density of upslope bonds in the bulk of the L -region is $1/2$ and near the $H - L$ domain boundaries it shows an algebraic variation, as expected in a maximal current phase. To carry out the correspondence further, we measure the mean-squared displacement of a tagged upslope bond in the L -region. Note that due to the presence of a kinematic wave [61], the density fluctuations in an ASEP with density ρ possess a relative velocity with respect to the individual particles. To probe how a particular density fluctuation decays with time, one needs to measure the tagged mean-squared displacement of a particle with a ‘sliding tag’ that keeps changing with time. The amount of ‘slide’ in the tag accounts for the relative motion of the tagged particle with respect to the density fluctuations. In [62, 63] this method was employed for an ASEP with periodic boundary conditions. In our work, we generalize this method for an open system and find that the tagged mean-squared displacement of an upslope bond grows with time with an exponent close to $2/3$, as expected for an ASEP (see Fig. 4.15).

In the stationary state of an ASEP, the drift velocity (v_p) of the individual particles is given by J/ρ , where J, ρ are particle current and density respectively. Besides this, the velocity (v_k) with which the coarse-grained density fluctuations are transported throughout the system is given by $\frac{\partial J}{\partial \rho}$ and is called the kinematic wave velocity [61, 64]. Hence, in the rest frame of the density fluctuations, the particles move with velocity $v_p - v_k$. In order to capture the correct dynamical exponent with which the mean squared fluctuation in the position of a tagged particle in the maximal current phase grows, we take recourse to the method of sliding tags [62, 63]. For an ASEP with open boundaries, due to finite rates of injection (ejection) at the boundary sites, the tags of the particles keep changing with time. To take this into account, one may consider a segment of length l sufficiently away from the boundaries within the

bulk and within this segment, tag all the particles at $t = 0$. Due to hard-core repulsion, none of these can cross each other. We measure the following quantity:

$$\Lambda^2(t) = \langle [y(m', t) - y(m, 0)]^2 \rangle - \langle [y(m', t) - y(m, 0)] \rangle^2 \quad (4.9)$$

where, m, m' are particle tags related by $m' = m - \rho ut$, $\{y(m, t)\}$ give the locations of the particles at time t and $u = v_p - v_k$. Here, $\rho = 1/2$ as the segment is in the maximal current phase [20]. The angular brackets denote averaging over both initial histories and stochastic evolution. By carrying out this measurement until the tagged particles approach the boundaries of the segment of length l , one finds $\Lambda^2(t) \sim t^{2/3}$. On the contrary, if one measures the mean-squared displacement σ^2 of a tagged up-slope bond without incorporating the tag shift, one observes diffusive behaviour (see Fig. 4.15 inset).

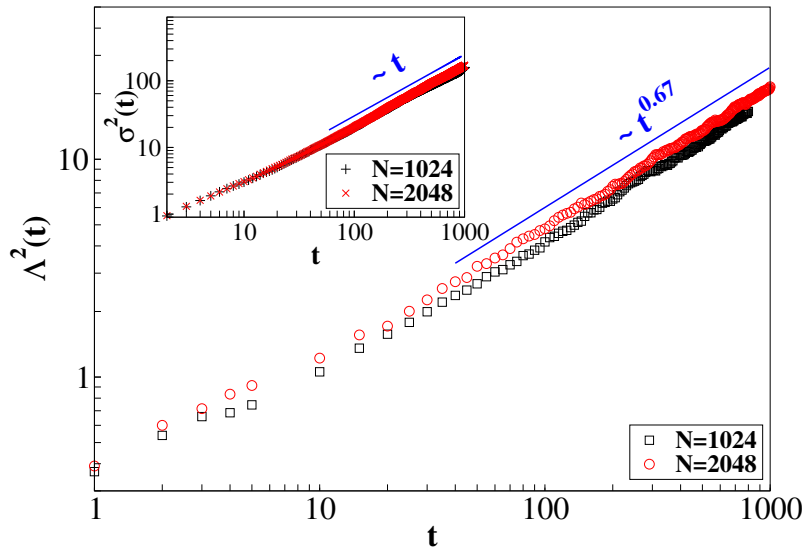


Figure 4.15: Main plot shows the sliding tag correlation function $\Lambda^2(t)$ for an upslope bond initially in the maximal current phase and find that it grows as $t^{0.67}$. Inset shows the variance $\sigma^2(t)$ of a tagged upslope bond in the same phase. When the relative shift between the tagged bond and the density patches is not taken into account, measurement of the tagged mean squared displacement does not capture the correct dissipation and shows a diffusive behaviour. We have used $N = 1024, 2048$ here. We have taken the density of H particles to be $1/2$ and hence the length of the open chain in maximal current phase is of length $N/2$. These data have been averaged over at least 10^3 initial histories.

4.5 CONCLUSION

Our study of the dynamical properties of a strongly coupled system of heavy and light particles on a fluctuating landscape has focused on the phase separated states that result when linear hydrodynamics predicts that the homogeneous system is unstable. As detailed

in Chapter 2, there are several different phases which arise as coupling constants are changed. The dynamics of two such ordered phases (SPS and FDPO) have already been studied in [24, 25] and [51] respectively. In this chapter, we have chosen to focus on the IPS and FPS phases. Their dynamic properties reflect some similarities and some differences.

Perhaps the single most striking feature is the existence of two very different time scales for the particles and the landscape in steady state, despite the strong coupling between them. Movement of the centre of mass of the macroscopic H cluster occurs on a time scale which grows exponentially with system size, $\sim \exp(\alpha N)$, whereas landscape fluctuations involve power law growths up to a time $\sim N^\gamma$. This dichotomy can be traced to the fact that the disordered landscape beneath the L cluster generates slope fluctuations, which reach the valley bottom and cause it to undulate, without a concomitant shift of the particles themselves. Interestingly, there is no such dichotomy in the coarsening properties of the systems — as shown in our data in Chapter 3, the approach to the steady state is described by the same power laws in time for both the IPS and FPS phases.

An interesting aspect of the coexisting phases in both cases is that their properties relate to well-known paradigms in the field, on employing a particle-hole description of the landscape slopes in the L region. Thus, in the IPS we have effectively an open simple exclusion process (SEP), with boundary conditions which set up a gradient and cause a current to flow. In the FPS, the corresponding particle-hole model is the asymmetric simple exclusion process (ASEP), in the maximal current phase. The currents carried in both cases translate into a bodily downward movement of the interface, resulting in a velocity which is $\mathcal{O}(1/N)$ for the IPS and $\mathcal{O}(1)$ for the FPS.

Although we have attempted to be exhaustive and to rationalize the observed results to the extent possible, some mysteries remain. First, why is the dynamic exponent $z = 2$ in the coarsening regime of the FPS, whereas in steady state, it has the value $3/2$, as expected on the basis of the ASEP analogy? Secondly, why is ν negative in the FPS phase? We have pointed out a possible correlation between this and enhanced current fluctuations at the valley bottom, but it would be desirable to make this connection stronger.

LH MODEL IN TWO DIMENSIONS — SQUARE AND TRIANGULAR LATTICE GEOMETRIES

5.1 INTRODUCTION

In this chapter we discuss results on our particle-landscape model in two dimensions for different lattice geometries. We address two important questions here: (a) Does the phase diagram shown in Fig. 2.1 (see Chapter 2) remain valid for all particle densities even in two dimensions? (b) Does the phase diagram remain robust for different kinds of lattice symmetries? If so, how do the topologies and the shape of the boundaries of the different ordered regions change for different lattice geometry? We find that the qualitative nature of the phase diagram remains valid for different lattice geometries in two dimensions. However, there are strong finite size effects that happen to manifest themselves in two dimensions. For small system sizes, one encounters different types of height topologies in the surface beneath the particle cluster. For large system sizes, however, one can numerically observe only a single kind of topology. We present a simple scaling argument that rationalises that in the thermodynamic limit, only a single type of configuration should survive. We present our model and results for two dimensional square and triangular lattice geometries. Part of results discussed in this chapter have been published in [47–49].

5.2 RESULTS ON A TWO DIMENSIONAL SQUARE LATTICE

The surface in two dimensions is simulated through a discrete solid-on-solid algorithm, where the height difference between the nearest neighbors on a square lattice is maintained at ± 1 . Let $h(i, j)$ denote the height of the site (i, j) on the lattice. This site is said to be on a local hill, if all its four neighbors with coordinates $(i \pm 1, j)$ and $(i, j \pm 1)$ have height $h(i, j) - 1$. Similarly, the site (i, j) is said to be in a valley when the neighbors have height $h(i, j) + 1$. The two dimensional surface evolves in time by switching between the hills and the valleys [65]. In our model, a site is selected at random. If it is on a hill, then it can flip to a valley when its height gets reduced by two units. This flipping rate is $(E + b)$ when the site is occupied by

an H particle and $(E - b')$ when it is occupied by an L particle. Similarly, if the chosen site happens to be in a valley, then its height can increase by two units and it becomes a hill. The switching rate in this case is $(E - b)$ when an H particle is present, and $(E + b')$ when an L particle is present. For updating the particles, we select a bond (horizontal or vertical) of the square lattice. If the two sites adjacent to the bond are occupied by two different species of particles, then their positions are exchanged with rate $(D + a)$ if after the exchange, height of the H particle decreases. The reverse exchange occurs with rate $(D - a)$.

5.2.1 Fast coarsening to IPS and FPS phases on a square lattice

The properties of the phases discussed in Chapter 2 remain qualitatively valid in two dimensions. The H and L particles form compact clusters. The shape of these two dimensional clusters depends on the topography of the surface heights. For small system sizes, we observe an interesting finite size effect that gives rise to two different surface geometries which we discuss in the next section. The relaxation time-scale to the IPS and FPS phases remain algebraic on a two-dimensional square lattice which we confirm by measuring the two-point density-density correlations between the H -particles (see Fig. 5.1).

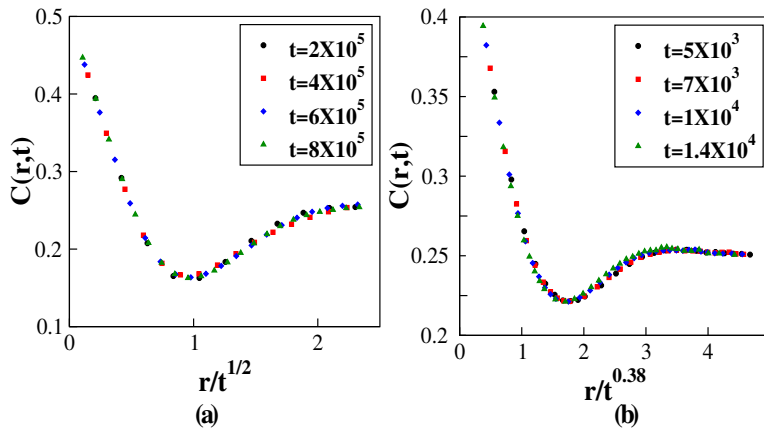


Figure 5.1: Scaling of particle density correlation in the coarsening phase on a two dimensional square lattice. The equal time density correlation for the particles $C(r, t)$ shows a collapse when r is scaled by $\mathcal{L}(t) \sim t^{1/z}$. (a) and (b) show scaled data for $b = 0.5, b' = 0$ and $b = 0.3, b' = -0.2$ respectively. For IPS phase, $z \simeq 2$ and FPS phase shows $z \simeq 2.6$. We have used $N = 256 \times 256$ here.

5.2.2 Finite size effects in topologies on a square lattice

For numerical simulations, we start with a flat initial configuration of the surface and random configuration for the particles and evolve the system in time, following the algorithm

described above. The phases obtained in this case are similar to those in one dimension. In the ordered phases, the H and L particles undergo complete phase separation and the landscape beneath the H cluster orders to form a deep valley. In the SPS phase, the entire landscape is ordered to form a deep valley accommodating the H -cluster at the bottom of it. In the IPS phase, the landscape beneath the L -region shows a linear variation of height along x or y direction, while in the FPS phase it is disordered. Inside the valley, as the deepest point is approached from both x or y directions, the height decreases and this means that the equal height contours have diamond-like shape. Using an analysis very similar to that discussed in Sec. 3.4.3, one can explain the clustering of H -particles in the IPS phase.

However, for IPS and FPS phases we have also encountered another type of configuration on a two dimensional square lattice, where instead of a single point with minimum height, the surface develops a line of such points and the shape of the surface looks like a ‘trench’ or ‘wedge’ (see Fig. 5.2). Through extensive numerical simulations we have also verified that such configurations are results of finite size of the system and for larger systems we only find diamond-shaped contours. The simple calculation presented below lends support to this finding.

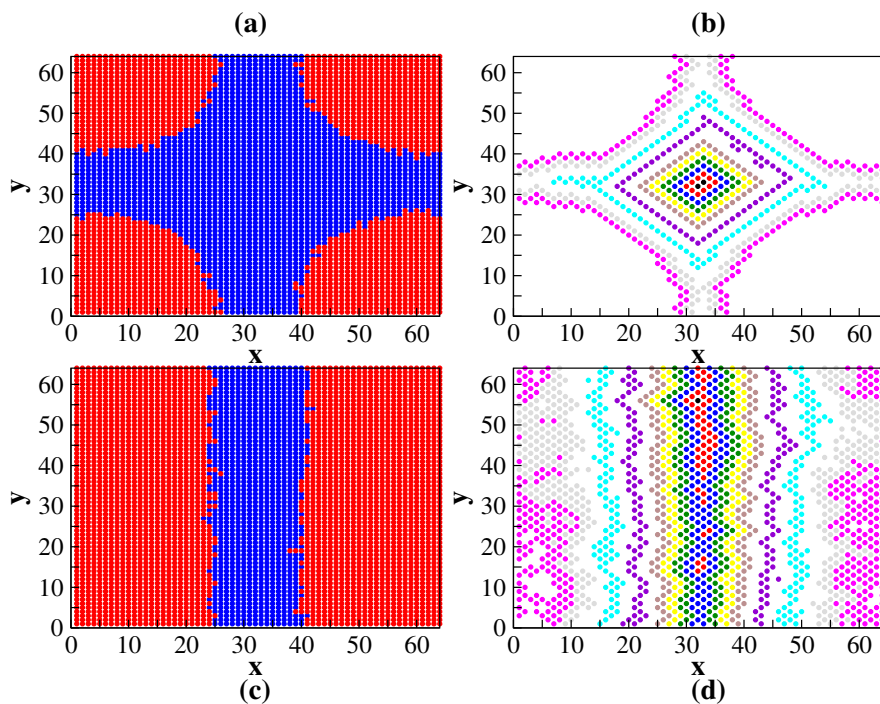


Figure 5.2: Representative plots for diamond and wedge type configurations in the IPS phase in two dimensions on a 64×64 square lattice. In (a) and (c), $H(L)$ clusters are shown in red(blue), while (b) and (d) show the equal-height contour plots.

The total gravitational energy of H -particles is $\sum_{ij} n_{ij} h(i, j)$, where n_{ij} is the H -particle occupancy at site (i, j) , and $h(i, j)$ is the height at that site measured from the flat (or logarithm-

mically rough) part of the landscape, in the L -region. Note that when equal height contours are diamond shaped, then the number of sites with a given height h above the minimum equals $4h$. For a perfectly ordered configuration, the H particles fill the landscape up to a certain height level h_0 above the minimum. Thus the total number of sites occupied by H particles is,

$$1 + 4 \sum_{h=1}^{h_0} h = \rho N^2 \quad (5.1)$$

where ρ is the density of H -particles. It follows from this relation that $h_0^2 \approx \rho N^2/2$. The number of H particles at a height j below the maximum occupied level is $4(h_0 - j)$ and hence the total energy becomes,

$$E_D = -4 \sum_{j=0}^{h_0-1} (h_0 - j)j - h_0 = -\frac{2}{3}h_0(h_0 + 1)(h_0 - 1) - h_0 \approx -\frac{2}{3}\left(\frac{\rho}{2}\right)^{3/2} N^3 \quad (5.2)$$

to the leading order in N . For a wedge-shaped surface, on the other hand, the equal-height contours are horizontal or vertical lines, running parallel to the line of height minima. The number of sites with a given height h in this case is $2N$ and the highest occupied level h_0 in this case is $\rho N/2$. This gives the total energy of H -particles in a wedge-like arrangement as,

$$E_W = -\frac{\rho^2 N^3}{4} - \frac{\rho N^2}{2} \approx -\frac{\rho^2 N^3}{4} \quad (5.3)$$

to leading order in N . For large N , it follows from Eqs. 5.2 and 5.3 that $E_D < E_W$ unless ρ is very high ($\rho \gtrsim 0.89$). In our simulations, we mainly consider $\rho \lesssim 1/2$ and for our case diamond-like arrangements are energetically more favorable for large systems. It will be interesting to study the limit $\rho \gtrsim 0.9$ to see if wedge-shaped configurations survive even for large N .

5.3 STEADY STATE DYNAMICS ON A SQUARE LATTICE

In this section, we present our simulation results on the dynamical correlations in the two-dimensional model defined in Sec. 5.2. Algebraically fast time scales in relaxation and steady state dynamics of the landscape are observed in the IPS and FPS phases in two dimensions as well. We monitor the mean squared displacement of the deepest point in the valley along the x and y directions in the IPS and FPS phases (Fig. 5.3a, b).

We find that in the IPS phase, at short times $t \ll N$, the valley moves diffusively with the diffusion constant $\sim 1/N$. The mean squared displacement then saturates at a finite value of order 1 until at large times it again starts growing diffusively, but with a diffusion

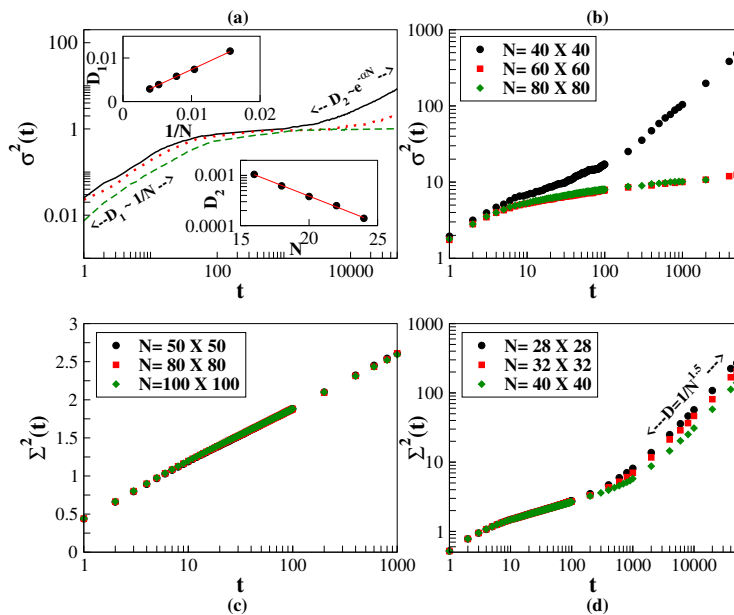


Figure 5.3: Landscape dynamics in two dimensions. **(a)** Mean squared displacement $\sigma^2(t)$ of the deepest point of the valley along the x -direction as a function of time for three different system sizes, 24×24 (solid line), 32×32 (dotted line), 40×40 (dashed line) in the IPS phase. Top and bottom insets show the short and large time diffusion constants $D_1 \sim 1/N$ and $D_2 \sim e^{-\alpha N}$ where $\alpha = 0.25$. **(b)** $\sigma^2(t)$ in the FPS phase for 4 different system sizes. While the initial growth and saturation does not show any dependence on the system size, the large time diffusivity falls off exponentially as the system size (data not shown here). **(c)** The height fluctuation $\Sigma^2(t)$ as a function of time in the part of the surface holding the L cluster in IPS phase. The fluctuations grow logarithmically in time as is characteristic of an Edwards Wilkinson surface in two dimensions. **(d)** $\Sigma^2(t)$ in the FPS phase shows a sub-diffusive regime that remains valid upto $t \sim 100$. This is followed by a diffusive growth at large times with the diffusion constant falling off as a power law $\sim N^{-1.5}$.

constant $\sim e^{-\alpha N}$. In the FPS phase, we monitor the same quantity and find that it grows sub-diffusively and saturates at a finite value. At large times $\sim e^{\alpha N}$, the valley performs diffusive motion with an exponentially small diffusion constant.

We also measure height fluctuations ($\Sigma^2(t)$) in the part of the surface occupied by the L particles and find that it shows a logarithmic growth for the IPS phase and a diffusive growth in the FPS phase with a diffusion constant $\sim N^{-1.5}$ (see Fig. 5.3c, d). Note that, while in the IPS phase, the surface beneath the L -cluster shows the logarithmic behaviour characteristic of an Edwards Wilkinson surface [66], in the FPS phase, there is a clear deviation from the behaviour of usual Kardar-Parisi-Zhang surfaces where one expects $\Sigma^2(t) \sim t^{2\beta}$ with $\beta \simeq 0.23$ [67].

The LH model can be simulated on a two dimensional triangular lattice using similar update rules as described in Sec. 5.2. However, since the triangular topology allows for 6 nearest neighbours, the definitions of hills and valleys are different from that on a square lattice. The height update rules for the surface is described as follows. Let $h(i, j)$ denote the height of the site (i, j) on the triangular lattice. This site is said to be on a local hill, if the averaged height of all its six neighbors with coordinates $(i \pm 1, j)$, $(i, j \pm 1)$, and $(i \pm 1, j \pm 1)$ is lower than $h(i, j)$. Similarly, the site (i, j) is said to be in a valley when the averaged height of all the neighbors is higher than $h(i, j)$. The two dimensional surface evolves in time by switching between the hills and the valleys as described earlier. While on a square lattice, the flipping of hills into valleys and vice versa conserves the height difference between each of the nearest neighbours, the same might not always be true for the dynamics on a triangular lattice. Similarly as on a square lattice, we start with a flat initial condition for the height profile of the surface and a randomly distributed particle profile. At first a site is selected at random. If the site (i, j) is on a hill, then it can flip into a valley, provided the magnitude of height difference between all the nearest neighbours after the flip never exceed unity — it can assume only three values $1, 0, -1$. This flipping rate is $(E + b)$ when the site is occupied by an H particle and $(E - b')$ when it is occupied by an L particle. Similarly, if the chosen site happens to be in a valley, then the switching rate is $(E - b)$ when an H particle is present, and $(E + b')$ when an L particle is present. For updating the particles, we select a bond of the triangular lattice. If the two sites adjacent to the bond are occupied by two different species of particles, then their positions are exchanged with rate $(D + a)$ if the height of the H -particle decreases after the transition. The reverse exchange occurs with a rate $(D - a)$. If the height difference across the chosen bond is zero, the particles diffuse with a rate D .

5.4.1 Finite size effects in topologies on a triangular lattice

We find that similar to our observations on a square lattice, the phase diagram shown in Fig. 2.1 qualitatively holds true for a triangular lattice. However, on a triangular lattice, we have encountered three different topologies for IPS and FPS phases with equal height contours looking like hexagons, wedges, and triangles. We show the top views of the particles clusters and the equal height contours in Fig. 5.4. Similarly as in Sec. 5.2.2, we show a scaling calculation for energies of the different topologies obtained on a triangular lattice.

Following the arguments presented in Sec. 5.2.2, we calculate the energies for perfectly ordered hexagonal and triangular topologies obtained on the triangular lattice. For a perfect hexagonal topology, the number of sites at a given height h above the minimum is $6h$. Hence

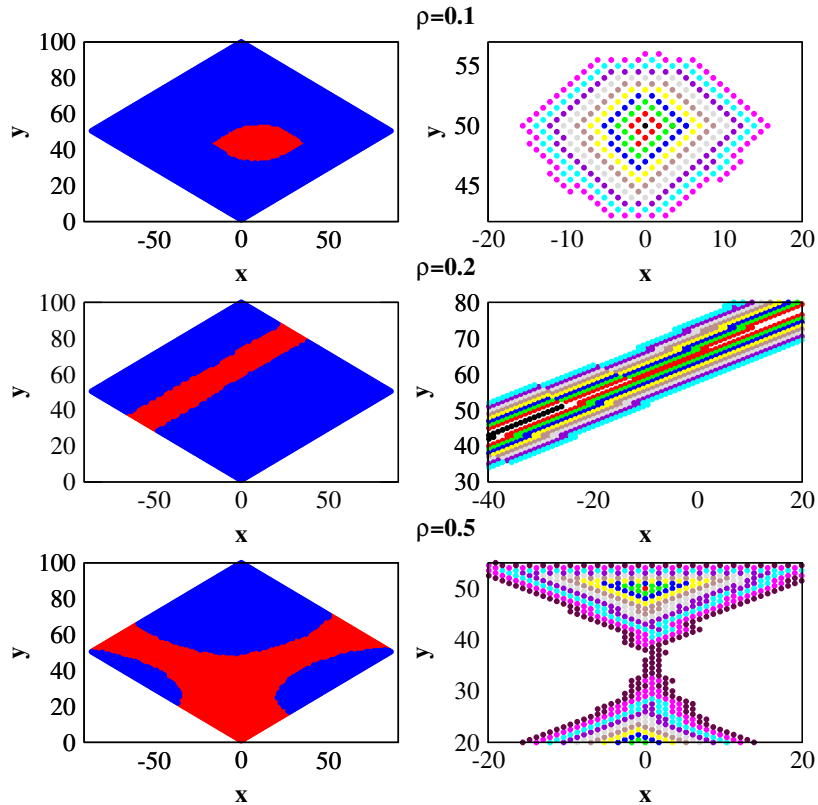


Figure 5.4: Representative plots for hexagonal, wedge, and triangular type configurations in the IPS phase in two dimensions on a 100×100 triangular lattice for three different densities. The left panels show the $H(L)$ clusters in red(blue), while the right panels show the equal-height contour plots.

the total number of sites ρN^2 occupied by H particles is $1 + 6 \sum_{h=1}^{h_0} h$, which yields $h_0^2 \approx \frac{\rho N^2}{3}$ for large N . The total energy for a perfectly hexagonal topology is hence,

$$E_H = -6 \sum_{j=0}^{h_0-1} (h_0 - j)j - h_0 = -\left(\frac{\rho N^2}{3}\right)^{3/2} - \frac{\rho N^2}{3} \approx -\left(\frac{\rho}{3}\right)^{3/2} N^3 \quad (5.4)$$

For a perfect triangular topology, on the other hand, the maximum height $h_0 \approx \frac{2}{9}\rho N^2$ and the energy is given by,

$$E_H = -9 \sum_{j=0}^{h_0-1} (h_0 - j)j - h_0 \approx -\frac{3}{2} \left(\frac{2}{9}\rho\right)^{3/2} N^3 \quad (5.5)$$

The above calculation predicts that for low densities ($\lesssim 0.6$), $E_H < E_W < E_T$, *i.e.*, the hexagonal topologies will be favoured over the wedge and triangular topologies. In our simulations, we indeed find that for low densities (~ 0.1), the equal height contours look

like hexagons. However, for densities $0.2 < \rho < 0.3$ we encounter wedge phases and beyond that, we find triangular topologies for $0.3 < \rho < 0.5$ even for a 200×200 triangular lattice. Our scaling calculation for energies of different topologies ignores boundary contributions from the particle clusters and assumes that beyond h_0 , the surface is perfectly flat. This might be a reason why for high densities our scaling argument fails to match the numerical simulations. A good agreement might be observed at really large system sizes which have not been possible for us to access.

5.5 CONCLUSION

To conclude, we have studied the two-way coupled particle-landscape model in two dimensions for two different types of lattice geometries — square and triangular. Although the qualitative nature of the phase diagram 2.1 remains same in two dimensions as well, we encounter several types of topologies that occur in finite size systems. We present a scaling argument which shows that in the thermodynamic limit there should be a single type of topology that is energetically favoured. Our numerical simulations for a square lattice confirm that for large system sizes, indeed the diamond type of configuration survives because of having the lowest energy. However, on a triangular lattice, the finite size effects seem stronger and for the largest possible system size that we could access numerically, the energetically less favourable configurations (*e.g.* wedge and triangular shaped configurations) continue to appear. It is possible that a much larger system size is required to verify our analytical prediction in this case.

NUMERICAL VERIFICATION OF MODE-COUPLING THEORY AND NON-LINEAR FLUCTUATING HYDRODYNAMICS FOR PROPAGATING MODES IN LH MODEL

6.1 INTRODUCTION

In this chapter, we study the disordered phase of the LH model (see Fig. 2.1). In characterising this phase, we are particularly interested in how the coupled time-evolution of particle density and landscape height gradient gives rise to different dynamical universality classes in the system, following the prescription of NLFH (see Sec. 1.2). However, unlike most NLFH studies so far, the exact steady state measure is not known for our system. In this phase, the coupling between the particles and the landscape is such that there is no long-ranged order in the particle or the landscape. However, there are still short-ranged correlations present in the system whose closed-form expressions are unknown. Therefore, in this case we are not able to write down exact expressions for the locally conserved currents in terms of the conserved densities which is required for carrying out the formalism of NLFH along with mode-coupling analysis (see Sec. 1.2). We rely on approximate expressions based on mean-field theory where we neglect all correlations in the system or a slightly improved approximation where we retain some nearest neighbor or next nearest neighbor correlations and ignore the rest. We develop a scheme for calculating currents based on such approximations and use those approximate expressions for current to carry out the analysis of NLFH and derive the conditions for observing different dynamical universality classes. Finally, we check our analytical predictions with numerical simulations. An important aspect that one has to keep in mind for this approach is presence of finite size effects. The scaling solution obtained from NLFH implicitly assumes the limit of large system size and large times. As we will show in the subsequent sections of this chapter, the numerical simulations involve measurement of space time correlations of the conserved modes and use the method of scaling collapse to verify the universality class. Clearly, finite size effects can play an important role here and may even mask the actual universality class which is expected to manifest itself in the scaling limit. In this work we perform a systematic analysis of the finite size effects and

explicitly demonstrate how it affects the conclusions. We also discuss how the criteria for observing different universality classes obtained from NLFH needs to be modified in view of finite size effects. The results discussed in this chapter are part of a manuscript under preparation [68].

6.2 SHORT-RANGED CORRELATIONS AND MEAN-FIELD CALCULATION IN THE DISORDERED PHASE

Fig. 2.1 shows the phase diagram for the LH model in the complete parameter range of b, b' that holds true for all values of ρ on an untilted surface ($m = 1/2$). Starting from the mean field expressions for the current, a linear stability analysis of the continuity equations for the two conserved fields predicts the $b' = -b$ line as the boundary between ordered and disordered phases for $m = 1/2$ [47]. In the disordered phase, neither the particles nor the landscape show any long ranged order and in this chapter, we focus on the disordered phase (dotted region in Fig. 2.1). Although in the disordered phase, the landscape and the particles do not have long ranged order, there are short ranged correlations present in the system. In Fig. 6.1 we show the nearest neighbor correlations between the particles and the tilts. Let η_i be the occupancy variable for H particle at site i , which takes the value 1 (or 0) if the site i is occupied by an H (L) particle. Similarly, let σ_i denote the tilt variable which is 1 (0) if the bond between sites i and $i + 1$ is upslope (downslope). We measure the four nearest neighbor correlations $\langle \eta_i \eta_{i+1} \rangle$ (Fig. 6.1, top left panel), $\langle \eta_i \sigma_i \rangle$ (Fig. 6.1, top right panel), $\langle \sigma_{i-1} \eta_i \rangle$ (Fig. 6.1, bottom left panel), and $\langle \sigma_i \sigma_{i+1} \rangle$ (Fig. 6.1, bottom right panel) in steady state for different values of b and b' within the disordered phase. From our dynamical rules in Eqs. 2.1 and 2.2 it follows that by interchanging between H and L and between b and b' , the model remains invariant. All correlations are therefore symmetric around the line $b = b'$ that bisects the disordered phase.

From Fig. 6.1, we observe that $\langle \eta_i \eta_{i+1} \rangle$ correlations are strongest. Therefore, any mean-field level approximation will be affected most by this nearest neighbor correlation among the H particles and we look for some parameter regime where this correlation is weak, in order for mean-field theory to work. All four correlations are also negligible near the bottom left corner of the phase diagram. The corner point $b = b' = -0.5$ has been studied earlier in [17] and it was shown that the system satisfies exact product measure in this case with pairwise balance [57]. In the vicinity of this point, all correlations are weak and mean-field theory is expected to work well in this neighborhood.

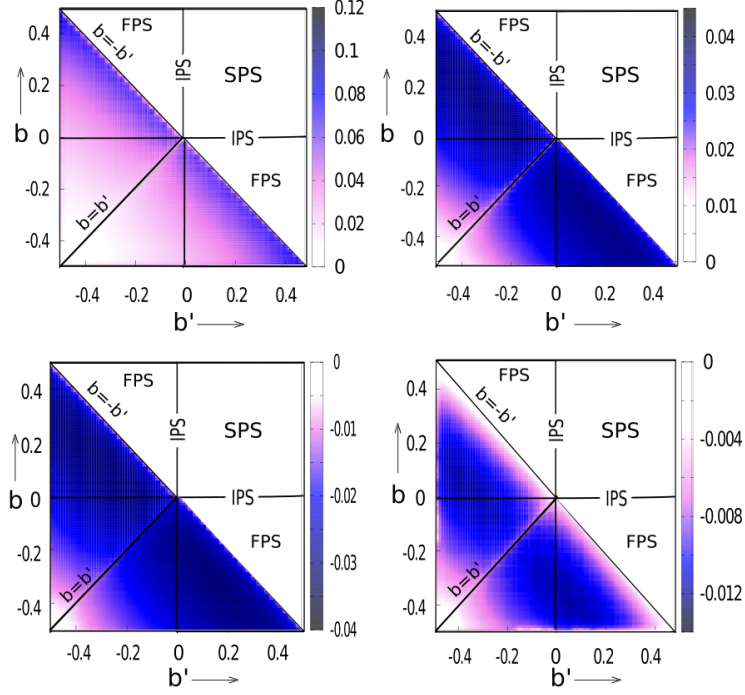


Figure 6.1: We plot nearest neighbor correlations in the disordered phase for $m = 1/2$. The top left panel shows the data for $\langle \eta_i \eta_{i+1} \rangle - \rho^2$, top right panel corresponds to $\langle \eta_i \sigma_i \rangle - \rho m$, bottom left panel $\langle \sigma_i \eta_{i+1} \rangle - \rho m$ and bottom right panel $\langle \sigma_i \sigma_{i+1} \rangle - m^2$. The plots are color-coded. Out of all these four correlations, particle-particle correlations are strongest while the surface bonds show weak anti-correlations. All four correlations vanish at $b = b' = -0.5$ point which satisfies product measure. Here, we have used $N = 2000$ and $\rho = 1/2$ and all data have been averaged over 10^5 histories.

Starting from the dynamical rules in Eqs. 2.1 and 2.2 one can write down the following formal expression for the average particle current J_ρ and tilt current J_m in the system,

$$\begin{aligned}
J_\rho &= (D + a)P(H \setminus L) + (D - a)P(H/L) \\
&\quad - (D + a)P(L/H) - (D - a)P(L \setminus H) \\
J_m &= (E + b)P(/H \setminus) + (E - b')P(/L \setminus) \\
&\quad - (E - b)P(\setminus H/) - (E + b')P(\setminus L/)
\end{aligned} \tag{6.1}$$

where, $P(H \setminus L)$ denotes the probability of a configuration that has an HL pair in two adjacent lattice sites connected by a downslope bond (\setminus). Similarly, $P(/H \setminus)$ denotes the probability to have an occupied local hill. All other terms in Eqs. 6.1 may be defined in the same manner. Within mean-field approximation, these joint probabilities can be factorized. For example, $P(H \setminus L)$ can be written as $\rho(1 - m)(1 - \rho)$, and $P(/H \setminus)$ becomes $m\rho(1 - m)$, and so on. Here, ρ denotes the density of H particles and m denotes the density of upslope bonds in the system. The average currents can thus be written as $J_\rho = 2a\rho(1 - \rho)(1 - 2m)$ and $J_m = m(1 - m)[2\rho(b + b') - 2b']$. Assumption of local equilibrium means when ρ and m

varies in space and time, local currents can still be obtained by substituting $\rho(x, t)$ and $m(x, t)$ in these expressions. We apply the formalism of NLFH illustrated in Sec. 1.2 starting with this expression for local currents and calculate the two mode-coupling matrices.

Our mean-field calculations correctly predict the $b = -b'$ line as the boundary between the ordered and disordered phase for $m = 1/2$ (Fig. 2.1) [48]. Using the above mean-field expressions for J_ρ and J_m , we can write down the Jacobian \mathbf{A} and its eigenvalues for $m = 1/2$ are $\lambda = \pm\sqrt{-2a\rho(1-\rho)(b+b')}$, which are real for $b < -b'$ and imaginary for $b > -b'$. Imaginary eigenvalues mean linear instability in $\rho(x, t)$ and $m(x, t)$ grows in time and takes the system to an ordered state with macroscopic inhomogeneity. On the other hand, real eigenvalues mean traveling wave solution holds, as discussed in Sec. 1.2. Thus $b = -b'$ line, marks the boundary between ordered and disordered phases. It is remarkable that mean-field theory makes this prediction so accurately because our plots in Fig. 6.1 show that in the vicinity of $b = -b'$ line correlations are particularly strong. We have checked that (data not shown here) for $m \neq 1/2$ the prediction does not work so well.

A somewhat improved approximation over mean-field theory might be retaining two-point or three-point correlations in the system and factorizing the rest. For example, $P(H\backslash L)$ can be written as $P(H\backslash)(1-\rho)$ and similarly, $P(/H\backslash) = P(H\backslash)m$, etc. Here, we have retained the correlations between a site and the next bond. These two-point correlations can be evaluated by writing down master equations for the probabilities $P(H/)$, $P(H\backslash)$, $P(L/)$ and $P(L\backslash)$ and (numerically) solving them in a self-consistent manner. An even better approximation can be obtained by retaining three point correlations like $P(H\backslash L)$ or $P(/H\backslash)$. These three point probabilities can again be evaluated by writing down the corresponding master equations and solving for steady state. However, our final conclusions are not so sensitive to whether we neglect all correlations in the system as in mean-field theory, or include two or three point correlations in our description. Using NLFH method (Sec. 1.2), when we calculate the mode-coupling matrices \mathbf{G}^1 and \mathbf{G}^2 , the condition of observing various universality classes depends on whether certain matrix elements are zero or non-zero. The actual value of these matrix elements may differ slightly depending on the approximations used, but that does not change the dynamical universality class. We carry out our analysis within that region of the disordered phase, where correlations are weak (see Fig. 6.1) and we find no significant difference based on our approximation scheme.

6.2.1 *Calculating currents from nearest neighbor approximations — master equation for two-point correlations*

Objects appearing in the expression for J_ρ are compound objects that can be formed out of a site-bond-site combination, while those for the bond current J_m comprise of three-point

objects formed in a bond-site-bond sequence. In this section, we will assume that mean field approximation works well beyond two-point functions, *i.e.*, we might express the probability of occurrence of the configurations like $P(H\backslash L), P(/H\backslash)$ as $P(H\backslash)(1 - \rho)$ and $P(H\backslash)m$ respectively, by retaining only the correlations between a site and the immediately next bond. From the colour plots presented in Fig. 6.1, this approximation can be expected to work well in the vicinities of the product measure point $b = b'$ where all the correlations are weak. With this convention, we write the following master equations for the probabilities for the four objects $P(H\backslash), P(L\backslash), P(H/), P(L/)$. The master equations for these probabilities consist of gain and loss terms that have 4-point probabilities like $P(H\backslash H/)$. Retaining only the correlations between a site and its right adjacent bond, this probability can be represented in the product form of two probabilities as, $P(H\backslash H/) = P(H\backslash)P(H/)$. The system of coupled non-linear differential equations so obtained can be solved numerically.

$$\begin{aligned}
\frac{dP(H/)}{dt} &= (E - b)P(H\backslash)P(H/) + (E + b')P(H\backslash)P(L/) \\
&\quad + (E + b)P(H\backslash)m + P(H\backslash)P(L/) + P(L/)\rho - (E + b)P(H/)P(H\backslash) \\
&\quad - (E - b')P(H/)P(L\backslash) - (E - b)P(H/)(1 - m) - P(L/)P(H/) \\
\frac{dP(H\backslash)}{dt} &= (E - b)P(H/)(1 - m) + (E + b)P(H/)P(H\backslash) \\
&\quad + (E - b')P(H/)P(L\backslash) + P(H\backslash)P(L\backslash) - (E + b)P(H\backslash)m \\
&\quad - (E - b)P(H\backslash)P(H/) - (E + b')P(H\backslash)P(L/) - P(L/)P(H\backslash) \\
&\quad - P(H\backslash)(1 - \rho) \\
\frac{dP(L/)}{dt} &= P(L/)P(H/) + (E - b')P(L\backslash)m + (E - b)P(L\backslash)P(H/) \\
&\quad + (E + b')P(L\backslash)P(L/) - P(L/)\rho - P(H\backslash)P(L/) - (E + b)P(L/)P(H\backslash) \\
&\quad - (E - b')P(L/)P(L\backslash) - (E + b')P(L/)(1 - m) \\
\frac{dP(L\backslash)}{dt} &= (E + b')P(L/)(1 - m) + (E + b)P(L/)P(H\backslash) \\
&\quad + (E - b')P(L/)P(L\backslash) + P(H\backslash)(1 - \rho) + P(L/)P(H\backslash) \\
&\quad - (E - b')P(L\backslash)m - (E - b)P(L\backslash)P(H/) - (E + b')P(L\backslash)P(L/) \\
&\quad - P(H\backslash)P(L\backslash)
\end{aligned} \tag{6.2}$$

Since the above set of equations are non-linear and have to be solved numerically, we do not have an closed-form expressions for the currents. For calculating the mode-coupling matrices for certain (ρ, m) sets one needs the knowledge of Jacobians and the Hessians consisting of respectively the first and second order derivatives of the currents with respect to the particle and tilt densities. Hence, it is required to have the current vs. density plots

around those ρ, m values with as small resolutions as possible. In parts of the disordered regime where all the nearest neighbor correlations are small in magnitude (lightly shaded regions in Fig. 6.1) and this formalism works well, we solve these equations for $0 \leq \rho, m \leq 1$ with spacing $\delta\rho, \delta m = 0.001$ and obtain J_ρ, J_m as a function of ρ, m . Later in this section, we compare the numerically measured values for the steady state currents and wave speeds with those obtained from solutions to the above equations for few values of b, b', ρ, m .

6.2.2 Calculating currents from next nearest-neighbour approximations — master equations for three-point correlations

We formulate master equations for all the possible 3-point quantities in the system, such as $P(H\backslash L), P(/H\backslash)$ etc. In order to solve the equations, we retain only the three point correlations and apply mean theory for the objects beyond. A set of 16 master equations is needed for describing the time evolution of all possible three-point objects in our model,

$$\begin{aligned}
P = \{ & P(H\backslash L), P(L\backslash H), P(H\backslash H), P(L\backslash L), P(H/L), P(L/H) \\
& P(H/H), P(L/L), P(/H\backslash), P(/L\backslash), P(\backslash H/), P(\backslash L/), \\
& P(/H/), P(/L/), P(\backslash H\backslash), P(\backslash L\backslash) \} \tag{6.3}
\end{aligned}$$

While decomposing higher-point objects such as $P(/H\backslash L/)$ that appear in the gain, loss terms in the master equations for the three-point quantities, we use the convention that retains the first three-point object and breaks up the rest using mean-field approximation. For example, using this convention, one has, $P(/H\backslash L/) = (1 - \rho)mP(/H\backslash)$. This yields a

linear set consisting of 16 master equations for the system which can be solved exactly. The set of master equations obtained using the above convention is given as follows:

$$\begin{aligned}
\frac{dP(H\backslash L)}{dt} &= (1 - \rho)(1 - m)P(H\backslash H) + (1 - \rho)(1 - m)P(H\backslash L) \\
&\quad + (E - b')(1 - m)P(L/H) + (E - b)(1 - \rho)P(\backslash H/) \\
&\quad - P(H\backslash L) - (1 - \rho)(1 - m)P(L/H) - \rho m P(H\backslash L) \\
&\quad - (E + b')mP(H\backslash L) - (E + b)(1 - \rho)P(/H\backslash)
\end{aligned} \tag{6.4}$$

$$\begin{aligned}
\frac{dP(L\backslash H)}{dt} &= P(L\backslash H) + \rho(1 - m)P(L/H) + \rho m P(L\backslash L) \\
&\quad + (E + b)(1 - m)P(L/H) + (E + b')\rho P(\backslash L/) \\
&\quad - (1 - \rho)(1 - m)P(L\backslash H) - \rho(1 - m)P(H\backslash L) \\
&\quad - (E - b)mP(L\backslash H) - (E - b')\rho P(/L\backslash)
\end{aligned} \tag{6.5}$$

$$\begin{aligned}
\frac{dP(H\backslash H)}{dt} &= \rho(1 - m)P(H\backslash L) + \rho m P(H\backslash L) + (E + b)(1 - m)P(H/H) \\
&\quad - (1 - \rho)(1 - m)P(H\backslash H) - \rho(1 - m)P(L/H) \\
&\quad + (E - b)mP(H\backslash H) - (E + b)\rho P(/H\backslash)
\end{aligned} \tag{6.6}$$

$$\begin{aligned}
\frac{dP(L\backslash L)}{dt} &= (1 - \rho)(1 - m)P(L/H) + (1 - \rho)(1 - m)P(L\backslash H) \\
&\quad + (E - b')(1 - m)P(L/L) + (E + b')(1 - \rho)P(\backslash L/) \\
&\quad - (1 - \rho)(1 - m)P(H\backslash L) - \rho m P(L\backslash L) - (E + b')mP(L\backslash L) \\
&\quad - (E - b')(1 - \rho)P(/L\backslash)
\end{aligned} \tag{6.7}$$

$$\begin{aligned}
\frac{dP(L/H)}{dt} &= \rho m P(L/L) + \rho m P(L/H) + (E - b) m P(L \setminus H) \\
&+ (E - b') \rho P(/L \setminus) - P(L/H) - \rho) m P(H \setminus L) \\
&- (1 - \rho)(1 - m) P(L/H) - (E + b') \rho P(\setminus L /) \\
&- (E + b)(1 - m) P(L/H)
\end{aligned} \tag{6.8}$$

$$\begin{aligned}
\frac{dP(H/L)}{dt} &= P(L/H) + (1 - \rho)(1 - m) P(H/H) + (1 - \rho) m P(H \setminus L) \\
&+ (E + b)(1 - \rho) P(/H \setminus) + (E + b') m P(H \setminus L) \\
&- (1 - \rho) m P(L/H) - \rho m P(H/L) - (E - b')(1 - m) P(H/L) \\
&- (E + b)(1 - \rho) P(\setminus H /)
\end{aligned} \tag{6.9}$$

$$\begin{aligned}
\frac{dP(H/H)}{dt} &= \rho m P(H/L) + \rho m P(H \setminus L) + (E - b) m P(H \setminus H) \\
&+ (E + b) \rho P(/H \setminus) - \rho m P(L/H) - (1 - \rho)(1 - m) P(H/H) \\
&- (E + b)(1 - m) P(H/H) - (E - b) \rho P(\setminus H /)
\end{aligned} \tag{6.10}$$

$$\begin{aligned}
\frac{dP(L/L)}{dt} &= (1 - \rho) m P(L/H) + (1 - \rho)(1 - m) P(L/H) \\
&+ (E - b')(1 - \rho) P(/L \setminus) + (E + b') m P(L \setminus L) - \rho m P(L/L) \\
&- (1 - \rho) m P(H \setminus L) - (E - b')(1 - m) P(L/L) \\
&- (E + b')(1 - \rho) P(\setminus L /)
\end{aligned} \tag{6.11}$$

$$\begin{aligned}
\frac{dP(/H\backslash)}{dt} &= (E - b)P(\backslash H/) + (E + b)\rho(1 - m)P(/H\backslash) \\
&+ (E + b)(1 - m)P(/H/) + (E - b')\rho(1 - m)P(/L\backslash) \\
&+ (E - b')(1 - \rho)(1 - m)P(/H/) - (E + b)P(/H\backslash) \\
&- (1 - \rho)P(/H\backslash) - (1 - m)P(L/H) - (E - b)\rho mP(/H\backslash) \\
&- (E - b)\rho(1 - m)P(\backslash H/) - (E + b')(1 - \rho)mP(/H\backslash) \\
&- (E + b'\rho(1 - m)P(\backslash L/)
\end{aligned} \tag{6.12}$$

$$\begin{aligned}
\frac{dP(\backslash H/)}{dt} &= mP(H\backslash L) + \rho P(\backslash L/) + (E + b)P(/H\backslash) \\
&+ (E - b)\rho mP(\backslash H\backslash) + (E + b')\rho mP(\backslash L/) \\
&- (E - b)P(\backslash H/) - (E + b)\rho(1 - m)P(\backslash H/) \\
&- (E + b)\rho(1 - m)P(\backslash H/) - (E + b)\rho mP(/H\backslash) \\
&- (E - b')(1 - \rho)(1 - m)P(\backslash H/) - (E - b')\rho mP(/L\backslash)
\end{aligned} \tag{6.13}$$

$$\begin{aligned}
\frac{dP(/L\backslash)}{dt} &= (1 - \rho)P(/H\backslash) + (1 - m)P(L/H) + (E + b')P(\backslash L/) \\
&+ (E - b')(1 - \rho)(1 - m)P(/L\backslash) + (E - b')(1 - \rho)(1 - m)P(/L/) \\
&+ (E + b)(1 - \rho)(1 - m)P(/H\backslash) + (E + b)\rho(1 - m)P(/L/) \\
&- (E + b')P(/L\backslash) - (E - b)\rho mP(/L\backslash) \\
&- (E - b)(1 - \rho)(1 - m)P(\backslash H/) - (E + b')(1 - \rho)mP(/L\backslash) \\
&- (E + b')(1 - \rho)(1 - m)P(\backslash L/)
\end{aligned} \tag{6.14}$$

$$\begin{aligned}
\frac{dP(\backslash L/)}{dt} &= (E - b')P(/L\backslash) + (E - b)\rho mP(L\backslash L) + (E - b)(1 - \rho)mP(\backslash H/) \\
&+ (E + b')(1 - \rho)mP(\backslash L\backslash) + (E + b')(1 - \rho)mP(\backslash L/) \\
&- (E + b')P(\backslash L/) - \rho P(\backslash L/) - mP(H\backslash L) \\
&- (E + b)\rho(1 - m)P(\backslash L/) - (E + b)(1 - \rho)mP(/H\backslash) \\
&- (E - b')(1 - \rho)(1 - m)P(\backslash L/) - (E - b')(1 - \rho)mP(/L\backslash)
\end{aligned} \tag{6.15}$$

$$\begin{aligned}
\frac{dP(/H/)}{dt} &= \rho P(/L/) + (E - b)\rho m P(/H\backslash) + (E + b')(1 - \rho)m P(/H\backslash) \\
&+ (E + b)\rho m P(/H\backslash) + (E - b')\rho m P(/L\backslash) - m P(L/H) \\
&- (E + b)\rho(1 - m)P(/H/) - (E - b')(1 - \rho)(1 - m)P(/H/) \\
&- (E - b)\rho m P(\backslash H/) - (E + b')\rho m P(\backslash L/)
\end{aligned} \tag{6.16}$$

$$\begin{aligned}
\frac{dP(/L/)}{dt} &= m P(L/H) + (E - b)\rho m P(/L\backslash) + (E + b')(1 - \rho)m P(/L\backslash) \\
&+ (E + b)(1 - \rho)m P(/H\backslash) + (E - b')(1 - \rho)m P(/L\backslash) - \rho P(/L/) \\
&- (E + b)\rho(1 - m)P(/L/) - (E - b')(1 - \rho)(1 - m)P(/L/) \\
&- (E - b)(1 - \rho)m P(\backslash H/) - (E + b')(1 - \rho)m P(\backslash L/)
\end{aligned} \tag{6.17}$$

$$\begin{aligned}
\frac{dP(\backslash H\backslash)}{dt} &= (1 - m)P(H\backslash L) + (E - b)\rho(1 - m)P(\backslash H/) \\
&+ (E + b')\rho(1 - m)P(\backslash L/) + (E + b)\rho(1 - m)P(\backslash H/) \\
&+ (E - b')(1 - \rho)(1 - m)P(\backslash H/) - (1 - \rho)P(\backslash H\backslash) \\
&- (E + b)\rho(1 - m)P(/H\backslash) - (E - b')\rho(1 - m)P(/L\backslash) \\
&- (E - b)\rho m P(\backslash H\backslash) - (E + b')(1 - \rho)m P(\backslash H\backslash)
\end{aligned} \tag{6.18}$$

$$\begin{aligned}
\frac{dP(\backslash L\backslash)}{dt} &= (1 - \rho)P(\backslash H\backslash) + (E + b)\rho(1 - m)P(\backslash L/) \\
&+ (E - b')(1 - \rho)(1 - m)P(\backslash L/) \\
&+ (E - b)(1 - \rho)(1 - m)P(\backslash H/) + (E + b')(1 - \rho)(1 - m)P(\backslash L/) \\
&- (1 - m)P(H\backslash L) - (E + b)(1 - \rho)(1 - m)P(/H\backslash) \\
&- (E - b')(1 - \rho)(1 - m)P(/L\backslash) - (E - b)\rho m P(\backslash L\backslash) \\
&- (E + b')(1 - \rho)m P(\backslash L\backslash)
\end{aligned} \tag{6.19}$$

The closed form expressions for the three point quantities thus obtained by solving the above equations are too long to be presented here. However, starting from the expressions for currents using these probabilities in Eq. 6.1, one may then calculate the wave speeds and obtain the mode-coupling matrices subsequently.

Below (see Table 6.1), we compare the numerical values of the currents and the wave speeds with those obtained by solving the two and three-point master equations at different parts of the phase diagram. Our comparisons show that the nearest neighbor and next nearest-neighbor approximations yield good match with the numerically obtained values in 3rd-quadrant since Fig. 6.1 shows that the correlations are weak on and around the $b = b'$

line. Although, when we calculate the speeds of the propagating modes using the first derivatives of these currents with respect to ρ, m , we do not find a quite good agreement with the numerically measured wave speeds (see Table 6.2).

b, b'	ρ, m	J_ρ				J_m			
		Simulations	2-pt.	3-pt.	MFT	Simulations	2-pt.	3-pt.	MFT
-0.3, -0.3	0.16, 0.203	0.073	0.0734	0.084	0.0798	0.0649	0.0626	0.0626	0.066
-0.4, -0.1	0.12, 0.26	0.0424	0.0421	0.056	0.0507	0.0117	0.0127	0.0167	0.0154
-0.1, -0.1	0.3, 0.3	0.0569	0.0684	0.089	0.084	0.0152	0.0137	0.0139	0.0168
-0.3, -0.3	0.89, 0.23	0.048	0.058	0.061	0.053	-0.0824	-0.085	-0.078	-0.083

Table 6.1: Comparison between particle and tilt currents measured in simulations and calculated from 2-point, 3-point master equations, and mean field theory. The error bar in the numerically measured currents are ± 0.00005 .

b, b'	ρ, m	λ_1			λ_2		
		Simulations	Master equation	MFT	Simulations	Master equations	MFT
-0.5, 0	0.36, 0.5	-0.323	-0.36 (3 point)	-0.339	0.323	0.305 (3 point)	0.339
-0.3, -0.5	0.56, 0.535	-0.421	-0.441(2 point)	-0.442	0.465	0.441 (2 point)	0.444
-0.3, -0.3	0.89, 0.23	-0.563	-0.545 (2 point)	-0.558	-0.139	-0.113(2 point)	-0.116
-0.3, -0.5	0.895, 0.2	-0.612	-0.608 (2 point)	-0.611	-0.136	-0.118 (2 point)	-0.122

Table 6.2: We present a few comparisons between the numerically measured speeds which we estimate from the moving peaks of the dynamical structure factors, speeds calculated using the currents obtained by solving the master equations, and the mean field values. The error bars in the numerically measured values of wave speeds are less than ± 0.001 .

6.3 SIMULATION RESULTS FOR DYNAMICAL STRUCTURE FUNCTION

To verify the predictions from NLFH we measure the dynamical structure function $C_{\alpha\alpha}(x, t) = \langle \phi_\alpha(0, 0) \phi_\alpha(x, t) \rangle$ with $\alpha = 1, 2$ in simulations and find out what value of the dynamical exponent z_α (see Eq. 1.2) gives the best scaling collapse. We compare this z_α with the one predicted by our NLFH calculations. We find finite size effects can significantly affect the value of z_α . We first demonstrate this for the point $b = b' = -0.5$, where product measure holds and exact expressions for J_ρ and J_m are available [54].

6.3.1 Significant finite size effects for $b = b' = -0.5$

Earlier studies for $b = b' = -0.5$ have shown that for different values of ρ and m the system can show KPZ and diffusive modes [54]. Let us consider the case for two KPZ modes, when G_{11}^1 and G_{22}^2 both are non-zero. In this case, a dynamical exponent $z_\alpha = 3/2$ is expected and $(x - \lambda_\alpha t)/t^{2/3}$, the scaling variable. In the top panel of Fig. 6.2 we present data for a particular set of values for ρ and m for which G_{11}^1 and G_{22}^2 are non-zero but their values are not so large, $G_{11}^1 = G_{22}^2 \simeq -0.6$. Plots 6.2(a), (b), and (c) show the scaling collapse for $C_{11}(x, t)$ for different system sizes. We find strong finite size effects in the scaling collapse and although for large systems $N = 16000$ the actual KPZ exponent is retrieved, there is significant deviation for small values of N . On the other hand, in Fig. 6.2(d), (e), and (f) we show the scaling collapse for $C_{11}(x, t)$ for another set of ρ, m values, for which $G_{11}^1 = -0.89$, $G_{22}^2 = -0.51$. The self-coupling term for the first mode is now larger than before and in this case we find much weaker finite size effect: for $N = 4000$ good agreement with KPZ exponent is obtained for the first mode. Our data in Fig. 6.2 also shows that for smaller N values, the shape of the master curve is not completely symmetric and the left tail is slightly longer than the right tail. However, as N becomes larger the symmetry is restored, as expected for a Prähofer-Spohn scaling function [46].

Let us analyse the reason behind strong finite size effects for smaller values of $G_{\alpha\alpha}^\alpha$. In Eq. 1.8 since $Q_{\alpha\alpha}$ is proportional to $(G_{\alpha\alpha}^\alpha)^2$, when the self-coupling co-efficient $G_{\alpha\alpha}^\alpha$ has small values, the third term on the right hand side of this equation also becomes small. In the limit $k \rightarrow 0$, this third term alone is expected to survive and the other terms should vanish. However, for finite system size N the smallest possible value of k is $2\pi/N$ and it is possible that if N is not so large, the diffusive and cross-coupling terms might become comparable to the self-coupling term and affect the value of z_α and the nature of the scaling function. In this case, one needs to consider very large N values when k is small enough and the effect of the diffusive and cross-coupling terms in Eq. 1.8 can be ignored. For larger value of $G_{\alpha\alpha}^\alpha$, the self-coupling term is already large, and the diffusive and cross-coupling terms can be ignored even when N is not so large.

Hence, although NLFH predicts a KPZ universality class for non-zero self-coupling, in order to numerically observe the same, it is not sufficient that $G_{\alpha\alpha}^\alpha$ is non-zero, it should also have a sufficiently large value. Otherwise, finite size effects can become overwhelmingly strong and the value of the dynamical exponent, as well as nature of the scaling function may be significantly affected. Our data in Fig. 6.2 are for the product measure point, where the exact expressions for currents are already available. However, this issue becomes even more crucial when currents are not exactly known and approximate expressions are used in NLFH analysis. In that case one must rely more heavily on numerics and it then becomes

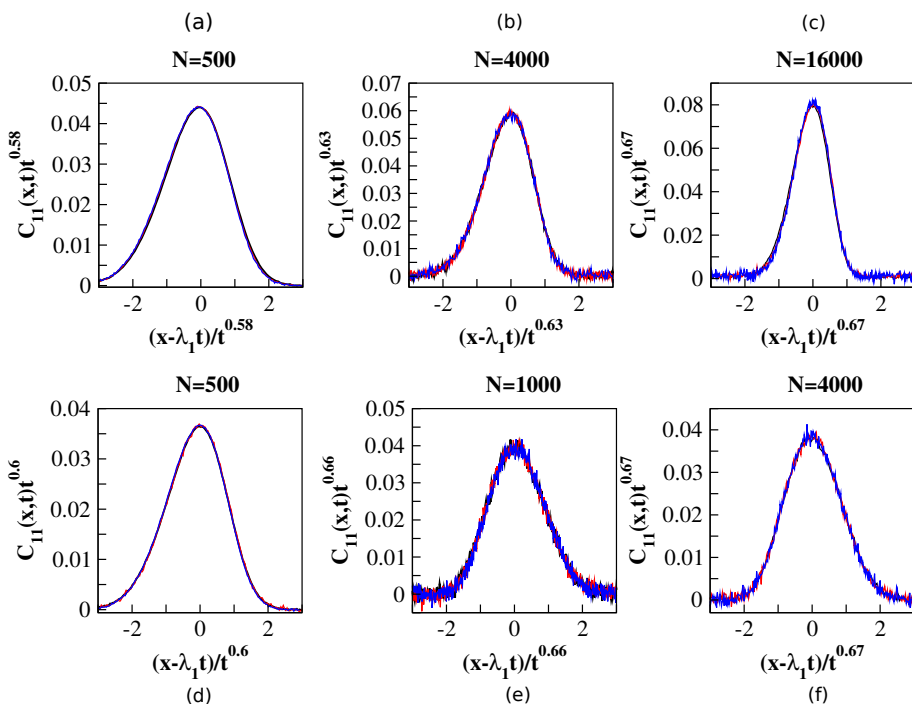


Figure 6.2: We show the collapse of dynamical structure functions $S(x,t)$ at 3 different times for system sizes $N=500$ (plot (a)), $N=4000$ (plot (b)), and $N=16000$ (plot (c)) corresponding to the parameter set $b = -0.5, b' = -0.5, \rho = 0.3, m = 0.5$ in the top panel. The G -matrix elements for these parameter values are: $G_{11}^1, G_{22}^2 = -0.6$. From the scaling collapse of the data at different times, we find the expected $1/z = 0.67 \pm 0.005$ for $N = 16000$. A systematic decrease in the exponent is observed with decreasing system sizes — $1/z = 0.63 \pm 0.01$ for $N = 4000$ and $1/z = 0.58 \pm 0.005$ as the system size is decreased to $N = 500$. The bottom panel corresponds to the parameter set $b = -0.5, b' = -0.5, \rho = 0.8, m = 0.6$. The G -matrix elements for these parameter values are: $G_{11}^1 \simeq -0.89, G_{22}^2 \simeq -0.51$. From the scaling collapse of the data at different times, we find an exponent $1/z = 0.67 \pm 0.005$ for $N = 4000$ (plot (f)), $1/z = 0.66 \pm 0.01$ for $N = 1000$ (plot (e)), whereas, the value of $1/z$ decreases to 0.6 ± 0.005 as the system size is decreased to $N = 500$ (plot (d)). The data shown in plots (a) and (d) have been averaged over 10^6 independent histories whereas those shown in the (b),(c),(e), and (f) have been averaged over at least 10^5 initial histories.

even more important that the numerical observation of the scaling collapse is not plagued by finite size effects. In the following subsections we show few such examples.

6.3.2 KPZ and 5/3 Lévy mode

As discussed in Sec. 1.2 (Chapter 1), the condition for having α -mode in KPZ universality class and mode β in 5/3 Lévy class is,

$$G_{\alpha\alpha}^\alpha, G_{\alpha\alpha}^\beta \neq 0, G_{\beta\beta}^\beta = 0 \quad (6.20)$$

and it follows from our discussions in the previous subsection that both $G_{\alpha\alpha}^\alpha$ and $G_{\alpha\alpha}^\beta$ should have large magnitude. We choose $b = b' = -0.3$, a point where spatial correlations are expected to be weak (see Fig. 6.1) and our approximate expressions for J_ρ and J_m agree reasonably well with currents measured in simulations (see Table 6.1). For this particular b, b' we plot the values of the diagonal elements of \mathbf{G}^1 and \mathbf{G}^2 in the ρ - m plane in Fig. 6.3.

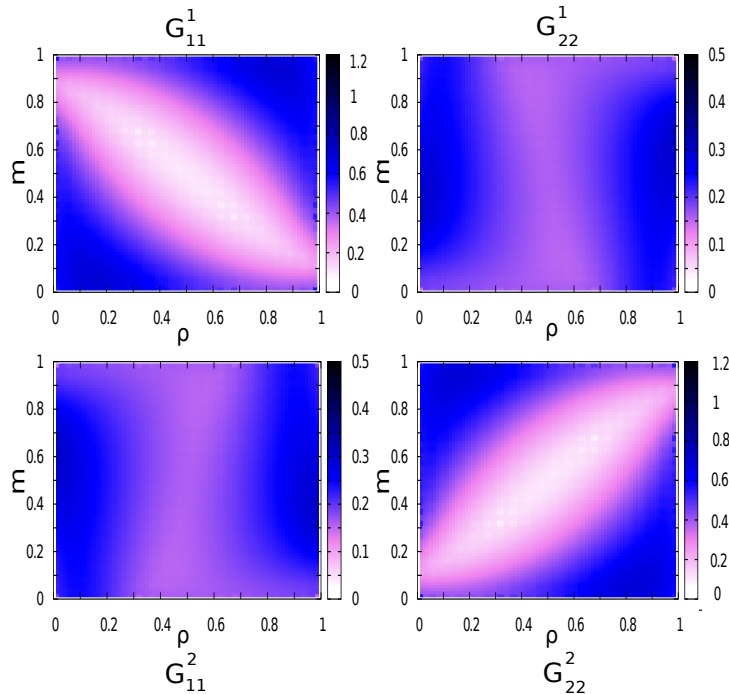


Figure 6.3: We show a contour map of all the four diagonal elements of the mode-coupling matrices in ρ, m plane for $b = -0.3, b' = -0.3$. The top left and right panels are plots corresponding to G_{11}^1, G_{22}^1 respectively, while the bottom panels correspond to G_{11}^2 (left) and G_{22}^2 (right). In our model it is possible to find several choices of ρ, m values for which Eq. 6.20 are satisfied such that both the non-zero elements are sufficiently large in order to be possible to verify a 5/3-Lévy mode numerically.

From this plot, we see that in the bottom-right region in the ρ - m plane, while G_{11}^1 is small in magnitude, G_{22}^2 is large, and G_{22}^1 is also moderately large which makes this region the best possible choice for observing 5/3-Lévy universality class for mode 1 and KPZ class for mode 2. We present our data in Fig. 6.4(a), (b) for $\rho = 0.89$ and $m = 0.23$. In plot 6.4(a),

we show our simulation data for $C_{11}(x, t)$ and find the best collapse is obtained when the shifted x -axis is rescaled with $t^{0.58}$, which is close to the value $3/5$ expected in this case. We also compare the master curve with α -Lévy stable distribution where $\alpha = 1/0.58 = 1.72$ and find reasonably good agreement. In Fig. 6.4(b) we show the scaling collapse for $C_{22}(x, t)$ and in this case we observe a dynamical exponent $z_2 = 3/2$ and our master curve also matches well with Prähofer-Spohn scaling function [46].

To demonstrate the finite size effect in this case, we now choose another point in the ρ - m plane, $\rho = 0.31$ and $m = 0.32$. From Fig. 6.3 we can see that at this point G_{11}^1 is large, G_{22}^2 is almost zero but G_{11}^2 is small. These values imply that while mode 1 is expected to show good agreement with KPZ universality class, the observation of $5/3$ -Lévy universality class for mode 2 may not be possible due to finite size effects. Indeed our data in Fig. 6.4(c),(d) show that the scaling collapse for $C_{11}(x, t)$ has been obtained for $1/z_1 \simeq 0.66$, which is close to KPZ exponent, but $C_{22}(x, t)$ shows a scaling collapse with $z_2 \simeq 2$ which corresponds to diffusive universality class, instead of $z_2 = 5/3$. Even the master curve in this case matches well with a Gaussian function which is the scaling function observed for a diffusive mode. Alternatively, the self-coupling term for mode 2 being close to zero in this case, in Eq. 1.8 only the diffusive term and the cross-coupling term are present and due to small magnitude of the cross-coupling term, the scaling behavior is dominated by the diffusive term. Our choice of $N = 16000$ is not large enough to remove this strong finite size effect and it is not numerically feasible to consider N much larger than this. We present a third scenario for KPZ, $5/3$ -Lévy combination, where we choose a point in the ρ - m plane which is close to one corner such that both ρ and m are high or low. We find in this case, although G_{11}^1 and G_{22}^2 are significantly large and G_{11}^2 is negligibly small, we do not find KPZ and $5/3$ -Lévy universality classes. In Fig. 6.4(e), (f) we show our data. We do not yet have any analytical arguments supporting this result.

6.3.3 Modified KPZ and diffusive mode

The condition for observing the α -mode in a modified KPZ class and β -mode in a diffusive class is

$$G_{\alpha\alpha}^\alpha, G_{\beta\beta}^\alpha \neq 0, G_{\beta\beta}^\beta = G_{\alpha\alpha}^\beta = 0 \quad (6.21)$$

This criterion can be satisfied for different set of b, b' values. First we present our data for $b = b' = -0.5$ where product measure holds and exact expression for currents are available [54]. In Fig. 6.5(a), (b) we present our simulation data for one particular choice of ρ and m and from the mode-coupling matrix elements given in the figure caption, it is clear that for the first mode we expect a modified KPZ behavior, while for the second mode we expect

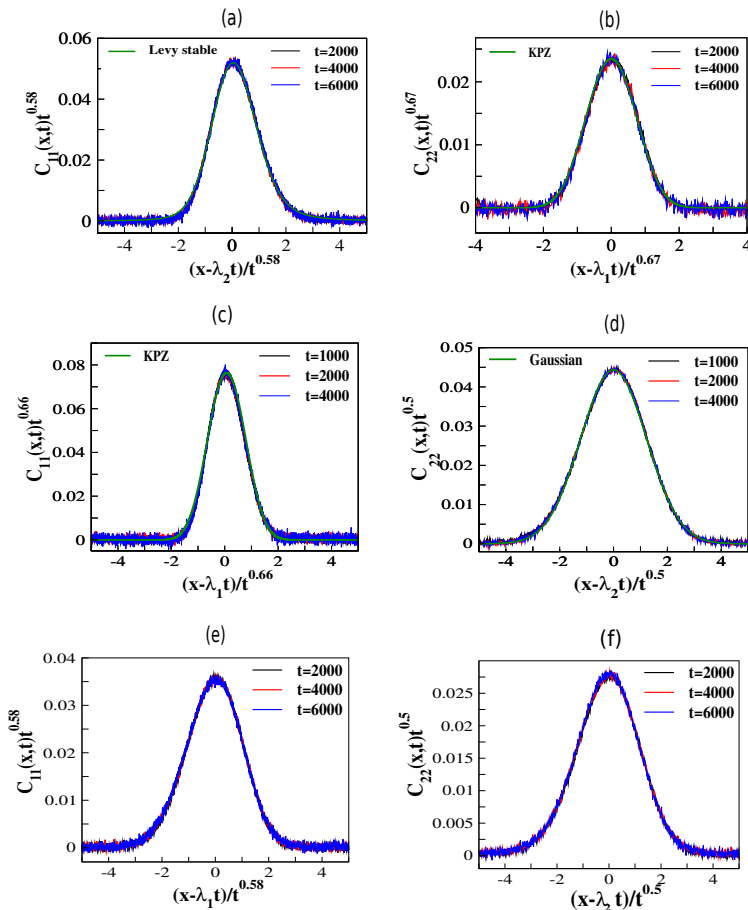


Figure 6.4: Dynamical structure factor $S(x, t)$ for both the modes corresponding to $b = -0.3, b' = -0.3, \rho = 0.89, m = 0.23$ at three different times for system size $N = 16000$ [(a) and (b)]. The G -matrices for these parameter values can be obtained by solving master equations for 2-point correlation functions: $G_{11}^1 = -0.06, G_{22}^1 = -0.39, G_{22}^2 = -1.01$. In this case, one expects $1/z = 0.6$ for the first mode and 0.67 for the second. Collapse of structure factors yield an exponent $1/z = 0.58 \pm 0.01$ for the first mode and $1/z = 0.67 \pm 0.01$ for the second. Structure functions have been compared with those of standard 0.58^{-1} -Lévy-stable distributions and KPZ distributions respectively. Plots (c) and (d) show the dynamical structure factor $S(x, t)$ corresponding to parameter values $b = b' = -0.3, \rho = 0.31, m = 0.32$ where a $5/3$ -rd Lévy would have been expected for the second mode [$G_{11}^1 = 0.512, G_{11}^2 = 0.126, G_{22}^2 = -0.003$]. From the collapse of $S(x, t)$, we find $1/z = 0.66 \pm 0.01$ for the 1st mode and $1/z = 0.5 \pm 0.01$ for the second. We compare our data with standard KPZ and Gaussian distribution functions. The data indeed shows that the second mode belongs to a diffusive universality class. Dynamical structure factor $S(x, t)$ corresponding to the parameter set $b = b' = -0.3, \rho = 0.915, m = 0.875$ have been shown in plots (e) and (f). Here, KPZ and $5/3$ -rd Lévy universality classes would have been expected for the first and second mode from the G -matrix elements respectively: $G_{11}^1 = -1.07, G_{11}^2 = -0.431, G_{22}^2 = -0.002$. From the collapse of $S(x, t)$, we find $z = 0.58 \pm 0.01$ for the 1st mode and $1/z = 0.5 \pm 0.01$ for the second. These data have been averaged over at least 10^5 independent histories.

diffusive scaling. Fig. 6.5(a) shows the structure function for mode 1 which shows a good scaling collapse for $1/z_1 = 0.66$, which is close to the expected value $2/3$. However, our mas-

ter curve fits rather well with usual Prähofe-Spohn scaling function, which is unexpected for a modified KPZ universality class, where a different scaling function is expected. Fig. 6.5(b) shows structure function of the second mode and as expected, it belongs to the diffusive universality class.

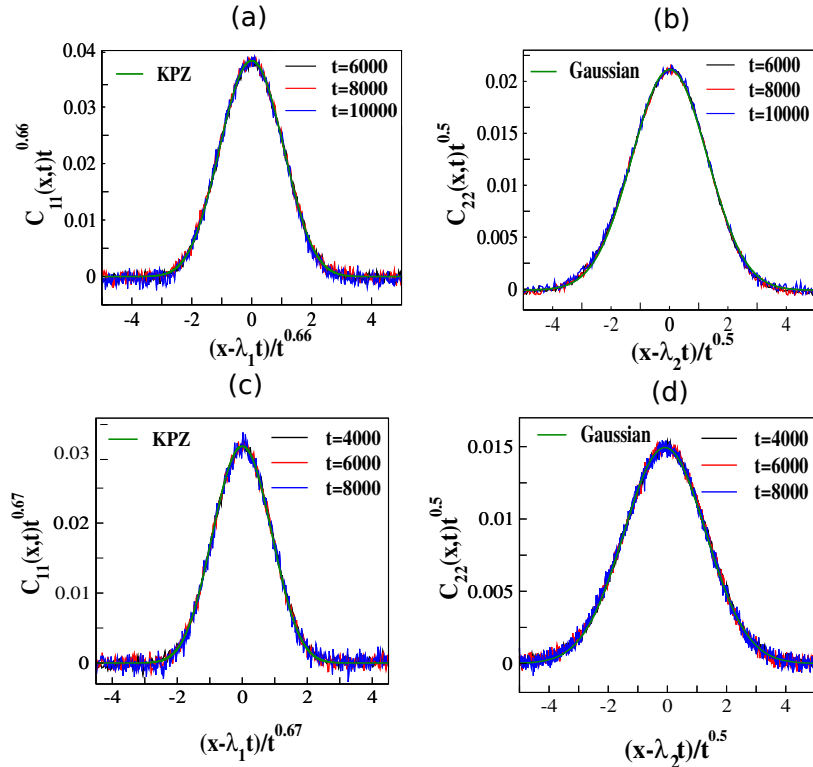


Figure 6.5: We show the dynamical structure factor $S(x, t)$ corresponding to parameter values $b = -0.5, b' = -0.5, \rho = 0.92, m = 0.93$ for $N = 16000$ in the top panel. For this case, the matrix elements are: $G_{11}^1 = 1.8, G_{22}^1 = 0.6, G_{11}^2 = 0.025, G_{22}^2 = -0.076$. From the collapse of structure factors measured at different times, we find an exponent $1/z_1 = 0.66 \pm 0.01$ (plot (a)) for the first mode, whereas the second mode is diffusive, with $1/z_2 = 0.5 \pm 0.005$ (plot (b)). Dynamical structure factor $S(x, t)$ corresponding to another set of parameter values $b = -0.3, b' = -0.5, \rho = 0.12, m = 0.105$ for $N = 16000$ is shown in the bottom panel. For this case, the matrix elements are: $G_{11}^1 = 1.52, G_{22}^1 = -0.5, G_{11}^2 = 0.023, G_{22}^2 = 0.004$. From the collapse of structure factors measured at different times, we find an exponent $1/z = 0.67 \pm 0.01$ for the first mode (plot (c)), whereas the second mode is diffusive, with $1/z = 0.5 \pm 0.01$ (plot (d)). The collapsed master curves in plots (a) and (c) match with that of an usual Prähofe-Spohn scaling function. These data have been averaged over at least 10^5 independent histories.

It is not clear why we fail to observe modified KPZ scaling in this case. From the values of the mode-coupling matrix elements given in the caption of Fig. 6.5 we notice that the self-coupling term G_{11}^1 is almost thrice in magnitude than the cross-coupling term G_{22}^1 . So it is possible that the cross-coupling is not felt so strongly and the mode shows usual KPZ scaling. Since the exact form of the modified KPZ scaling function is not known, it might also be possible that the functional form is not too different from the usual Prähofe-Spohn

scaling function to be numerically able to distinguish between the two. We have extensively searched in our parameter space but could not find any (b, b', ρ, m) set for which Eq. 6.21 is satisfied, and $G_{\alpha\alpha}^\alpha$ is smaller than $G_{\beta\beta}^\alpha$. We show one example in Fig. 6.6, where we plot the mode-coupling matrix elements in the ρ - m plane for one specific (b, b') set. Although Eq. 6.21 is satisfied for many (ρ, m) values, for each of them we find the self-coupling term is significantly larger than the cross-coupling term. Our simulation data shows usual KPZ scaling in this case also (see Fig. 6.5c).

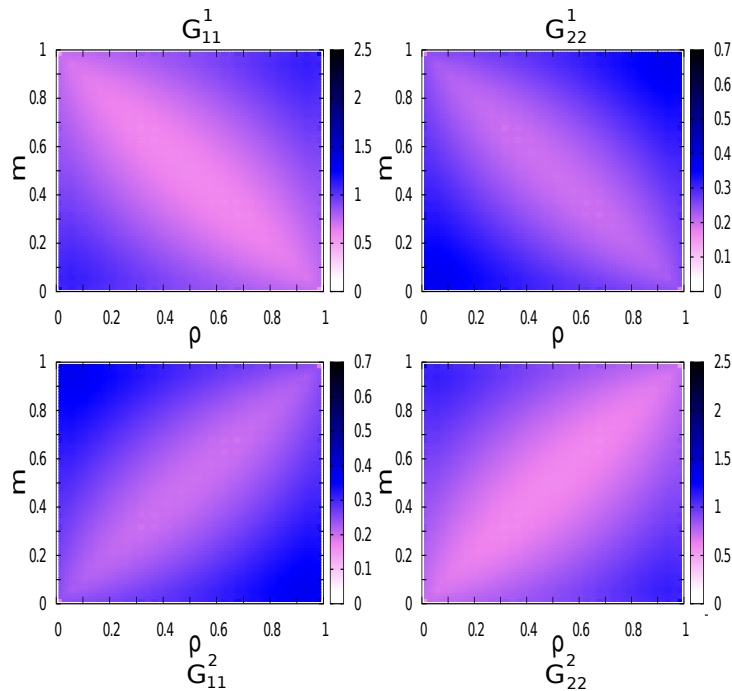


Figure 6.6: We show a contour map of all the four diagonal elements of the mode-coupling matrices in ρ, m plane for $b = -0.3, b' = -0.5$. The top left and right panels are plots corresponding to G_{11}^1, G_{22}^1 respectively, while the bottom panels correspond to G_{11}^2 (left) and G_{22}^2 (right). In our model it is possible to find several choices of ρ, m values for which Eq. 6.21 are satisfied such that both the non-zero elements are sufficiently large in order to be possible to verify a modified KPZ mode numerically.

6.3.4 Golden mean modes

Golden mean modes always occur in pairs, since the dynamical exponents z_α and z_β satisfy the conditions $z_\alpha = 1 + 1/z_\beta$ and $z_\beta = 1 + 1/z_\alpha$, whose recursive solution yields $z_\alpha = z_\beta = (\sqrt{5} + 1)/2$. In our system there are only two modes and hence both $C_{11}(x, t)$ and $C_{22}(x, t)$ should show scaling as per the golden mean universality class. This happens when the self-coupling term vanishes and the cross-coupling term survives for each mode:

$$G_{22}^1, G_{11}^2 \neq 0; G_{11}^1 = G_{22}^2 = 0 \quad (6.22)$$

However, we find that in our system these criteria are not simultaneously satisfied. We cannot find any point in our parameter space where both cross-coupling terms are sufficiently large (to avoid finite size effects) and self-coupling terms are negligibly small. We illustrate this in Fig. 6.7 where we have shown the variation of these matrix elements in the ρ - m plane for a fixed b, b' . The top right and bottom left panels show the variation of the cross-coupling co-efficients and it is clear from the color shades in these two panels that whenever one cross-coupling term gets large, the other one becomes small. Therefore, the condition in Eq. 6.22 is not satisfied. Our simulation results for the structure functions confirm this reasoning. We have determined the dynamical exponents in this case by measuring the variance of the structure functions as a function of time (data not shown) and found that for both modes, the variance scales as $t^{0.57}$, whereas for golden mean an exponent $\simeq 0.62$ should be obtained. In Fig. 6.8(a),(b) we show the scaling collapse of $C_{11}(x, t)$ and $C_{22}(x, t)$ and both modes show good collapse with $\sim t^{0.57}$ scaling.

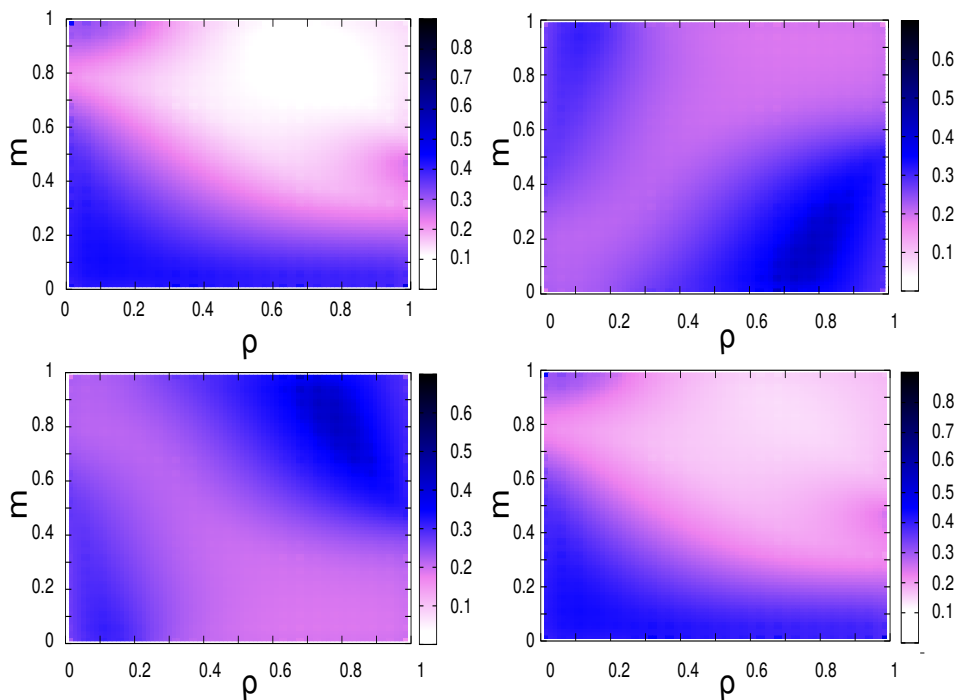


Figure 6.7: We show a contour map of all the four diagonal elements of the mode-coupling matrices in ρ, m plane for $b = 0.1, b' = -0.3$. The top left and right panels are plots corresponding to G_{11}^1, G_{22}^1 respectively, while the bottom panels correspond to G_{11}^2 (left) and G_{22}^2 (right). All the four elements simultaneously assume very small magnitudes at the central light colour zone and hence, it never so happens that $G_{11}^1, G_{22}^2 \simeq 0$ simultaneously with sufficiently large non-zero values of G_{22}^1, G_{11}^2 to override the finite size effects severely affecting the numerical observations for the dynamical exponent.

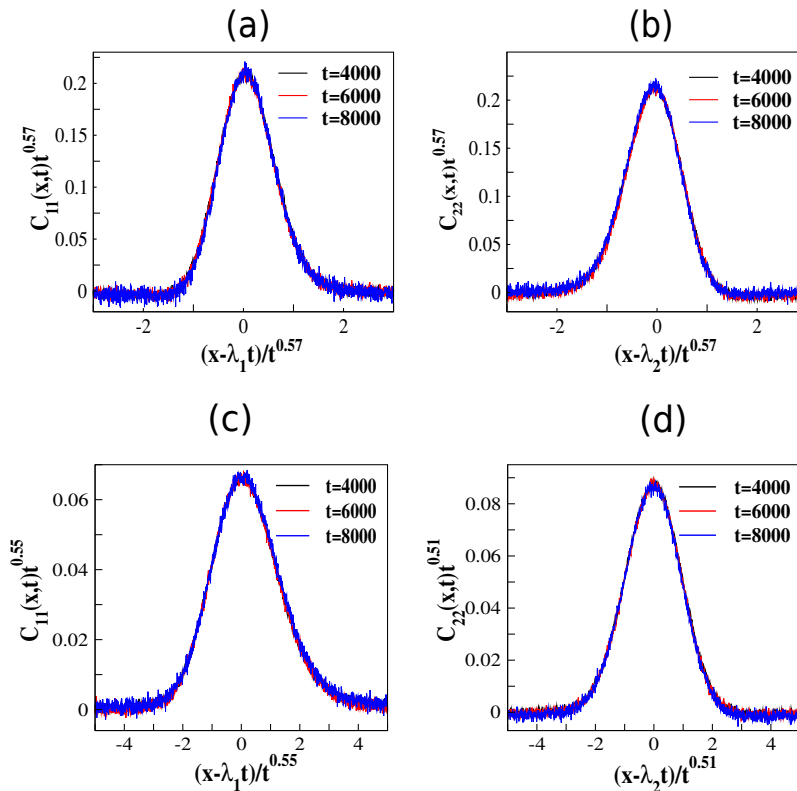


Figure 6.8: We measure the dynamical structure factor $S(x, t)$ at 3 different times for both the modes corresponding to parameter values $b = 0.1, b' = -0.3, \rho = 0.67, m = 0.49$ for $N = 16000$ in the top panel. For this case, the matrix elements are: $G_{11}^1 = -0.067, G_{22}^1 = -0.233, G_{11}^2 = -0.20, G_{22}^2 = 0.082$ and one expects the golden mean universality class ($1/z = 0.618$) for both the modes. The estimate of G -matrices for these parameter values can be obtained from mean field expressions for currents. From the scaling collapse of the data at different times, we find an exponent $1/z = 0.57 \pm 0.02$ for both the modes. The bottom panel shows dynamical structure factor $S(x, t)$ for both the modes corresponding to parameter values $b = 0.1, b' = -0.3, \rho = 0.85, m = 0.34$ for $N = 16000$. For this case, one expects a 3/2-Lévy scaling for the first mode and diffusive scaling for the second. The matrix elements are: $G_{11}^1 = 0.0098, G_{22}^1 = 0.739, G_{11}^2 = -0.05, G_{22}^2 = -0.07$. From the collapse of structure factors measured at different times, we find an exponent $1/z = 0.55 \pm 0.01$ for the first mode, whereas the second mode is diffusive, with $1/z = 0.51 \pm 0.01$. These data have been averaged over at least 10^5 independent histories.

6.3.5 3/2-Lévy and diffusive mode

The criteria for observing a 3/2-Lévy universality class for the mode α and diffusive class for mode β is

$$G_{\alpha\alpha}^\alpha = G_{\alpha\alpha}^\beta = G_{\beta\beta}^\beta = 0, G_{\beta\beta}^\alpha \neq 0. \quad (6.23)$$

We find that in our system this criterion is not satisfied for any parameter regime. Although it is possible to find self-coupling term for both modes and cross-coupling term for

the mode β simultaneously small, the cross-coupling term for mode α also tends to be small in this case (see Fig. 6.7). As a result, we are not able to observe 3/2-Lévy mode in our system. We show one example in Fig. 6.8(c), (d).

6.4 CONCLUSION

We have studied disordered state dynamics of a coupled system of sliding particles on a fluctuating landscape using the recently developed formalism of NLFH. In a large part of our parameter space, product measure is not satisfied and exact current-density relationship is not known. We restrict our study to those regions of the parameter space where spatial correlations are weak and mean-field approximation can be used. We have also used an improved approximation where short ranged correlations are self-consistently calculated and other correlations are factorized. Using our approximate expression for currents we perform NLFH calculation which predicts the existence of 5/3-Lévy, 3/2-Lévy, golden mean, modified KPZ universality classes, apart from usual KPZ and diffusive classes. However, when we attempt to verify these predictions from our numerical simulations, we encounter strong finite size effects. We demonstrate that it is not enough to have a certain mode-coupling coefficient non-zero, its magnitude needs to be significantly large in order for that term to dominate in the scaling limit. This makes it difficult for us to observe golden mean or 3/2-Lévy universality classes in our system, but we have been able to verify the existence of 5/3-Lévy universality class. The case of modified KPZ universality class yields some interesting outcome which we have not been able to explain. Instead of finding a scaling function different from Prähofer-Spohn scaling function, we find that our data match well with Prähofer-Spohn function. Thus our observation of modified KPZ cannot be distinguished from an usual KPZ universality class. Note that in an earlier study [54] it was reported that for $b = b' = -0.5$, where product measure holds, one can observe only usual KPZ or diffusive universality class. Using formalism of NLFH we find that even in this product measure point, one can have some ρ , m values where one mode follows modified KPZ class and the other mode is diffusive. But our numerical simulations show usual KPZ class, in agreement with [54]. To the best of our knowledge, our study is the first step towards the extension of the formalism of NLFH for systems where exact steady state measure is not known. It is of importance to have a general understanding of the significant finite size effects for various different unconventional universality classes. It would be intriguing to quantify how the finite size effects manifest themselves for various non-product-measure systems that obey different dynamical rules.

BIBLIOGRAPHY

- ¹J. J. Tyson and B. Novak, *Interface Focus* **4**, 20130070 (2014) (cit. on p. 1).
- ²R. Lipowsky, S. Klumpp, and T. M. Nieuwenhuizen, *Phys. Rev. Lett.* **87**, 108101 (2001) (cit. on p. 1).
- ³R. J. Allen and B. Waclaw, *Rep. Prog. Phys.* **82**, 016601 (2019) (cit. on p. 1).
- ⁴D. Chowdhury, L. Santen, and A. Schadschneider, *Physics Reports* **329**, 199 (2000) (cit. on p. 1).
- ⁵*Turbulence and stochastic processes*, Vol. 434 (Edited by J. C. R. Hunt, O. M. Philips, and D. Williams, Proc. R. Soc. London A, 1991), pp. 1–240 (cit. on p. 1).
- ⁶B. Schmittmann and R. K. P. Zia, *Phase transitions and critical phenomena*, vol. 17 (Academic Press, London, 1995) (cit. on p. 1).
- ⁷R. H. Kraichnan, *Phys. Rev. Lett.* **72**, 7 (1994) (cit. on p. 2).
- ⁸B. Derrida, *Phys. Scr.* **T38**, 6 (1991) (cit. on p. 2).
- ⁹B. I. Shraiman and E. D. Siggia, *Nature* **405**, 639 (2000) (cit. on p. 2).
- ¹⁰D. Goswami, K. Gowrishankar, S. Bilgrami, S. Ghosh, R. Raghupathy, R. Chadda, R. Vishwakarma, M. Rao, and S. Mayor, *Cell* **135**, 1085 (2008) (cit. on pp. 2, 5).
- ¹¹T. S. Van Zanten, A. Cambi, M. Koopman, B. Joosten, C. G. Figdor, and M. F. Garcia-Parajo, *Proc. Natl. Acad. Sci.* **106**, 18557 (2009) (cit. on pp. 2, 5).
- ¹²K. Gowrishankar, S. Ghosh, S. Saha, C. Rumamol, S. Mayor, and M. Rao, *Cell* **149**, 1353 (2012) (cit. on pp. 2, 5).
- ¹³A. Das, A. Polley, and M. Rao, *Phys. Rev. Lett.* **116**, 068306 (2016) (cit. on pp. 2, 4, 5).
- ¹⁴R. Varma, G. Campi, T. Yokosuka, T. Saito, and M. L. Dustin, *Immunity*, 117–27 (2006) (cit. on p. 2).
- ¹⁵C. Yu, J. B. K. Law, M. Suryana, H. Y. Low, and M. P. Sheetz, *Proc. Natl. Acad. Sci.* **108**, 51 (2011) (cit. on p. 2).
- ¹⁶D. Ertas and M. Kardar, *Phys. Rev. E* **8**, 2 (1993) (cit. on p. 2).
- ¹⁷D. Das, A. Basu, M. Barma, and S. Ramaswamy, *Phys. Rev. E* **64**, 021402 (2001) (cit. on pp. 2, 68).
- ¹⁸P. Ferrari, S. Sasamoto, and H. Spohn, *J. Stat. Phys.* **153**, 317 (2013) (cit. on p. 2).

- ¹⁹H. Spohn, *J. Stat. Phys.* **154**, 1191 (2014) (cit. on pp. 2, 6).
- ²⁰B. Derrida, E. Domany, and D. Mukamel, *J. Stat. Phys.* **69** (1992) (cit. on pp. 3, 13, 21, 37, 56, 57).
- ²¹S. A. Janowsky and J. L. Lebowitz, *Phys. Rev. A* **45**, 2 (1992) (cit. on p. 3).
- ²²J. M. Crowley, *J. Fluid Mech.* **45**, 151 (1971) (cit. on p. 3).
- ²³J. M. Crowley, *Phys. Fluids* **19**, 1296 (1976) (cit. on p. 3).
- ²⁴R. Lahiri and S. Ramaswamy, *Phys. Rev. Lett.* **79**, 1150 (1997) (cit. on pp. 3, 10–12, 15, 19, 25–27, 43, 58).
- ²⁵R. Lahiri, M. Barma, and S. Ramaswamy, *Phys. Rev. E* **61**, 1648 (2000) (cit. on pp. 3, 10, 11, 15, 19, 25–27, 43, 58).
- ²⁶M. R. Evans, Y. Kafri, H. M. Koduvely, and D. Mukamel, *Phys. Rev. Lett.* **80**, 425–429 (1998) (cit. on pp. 4, 11, 12, 26, 27).
- ²⁷D. Das and M. Barma, *Phys. Rev. Lett.* **85**, 1602 (2000) (cit. on pp. 4, 5, 11, 19, 42).
- ²⁸S. Chatterjee and M. Barma, *Phys. Rev. E* **73**, 011107 (2006) (cit. on pp. 4, 42).
- ²⁹A. J. Bray, *Adv. Phys.* **43**, 357 (1994) (cit. on p. 4).
- ³⁰B. Drossel and M. Kardar, *Phys. Rev. B* **66**, 195414 (2002) (cit. on p. 5).
- ³¹A. Nagar, M. Barma, and S. N. Majumdar, *Phys. Rev. Lett.* **94**, 240601 (2005) (cit. on p. 5).
- ³²B. Veksler and N. Gov, *Biophys. J.* **93**, 3798 (2007) (cit. on p. 5).
- ³³B. Peleg, A. Disanza, G. Scita, and N. Gov, *PLoS One* **6**, e18635 (2011) (cit. on p. 5).
- ³⁴F. Cagnetta, M. R. Evans, and D. Marenduzzo, *Phys. Rev. Lett.* **120**, 258001 (2018) (cit. on p. 5).
- ³⁵F. Cagnetta, M. R. Evans, and D. Marenduzzo, *Phys. Rev. E* **99**, 042124 (2019) (cit. on p. 5).
- ³⁶M. Kardar, G. Parisi, and Y.-C. Zhang, *Phys. Rev. Lett.* **56**, 889 (1986) (cit. on pp. 5, 32).
- ³⁷S. F. Edwards and D. R. Wilkinson, *Proc. R. Soc. London, Ser. A* **381**, 17 (1982) (cit. on pp. 5, 20, 31, 32).
- ³⁸H. van Beijeren, *Phys. Rev. Lett.* **108**, 180601 (2012) (cit. on p. 6).
- ³⁹A. Roy, A. Dhar, O. Narayan, and S. Sabhapandit, *J. Stat. Phys.* **160**, 73 (2015) (cit. on p. 6).
- ⁴⁰H. Spohn and G. Stoltz, *J. Stat. Phys.* **160**, 861 (2015) (cit. on pp. 6, 10).
- ⁴¹S. G. Das, A. Dhar, K. Saito, C. B. Mendl, and H. Spohn, *Phys. Rev. E* **90**, 012124 (2014) (cit. on p. 6).
- ⁴²V. Popkov, J. Schmidt, and G. M. Schütz, *Phys. Rev. Lett.* **112**, 200602 (2014) (cit. on p. 6).
- ⁴³V. Popkov, J. Schmidt, and G. M. Schütz, *J. Stat. Phys.* **160**, 835 (2015) (cit. on p. 6).

- ⁴⁴A. Miron, J. Cividini, A. Kundu, and D. Mukamel, Phys. Rev. E **99**, 012124 (2019) (cit. on p. 7).
- ⁴⁵V. Popkov, A. Schadschneider, J. Schmidt, and G. M. Schütz, J. Stat. Mech., 093211 (2016) (cit. on p. 8).
- ⁴⁶M. Prahöfer and H. Spohn, J. Stat. Phys. **115**, 255 (2004) (cit. on pp. 9, 78, 81).
- ⁴⁷S. Chakraborty, S. Pal, S. Chatterjee, and M. Barma, Phys. Rev. E **93**, 050102(R) (2016) (cit. on pp. 10, 12, 15, 20, 40, 46, 59, 68).
- ⁴⁸S. Chakraborty, S. Chatterjee, and M. Barma, Phys. Rev. E **96**, 022127 (2017) (cit. on pp. 10, 13, 15, 23, 59, 70).
- ⁴⁹S. Chakraborty, S. Chatterjee, and M. Barma, Phys. Rev. E **96**, 022128 (2017) (cit. on pp. 10, 15, 40, 43, 59).
- ⁵⁰B. Derrida, J. L. Lebowitz, and E. R. Speer, J. Stat. Phys. **107**, 599 (2002) (cit. on pp. 12, 21, 34, 41, 51).
- ⁵¹S. Chatterjee and M. Barma, J. Stat. Mech.: Theo. Exp. **2007**, L01004 (2007) (cit. on pp. 12, 21, 58).
- ⁵²A. N. Kolmogorov, Math. Ann. **112**, 155 (1936) (cit. on pp. 12, 31).
- ⁵³M. Barma and S. Ramaswamy, Turk. J. Phys. **24**, 235 (2000) (cit. on p. 18).
- ⁵⁴D. Das, M. Barma, and S. N. Majumdar, Phys. Rev. E **64**, 046126 (2001) (cit. on pp. 21, 77, 78, 81, 87).
- ⁵⁵M. Clincy, B. Derrida, and M. R. Evans, Phys. Rev. E **67**, 06115 (2003) (cit. on p. 27).
- ⁵⁶E. N. Economou, *Green's functions in quantum physics* (Springer-Verlag Berlin Heidelberg, 2006) (cit. on p. 33).
- ⁵⁷G. M. Schütz, R. Ramaswamy, and M Barma, J. Phys. A: Math. Gen. **29**, 837 (1996) (cit. on pp. 41, 68).
- ⁵⁸G. E. Uhlenbeck and L. S. Ornstein, Phys. Rev. **36**, 823 (1930) (cit. on pp. 45, 49).
- ⁵⁹P. A. Ferrari, E. Presutti, E. Scaciatelli, and M. E. Vares, Stoch. Proc. Appl. **39**, 89 (1991) (cit. on p. 52).
- ⁶⁰T. M. Liggett, *Interacting particle systems* (Springer-Verlag, New York, 1985) (cit. on p. 52).
- ⁶¹M. J. Lighthill and G. B. Whitham, Proc. R. Soc. Lond Ser A **229**, 281 (1955) (cit. on p. 56).
- ⁶²S. N. Majumdar and M. Barma, Phys. Rev. B **44**, 5306 (1991) (cit. on p. 56).
- ⁶³S. Gupta, S. N. Majumdar, C. Godreche, and M. Barma, Phys. Rev. E **76**, 021112 (2007) (cit. on p. 56).
- ⁶⁴M. J. Lighthill and G. B. Whitham, Proc. R. Soc. Lond Ser A **229**, 317 (1955) (cit. on p. 56).

- ⁶⁵G. Manoj and M. Barma, *J. Stat. Phys.* **110**, 1305–1316 (2013) (cit. on p. 59).
- ⁶⁶A. L. Barabasi and H. E. Stanley, *Fractal concepts in surface growth* (Cambridge University Press, 1995) (cit. on p. 63).
- ⁶⁷F. D. A. Aarao Reis, *Phys. Rev. E* **69**, 021610 (2004) (cit. on p. 63).
- ⁶⁸S. Chakraborty, S. Chatterjee, and M. Barma, Manuscript in preparation (2019) (cit. on p. 68).
- ⁶⁹R. Kapri, M. Bandopadhyay, and M. Barma, *Phys. Rev. E* **93**, 012117 (2016).